

Development of a Flexible Actuator and Motion Planning for Endoscopic Robots

A Thesis

Submitted for the Degree of

Doctor of Philosophy

in the **Faculty of Engineering**

by

Ashwin K P



Mechanical Engineering
Indian Institute of Science
Bangalore – 560 012 (INDIA)

July 2018

© Ashwin K P
July 2018
All rights reserved

Dedicated to the benevolent Gods
—the creators, providers and saviors—
Mother and Father

CERTIFICATE

I hereby certify that the content embodied in this thesis titled **Development of a flexible actuator and motion planning for endoscopic robots** has been carried out by Mr. Ashwin K P at the Indian Institute of Science, Bangalore under my supervision and that it has not been submitted elsewhere for the award of any degree or diploma.

Signature of the Thesis Supervisor:

.....

Professor Ashitava Ghosal

Dept. of Mechanical Engineering

Indian Institute of Science, Bangalore

DECLARATION

I hereby declare that the content embodied in this thesis titled **Development of a flexible actuator and motion planning for endoscopic robots** is the research carried out by me at the Department of Mechanical Engineering, Indian Institute of Science, Bangalore under the supervision Prof. Ashitava Ghosal, Department of Mechanical Engineering, IISc. In keeping with the general practice in reporting scientific observations, due acknowledgment has been made wherever the work described is based on the findings of other investigations.

Signature of the Author:

.....

Ashwin K P

Dept. of Mechanical Engineering

Indian Institute of Science, Bangalore

Acknowledgements

While the successful completion of this work is attributed to academic and personal influence of many, I take this opportunity to thank a few people without whom it would have been almost impossible.

First and foremost, I express my whole-hearted thanks to Prof. Ashitava Ghosal for his guidance and support throughout. He granted me a lot of freedom to think and work on topics of my interest, at my convenient pace, and always encouraged and helped me at critical junctures in my research. Apart from robotics, I have learned from him many qualities which I believe, have improved my professional as well as personal character. His traits as a mentor is something I will try to imitate, should I pursue a career in teaching!

I thank IISc and the Department of Mechanical Engineering, for providing me the opportunity to do research in a highly intellectual atmosphere. The culture, discipline and the overall environment set up by the department has always been pleasant, motivating and of high quality. I am grateful for being able to learn from some of the best professors in the country.

I would like to thank Robert Bosch Centre for Cyber Physical Systems (RBCCPS) for providing me necessary funds to do most part of my research. I also thank Mr. Raghavan, proprietor of Electrical and Allied Products, Bangalore, for taking time from his busy schedule and arranging his working staff so as to help me with braiding the silicone tubes used in this work. To know that his gesture is only motivated by his enthusiasm to see progressive research from young students has always been inspiring! I would also like to thank Aditya and Shanthanu for their initial contributions to this research.

A bunch of thanks to my labmates in Robotics lab, especially Ashith, Midhun, Bose, Don and Arka for their valuable support—both professional and personal— and also for making research enjoyable and entertaining. I have made a lot of friends since I joined IISc, and all of them have had a part in shaping up an unforgettable set of good memories throughout the years. Without the help, positivity and rational advice of Aswin N, it would have been impossible for me to endure all the mandatory tough situations encountered during PhD. Be it the harder levels of Klueless or the tensed scene of being chased down by Frost troll in Skyrim,

his judgement always helped us get through! I also thank the PD gang—especially Mandela, Akki, Haris and Jahfer for making life at IISc fun filled. I also thank SIMA football league and Rhythmica for providing me opportunities to take part in their programmes.

Finally, and more importantly, I thank my parents and siblings for their persistent care and support. I also appreciate them being considerate and reducing the extend of conversations about ‘getting married’ to less than ten minutes whenever I am home! They are the best.

Abstract

Endoscopy is a procedure by which a long flexible device called the ‘endoscope’ is inserted into a patient’s gastro-intestinal(GI) tract primarily for diagnosis. An endoscope is typically equipped with a camera, fiber-optic lighting system and nozzle for spraying water or pumping air. Most commercial endoscopes are also equipped with a catheter channel for passing instruments (catheters) for specific treatments and diagnostic procedures. The thesis aims at addressing two common issues faced by endoscopists: 1) Actuation and positioning of the catheter tip at a desired location while maintaining a stationary camera focus and 2) Manoeuvring the endoscope inside the stomach while avoiding the curling of scope and perforation of tissue walls. Efficient methods to solve these problems could reduce the procedure time and hence, overall discomfort experienced by the patients.

In order to address the first problem, a flexible end-effector for independently actuating the catheter is developed and analysed. The design uses miniaturized pneumatic artificial muscles (MPAMs) for actuating the end-effector. For analysis and implementation, a mathematical model which accurately predicts the pressure-deformation characteristics of MPAM is necessary and hence, a detailed survey on existing models for PAMs as well as MPAMs was conducted. Comparison between static characteristics of PAMs obtained from different phenomenological models in the literature and experiments conducted on the in-house fabricated MPAMs show that the existing models are either inaccurate or inconsistent with changes in fabrication parameters of MPAMs. Hence, a new and improved mathematical model for the pressure-deformation characteristics of MPAM is derived. For MPAMs with less than 2 mm diameter and lengths ranging from 40 mm to 70 mm, it is shown that the developed model could consistently predict the deformation characteristics of the prototype with less than 5% error.

An end-effector prototype which uses three MPAMs for actuation is fabricated and tested. The prototype which is 55 mm long with an outer diameter of 8 mm could deflect a commercial forceps catheter tip by about 20 mm in different directions. An iterative scheme for the forward kinematics of end-effector which takes into account the static characteristics of MPAMs is also developed. The forward kinematics model could predict the final pose of the end-effector with

a maximum error of 2 mm at the tip. An inverse kinematic strategy, using the projection of the workspace of the end-effector is developed and the end-effector actuation is implemented in real-time, taking input from a thumb-stick.

The second problem faced in endoscopy is partially addressed by proposing the use of a multi-segmented continuum endoscopic robot. To this end, a new optimization based approach to solve forward kinematics of a single segment of the robot is presented at first. Actuation of the continuum robot in 2D plane is mathematically proven to provide the exact configuration as that obtained from differential geometry based methods. Simulations conducted with different number of segments also validate the same, barring the cumulative errors arising from the numerical solution procedure. The method is extended to 3D and is also verified using numerical simulations. For the multi-segmented robot, a motion planning algorithm to confine the travel of the robot within the GI tract is developed. Different methods to represent ducts in 2D and 3D are discussed and a tractrix based optimization scheme is developed for each representations. Motion of an endoscope through GI tract is simulated using a GI tract profile obtained from the CT scan data of human viscus. The proposed method is shown to confine the movement of the endoscope within the tract, while emulating realism.

Contents

Acknowledgements	i
Abstract	iii
Contents	v
List of Figures	viii
List of Tables	xii
1 Introduction	1
1.1 Motivation	1
1.2 Contributions of the thesis	10
1.3 Preview of the thesis	11
2 A survey on static modelling of pneumatic artificial muscles	13
2.1 Introduction	13
2.2 Review of static modeling of PAMs	14
2.2.1 Basic modeling strategies	16
2.2.2 Correction factors for Gaylord's model	17
2.2.3 Inclusion of material properties for bladder: linear elastic model	19
2.2.4 Inclusion of material properties for bladder: non-linear elastic model	20
2.2.5 End-effects consideration	22
2.2.6 Bladder as a thin walled tube	23
2.2.7 Advanced modeling of PAMs	24
2.2.8 Modeling MPAMs	26
2.2.9 Empirical considerations	27
2.2.10 Modeling hysteresis	29

2.3	Conclusions and summary of review	31
3	Fabrication and characterization of miniaturized PAMs	34
3.1	Introduction	34
3.2	MPAM characteristics and experimental set-up	35
3.3	Proposed statics model for MPAM	39
3.3.1	Characterization of pressure dead-band	39
3.3.2	Model for first phase-expansion	39
3.3.3	Model for second phase-contraction	42
3.3.4	Summary of proposed model	47
3.4	Experimental validation of proposed model	48
3.5	Conclusions	53
4	Design, fabrication and analysis of flexible end-effector for endoscopic catheters	54
4.1	Introduction	54
4.2	End-effector design	56
4.3	Forward kinematics of end-effector	58
4.4	Experimental validation	62
4.5	Inverse kinematics of end-effector	68
4.6	Real-time implementation of end-effector actuation	72
4.7	Implementation examples	74
4.8	Conclusions	75
5	Motion planning of endoscopic robots	76
5.1	Introduction	76
5.2	Kinematics model for continuum robot	77
5.2.1	Forward kinematics of 2D continuum robot	78
5.2.2	Forward kinematics of 3D continuum robot	81
5.3	Motion planning of endoscopic robot	86
5.3.1	Overview of tractrix based motion planning	86
5.3.2	Motion planning through planar ducts	89
5.3.2.1	Representation of duct using super-ellipses	89
5.3.2.2	Representation of duct as a set of connected quadrilaterals	91
5.3.2.3	Representation of duct using two non-intersecting continuous curves	95
5.3.3	Motion planning through 3D ducts	96

5.3.3.1	Representation of duct as a combination of super-ellipsoids . . .	96
5.3.3.2	Representation of duct as a set of connected cylinders	97
5.3.3.3	Representation of duct using point clouds	97
5.3.4	Simulation of motion through GI tract	98
5.3.5	Limitations of the tractrix based scheme	99
5.4	Conclusions	101
6	Conclusions and Future work	103
6.1	Summary	103
6.2	Scope for future work	105
	Appendix	107
A	Analytical expressions for u, v for quadrilateral patch	107
B	Parametric equation of solid cylinder	107
C	Tractrix emulates natural motion	108
	Bibliography	110

List of Figures

1.1	Bozzini's Lichtleiter [3]	2
1.2	Commercial endoscope	3
1.3	Different catheters used in endoscopic procedures	4
1.4	Difficulties associated with endoscopy	4
1.5	(a) Actuation of PAM [25] (b) PAMs used in a robot arm [26]	6
1.6	Elephant trunk robot [65]	8
2.1	MPAM nomenclature	15
3.1	Fabricated miniaturized pneumatic artificial muscles–1.5 and 1.2 mm diameter	35
3.2	MPAM before and after pressurization	36
3.3	Layout of pneumatic circuit and controller	37
3.4	Experimental set-up for MPAM characterization	38
3.5	MPAM hysteresis profile	38
3.6	Deformation phases of MPAM (inset – elongation part zoomed)	40
3.7	MPAM statics	43
3.8	Braid statics	44
3.9	Area of contact between silicone tube and braided sleeve	46
3.10	End-effect due to braiding	46
3.11	Experimental validation for 40 mm MPAM $\theta_0 = 36^\circ$, $r_i = 0.25$ mm, $r_o = 0.55$ mm, $r_n = 0.04$ mm, $m = 30$, $\phi = 5$ mm, $E = 0.35$ MPa, $\nu = 0.499$.	49
3.12	Experimental validation for 60 mm MPAM. $\theta_0 = 36^\circ$, $r_i = 0.25$ mm, $r_o = 0.55$ mm, $r_n = 0.04$ mm, $m = 30$, $\phi = 5$ mm, $E = 0.35$ MPa, $\nu = 0.499$.	49
3.13	Experimental validation for different angle of windings $l_o = 40$ mm, $r_i = 0.25$ mm, $r_o = 0.55$ mm, $r_n = 0.04$ mm, $m = 30$, $\phi = 5$ mm, $E = 0.35$ MPa, $\nu = 0.499$.	50
3.14	Experimental validation for MPAM wound at 38° angle. $r_i = 0.25$ mm, $r_o = 0.55$ mm, $r_n = 0.04$ mm, $m = 30$, $E = 0.35$ MPa, $\nu = 0.499$.	50

3.15	Experimental validation for MPAM with tube O.D 1.5 mm. $\theta_0 = 35^\circ$, $r_i = 0.25$ mm, $r_n = 0.04$ mm, $m = 30$, $E = 0.35$ MPa, $\nu = 0.499$.	51
3.16	Axial force vs displacement comparison $P_i = 758$ kPa, $\alpha = 36^\circ$, $l_o = 45$ mm, $r_i = 0.25$ mm, $r_o = 0.55$ mm, $r_n = 0.04$ mm, $m = 30$, $\phi = 5$ mm, $E = 0.35$ MPa, $\nu = 0.499$	51
3.17	Evolution of final braid angle for large pressure range	52
4.1	Conceptual design of endoscopic tip assembly	55
4.2	End-effector Design	56
4.3	Design with separate catheter	57
4.4	End-effector prototype with forceps	58
4.5	Tendon driven robot analogy	59
4.6	Backbone-actuator profile	59
4.7	Displacement vector addition	61
4.8	End-effector profile reconstruction using image analysis	63
4.9	Angles showing MPAM arrangement in the end-effector	63
4.10	MPAM R actuated at 689.4 kPa	64
4.11	MPAM G actuated at 689.4 kPa	65
4.12	MPAM G actuated at 551.6 kPa	66
4.13	MPAMs R, G actuated at 689.4 kPa	67
4.14	MPAM G at 689.4 kPa and R at 413 kPa	69
4.15	End effector with forceps at 827 kPa	69
4.16	Pressure vs deflection, with catheter	70
4.17	Front view of end-effector	70
4.18	Projected workspace of end-effector	71
4.19	Vector in projected workspace	71
4.20	Experimental vs theoretical comparison of deflection in random direction	72
4.21	Deflection in resultant direction	72
4.22	Vector outside workspace	73
4.23	Tracing line in workspace	74
4.24	Tracing circle in workspace	74
5.1	Discretization of robot in 2D plane	78
5.2	Nomenclature for single segment	78
5.3	variation of β with θ	79
5.4	Assembly of 4 bar linkages for iteration procedure	80

5.5	Comparison between analytical and optimization based solutions	82
5.6	Solution with increased number of segments	82
5.7	Discretization of robot in 3D	82
5.8	Nomenclature of segment in 3D	82
5.9	Profile of robot with cables actuated by equal displacements. (Black lines for analytical solution and blue lines for optimization based solution)	84
5.10	Profile of robot with cables actuated by different displacements. (Black lines for analytical solution and blue lines for optimization based solution)	85
5.11	Tractrix curve in 2D with one link	87
5.12	Tractrix with multiple links	87
5.13	Obstacle avoidance in a plane	89
5.14	Super ellipses	90
5.15	Duct modeled as a combination of super-ellipses a through e – red: outer boundary, blue: desired path of head	90
5.16	Motion through duct modelled as combination of super-ellipses	91
5.17	Effect of gradient of inequality constraint in pulling the tail into the duct	91
5.18	Duct represented by stitched quadrilaterals A_1 through A_6	92
5.19	Example of constrained motion of a 40 link robot with stitched quadrilaterals	94
5.20	Effect of gradient of inequality constraint in pulling the tail into the quadrilateral duct	94
5.21	Example of analytical duct	95
5.22	Motion through analytical duct	95
5.23	Super-ellipsoids	96
5.24	Fitted ellipsoids	98
5.25	Fitted cylinders	98
5.26	Point clouds	98
5.27	GI tract as collection of super-ellipsoids	99
5.28	GI tract with connected cylinders	99
5.29	Motion of endoscope through GI tract	100
5.30	Infeasible link length	101
5.31	Traversability of a curve	101
5.32	Feasible link lengths	101
B.1	Parameters of a general cylinder	108
C.2	Tractrix emulating the motion of a bicycle chain on photo paper, $\nu = 0.95$	109

C.3	Tractrix emulating the motion of a bicycle chain on gravel, $\nu = 0.86$	109
-----	--	-----

List of Tables

2.1	Summary of phenomenological models of PAM	33
4.1	Forward kinematics iteration for MPAM- <i>R</i> at $P_i = 689.4$ kPa	64
4.2	Forward kinematics iteration for MPAM- <i>R</i> at $P_i = 689.4$ kPa with MPAM de- formation correction	65
4.3	Forward kinematics iteration for MPAM- <i>R</i> at $P_i = 551.6$ kPa	66
4.4	Forward kinematics iteration for $P_i = 413.6$ kPa	68

Chapter 1

Introduction

1.1 Motivation

According to the paper by Spaner and Warnock [1], the concept of using mechanical means to visualize interior organs of a human body started as early as the 10th century A.D. and the earliest device was arguably the invention by an Arab physician, Albukasim where reflected light is used to view human cervix. Little progress was made from this initial concept till the introduction of a light transmitting device –“Lichtleiter” by Italian-German physician Philip Bozzini in 1805 which kick started the evolution of the ‘endoscope’—an instrument used for examining the interior of hollow viscus (see [2], Fig. 1.1) . The term ‘endoscopy’ would later be referred to the study performed using endoscopes. The endoscopes fabricated in the early 18th century consisted of light chambers which were illuminated using wax candles or burning continuous wicks. From the light chambers, a tube filled with prisms or mirrors was introduced to shallow orifices in body such as urethra and urinary bladder. The first esophagoscopy procedure was conducted in 1868 by German physician Kussmaul by overcoming the difficulty of manoeuvring the scope through the neck by appropriately positioning the patient’s head. Later, the illumination method was improvised using electrically heated platinum wire while cooling the surroundings with a continuous flow of cold water. With the invention of Edison’s incandescent electric bulb, straight rigid tubes with light bulb at the tip was developed. Straight tubes were quite popular and were in use till the second half of the 20th century till the development of optical fiber cables. As the procedure became more popular afterwards, specific terms such as bronchoscopy, rhinoscopy, cystoscopy and gynoscopy evolved for inspecting distinct body parts and the term endoscopy became largely associated to inspecting the gastrointestinal(GI) tract.

Through the hundred years from its invention, the endoscope has undergone many technological advancements in terms of lighting and visualization. As opposed to its predecessors,



Figure 1.1: Bozzini's Lichtleiter [3]

a modern endoscope is a single flexible tube, about 1–2 meters long, with diameters ranging from 9 mm to 12 mm (see Fig. 1.2). A commercial endoscope is equipped with a camera which provides real-time visual feedback from the point of view of endoscope tip and a LED based lighting system for illumination. A nozzle is also present which could spray a stream of water and blow air so as to clean the camera lens and the tissue under observation. The air pump which uses carbon dioxide is also used to inflate sections of the GI tract whenever required [4]. One or two thumb wheels attached at the holding end of the scope can be operated so as to actuate the distal end of the endoscope (about 10 cm length from the tip) in vertical as well as horizontal directions. This way, it is possible to orient the camera to a desired location for better perspective. The thumb wheels also act as a means to steer the distal part of endoscope aiding the manoeuvrability. Apart from these basic components, most of the commercial endoscopes also contain one or more channels through its length whereby specific instruments—also called catheters—can be inserted. The catheters are long flexible mechanisms of about 2.5 mm outer diameter which can be inserted from the holding end of the endoscope and can pass through the catheter channel. The mechanism at the distal end of catheter protrudes from the distal tip of endoscope and based on the mechanism, different procedures can be performed such as removing foreign bodies from the tract, collection of tissue samples and treatments such as ablation, ligation, stenting etc.(see Fig. 1.3). With the development of different catheters, endoscopes have evolved from using the basic gripping tool for removing foreign objects in the tract or for collecting samples for biopsy, to state-of-the-art techniques such as endoscopic ultrasound



(a) Endoscope by Olympus [5]



(b) Distal end of an endoscope [5]

Figure 1.2: Commercial endoscope

where the doctors can visualize areas in the body which are otherwise anatomically difficult to access without surgery.

The motivation for the work presented in this thesis comes from partially addressing two issues faced by doctors while performing endoscopy.

1. When the distal end of an endoscope is deflected using the thumb wheels, not only the camera, but the tip of the catheter also deflects along with it. Hence every time a catheter has to be positioned at a required position and orientation, the camera focus will change. The motion dependency between the camera and the catheter tip makes the precise positioning of catheter non-trivial and sometimes difficult, especially when there are more than one catheters deployed at the same time (see Fig. 1.4(a)).
2. Another challenge in endoscopy is manoeuvring the scope in the stomach region. While the forward feed is provided by manually pushing the tube from the dorsal end, sometimes the scope has to be twisted from the holding end in order to guide the tip for motion in transverse direction [9]. This procedure is usually difficult and non-trivial task even for experienced endoscopists (see Fig. 1.4(b)). Since the guidance of scope is provided only by the curvature of the walls, it is very common that the distal section of the scope coils itself inside the stomach when reaching for the intestine section¹(see Fig. 1.4(c)).

¹Identifying the starting end of intestine is itself a challenging task and the accuracy mostly depends on the doctor's experience. Once the intestine is identified, the doctors hook the endoscope tip at the entry of the

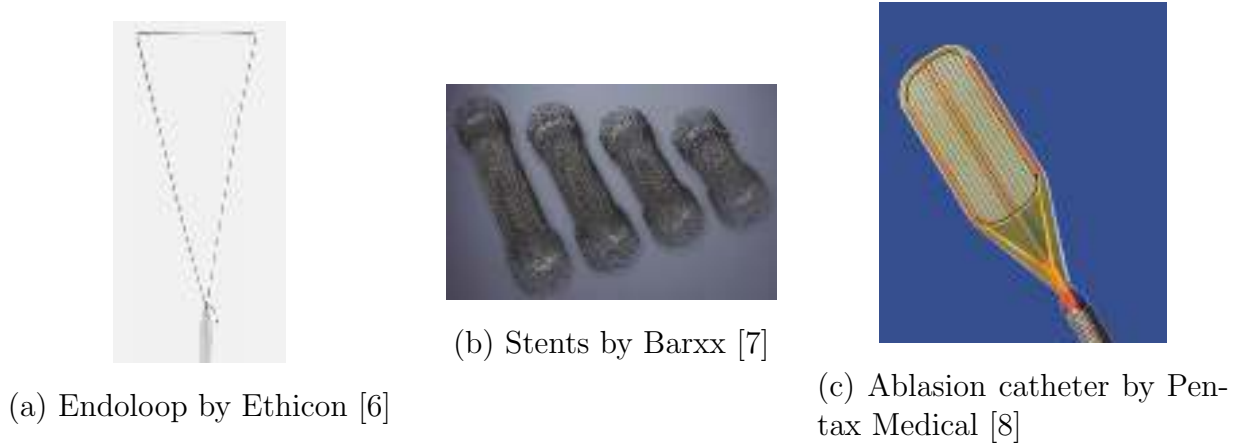


Figure 1.3: Different catheters used in endoscopic procedures

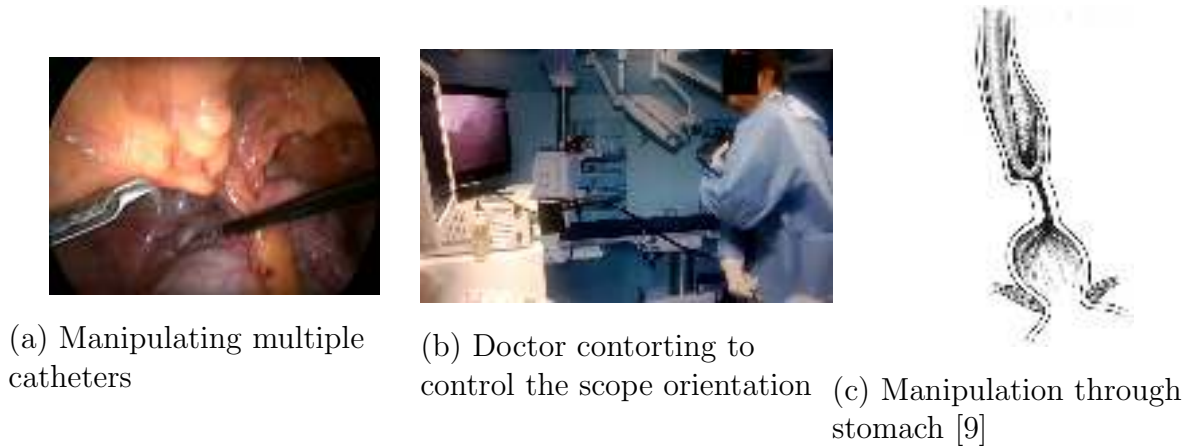


Figure 1.4: Difficulties associated with endoscopy

Uncontrolled manoeuvring could also lead to perforation of the walls of the GI tract [10].

An endoscope design which addresses these limitations will reduce the procedure time and hence, the discomfort experienced by the patients.

The first difficulty can be addressed by providing some means to actuate the distal tip of the catheter independent of the camera. A miniaturized end-effector integrated to the endoscope tip which can be actuated from the holding end of the scope will enable the endoscopists to manipulate the catheter tip without altering the camera focus. Since the camera is usually positioned at around 50 mm from the region under inspection, the length of such an end-effector may be limited to less than 50 mm. Considering the size of the endoscope, the actuator along with the catheter should be less than about 8 mm in diameter. Also, flexible mechanisms

intestine—locking the scope— and pull the scope in order to shorten its working length and also to straighten it. Unless this procedure is carried out, the scope curls inside the stomach on further pushing.

may be preferred over rigid systems so as to avoid the end-effector scratching the tissues and causing perforation.

Conventional actuation techniques are not quite suitable in actuating endoscopic catheters since both precise control and flexibility are desired at a miniature size. At present, the tip of endoscope is moved by pulling a set of cables (tendons), which actuate a series of universal joints [11]. This technique is made use of in a few NOTES (Natural Orifice Translumenal Endoscopic Surgery) platforms [12]. The main disadvantage of actuating the end-effector with cables is that the end-effector becomes stiff in the actuated state and compliance has to be actively controlled [13]. The use of micro-motors is ruled out since it increases the weight at the tip of endoscope apart from making the end of the scope rigid. Shape memory alloy (SMA) wires have the required flexibility and precise positioning capability ([14], [15], [16]). However, the response time of SMA wires for heating and cooling could be of the order of a few seconds which would make the procedure lengthier. Also, the temperature increase due to heating of SMA wires for their actuation is not desirable. These reasons demand the use of unconventional actuating mechanisms in the end-effector. Soft actuators pose a good candidate for this application since the actuator could be non-stiff in the un-actuated state and compliant in the actuated state [17]. Soft actuators have definite advantages over rigid manipulators working in unstructured, cluttered and fragile environments which have made them a fast growing topic in robotics research. Detailed review on different soft robotics actuators can be found in references [18], [19], [20] and [21].

In 1958, Richard H. Gaylord patented a ‘Fluid Actuated Stroking Device’ which is ‘an expansible chamber device comprising a bladder confined within a braided sheath...adapted to be energized by a fluid’ [22]. The bladder which is sealed on one end is made of flexible material and the braided sheath is usually woven using in-extensible fibers. The device, which is essentially a linear actuator has an interesting property that if the angle at which the outer sheath is braided differs from a particular locking angle, the device contracts or expands upon pressurization of the fluid contained in the bladder. This invention gained popular attention when it was later used by McKibben in a design of orthotic wheelchair [23]. Due to the similarity of this flexible actuator with biological muscles, the device is often identified by the name ‘McKibben Muscles’ or ‘Fluidic Artificial Muscles (FAMs)’. For several years, these muscles did not achieve much commercial success probably due to the bulky accessories which are required to energize the system or due to the faster progress in the development of electric motors and other actuators. More recently since the 1980s, the actuators have regained its commercial and academic attention due to its unique advantages. The FAMs which make use of pressurized air are also called ‘Pneumatic Artificial Muscles (PAMs)’ and are now extensively



Figure 1.5: (a) Actuation of PAM [25] (b) PAMs used in a robot arm [26]

studied by engineers especially in the field of bio-inspired and medical robotics (Figure 1.5). In [24], the authors have listed in detail, the major developments towards the evolution of Pneumatic Artificial Muscles.

Among the different types of conventional actuating mechanisms such as electric motors, pneumatic pistons, shape memory alloys etc. as well as the other flexible actuators used in robots [27], artificial muscles stand out due to their following advantages:

- High power to weight ratio: The earliest commercial PAM called ‘Rubbertuator’ by Bridgestone corporation and Hitachi weighed about 6 kg and could lift a mass of approximately 2 kg (refer [28], [29]). At present, the PAMs manufactured by companies like Festo [26] has a lifting force of 6000 N while weighing only about 800 grams.
- Flexibility and compliance: An unpressurized PAM exhibits the same flexibility as that of the bladder but it becomes stiff while remaining reasonably compliant upon pressurization. This compliance is a necessity for the development of medical devices such as minimal invasive surgical tools ([30], [31], [32]) and rehabilitation robots (refer [28], [33], [34]).
- Compatibility with human environment: The primary actuation mechanism of PAM is pressurized air or pressurized inert gas. Hence, it is safer compared to other devices which use electricity, heat or chemically active substances. The only practical safety concern regarding PAM could be the rupture of inner bladder under high pressure. However, by controlling volume flow rate of air into PAMs, this issue can be addressed.
- Low cost in fabrication: A simple PAM could be fabricated from inexpensive off-the-shelf materials. Hence the manufacturing cost of PAMs is very low compared to other actuators

in the same functionality regime. However, it may be noted that PAMs require pneumatic circuitry which increases the initial cost.

Due to the above mentioned advantages, PAMs have found many applications in the robotic industry. A detailed survey on robots which make use of PAMs spanning the domains such as biologically inspired robots, rehabilitation devices, industrial robots, exoskeletons and aerospace applications can be found in [35]. Particularly interesting are the miniaturized versions of PAMs, also called MPAMs, where the diameter is less than 5 mm. Due to the small size, these actuators are used in different applications such as wearable hand exoskeletons [36], cardiac compression devices [37], tool manipulation in surgical devices ([38], [39], [31]) etc. Miniaturized PAMs of diameter less than 2 mm can be bundled into an organized muscle structure for lifting heavy loads. An advantage of using multiple PAMs as bundle or in parallel is the ability to recruit selected muscles as per the load requirement. The variable recruitment technique of muscle bundles is more energy efficient compared to a single muscle of equivalent capacity and are studied in references [40], [41], [42], [43] and [44]. It is shown in [45] that bundling MPAMs exhibit better contraction ratio compared to a single muscle of same diameter. By adjusting the braiding characteristics of PAM or by clubbing two PAMs with different characteristics, the PAM could generate a moment resulting in bending actuators (refer [46], [47], [48]). These references suggest that a flexible end-effector designed with MPAMs as their main actuation technique could prove to be an effective means to address the problem of independent actuation of catheter.

The second problem of maneuverability of endoscope can be addressed by converting the entire length of the scope as a redundant serial robot and actively controlling the configuration of the robot while the endoscopic robot travels through the GI tract. The concept of robot assisted medical procedures such as in robotic surgery [49] is gaining high momentum since they provide stable control with less error and high repeatability [50]. Apart from surgical robotics, hyper-redundant robots also find their application in search and rescue operations, industrial pipeline inspections and also in bio-inspired robotics and hence, considerable efforts are being made towards the research and improvement of the same (please see [51], [52], [53], [54], [55], [56], [57] and [58]). A hyper-redundant endoscopic robot could be designed as a set of rigid links actuated using motors as is the case of a snake like robot [59], as a multi-segmented continuum robot [60] or a concentric tube design [61], [62]. The major challenge in the first two cases is in conforming the dimensions of the robot to the dimensions of a commercial endoscope and in incorporating a large number of joints within the given length of an endoscope. The limitation is more prominent in case of motor-actuated robot compared to continuum robot. In case of concentric tube design, different pre-formed concentric tubes are telescopically actuated and hence, the



Figure 1.6: Elephant trunk robot [65]

actuated configuration of the robot depends on the manner in which the tubes are deformed and hence limits the dexterity. In an application point of view, out of the different robot designs, continuum robot seems to be the best choice for the application in hand since the robot will be lighter in weight and flexible, which are desirable properties for an endoscope.

Continuum robots are generally serial robots which use flexible links instead of rigid links which make it ideal for the fabrication of endoscopic robot. Since the degree of freedom of such robots are infinite, they possess all the advantages of a hyper-redundant robot. A detailed review on the design, history and applications of continuum robots can be found in [63] and [64]. One of the earliest continuum robot developed was the Rice/Clemson ‘elephant-trunk’ robot shown in [65] (refer Fig. 1.6). The robot which resembles a spinal column structure consists of a flexible backbone whose pose can be adjusted by pulling a set of cables attached to it. The robot is made of multiple segments and each segment can be actuated using a set of four cables which are placed 90° apart from each other. Guide disk attached at regular intervals on the backbone routes the cables (tendons) from the base of the robot till the tip of the segment so that the separation between the cables are maintained. By pulling the cable pairs attached to a segment, the segment can be actuated, which assumes the configuration of an arc of a circle. By actuating multiple segments, the continuum robot can take different configurations in 3D. Detailed analysis of the workspace of the robot can be found in [66]. It is also possible to generate special configurations for the actuated continuum robot by varying the tendon routing as shown in [67]. Many advanced flexible robots are modifications of this original concept, with difference mostly in the actuation mechanism (such as pneumatic [26], SMA wires [68]) or the type of backbone (such as serially connected universal joints ([67], [69]), flexible continuous beam [70] or rigid rods connected using compliant joints [71]). While the continuum robots are generally fabricated with segments of equal length, in [72], the authors describe analysis and experiment on robot with varying lengths of segments.

In case of hyper-redundant robots, there are theoretically infinite possibilities to achieve a particular position and orientation of its end-effector. The additional degrees of freedom of a hyper-redundant endoscopic robot can be effectively used in manipulation through GI tract, since it is possible to select a configuration which is confined to the tract without altering the tip position. Identifying a suitable configuration from the many possible configurations, given the position and orientation of the tip constitutes the redundancy resolution of the hyper-redundant robot. For an endoscopic robot, the path through which the tip of the robot has to move can be set as the medial axis of the GI tract. If the path followed by the tip is predetermined, then the redundancy resolution problem also constitutes the motion planning of the robot.

The initial focus of researchers on addressing redundancy resolution problem was to solve the equation relating the end-effector velocity $\dot{\vartheta}$, to the joint rates $\dot{\varphi}$, i.e, $\dot{\vartheta} = J(\varphi) \dot{\varphi}$ where J is the manipulator Jacobian matrix. Primary idea of inverse kinematics is to invert the Jacobian using Moore-Penrose inverse (pseudo inverse) [73]. While this method results in kinematic singularities, methods such as extended Jacobian ([74], [75]) and task prioritized augmented Jacobian [76] are aimed to avoid these singularities and also obtain solutions to inverse kinematic problem by specifying a velocity component at the singular configuration depending on the task at hand. Since the major advantage of using a hyper-redundant robot is to facilitate motion avoiding obstacles and movement in confined spaces, many researchers have worked on this particular task using above mentioned techniques [77]. However, even though the methods avoid singularities in the manipulator Jacobian, it could generate other forms of singularities and also, the method becomes computationally complex for large number of joints [78]. Many other redundancy resolution methods including variational approach, geometric approach, neural networks and fuzzy logic can also be found in the literature ([79], [80], [81], [82]).

In reference [53], obstacle avoidance problem for hyper-redundant manipulator is carried out by fitting a curve through the joints of manipulator and planning the path for this ‘backbone curve’ which avoids obstacles. Finding the pose of the backbone curve directly gives the coordinates of the joints. Hence, in case of obstacle cluttered environments, planning the path of the end-effector which avoids the obstacles will result in redundancy resolution since the trajectory itself forms the backbone curve of the manipulator (see [83], [84], [85], [86]). Even though the backbone curve approach is very simple, end-effector trajectory with many closely spaced kinks may sometimes produce undesirably high accelerations at the joints. The motion will also look un-natural. In reference [87], the authors proposed a tractrix based redundancy resolving algorithm which produces natural looking motion of hyper-redundant robot. It is also shown in [88] that the same can be achieved by minimizing the subsequent motion of the links, given the displacement of the head (end-effector). The tractrix based solution also has

an interesting characteristic that the motion attenuates from the head to the tail(base) of the entire manipulator. For obstacles represented by simple analytical shapes, it is shown in [89] that the algorithm can be effectively used for obstacle avoidance as well.

1.2 Contributions of the thesis

The thesis aims to partially address the two challenges faced by endoscopists: 1) Positioning the catheter tip at a desired location while maintaining a stationary camera focus and 2) Controllable manoeuvring of the endoscope inside the stomach. To this end, the following are the major contributions from this thesis:

1. *A survey on mathematical model for statics of PAMs*

In this work, miniaturized pneumatic artificial muscles are used for actuating a novel end-effector which can impart independent catheter motion. Many researchers have attempted to capture the accurate description of the physics of PAMs which made available a variety of modeling techniques in literature, some of which, even though are not exact representation of the physical phenomena, seem to suit the purpose of application in PAM enabled robots and mechanisms. A thorough survey and documentation of the static modeling considerations for PAM, from the first model mentioned in Gaylord's patent, to the recent models in the literature have been carried out in this thesis.

2. *A new model for miniaturized PAMs.*

A miniaturized pneumatic artificial muscle of outer diameter less than 2 mm is fabricated and tested in-house. Since the existing static models available for pressure-deformation relationship of pneumatic muscles do not conform to the experimentally obtained characteristics of the fabricated MPAM, a new static model for miniaturized PAMs built on the framework of inflation of a linear elastic cylindrical tube is developed. The developed model shows better consistency with the physics of MPAM and hence, the model as well as the modelling strategy opens up a new and different approach in modelling statics of miniaturized PAMs.

3. *A novel flexible end-effector for actuating endoscopic catheters*

Using three MPAMs, a flexible end-effector which can actuate the tip of an endoscopic catheter is designed, fabricated and tested. The 55 mm long end-effector prototype could deflect the tip of a commercial forceps tool by more than 20 mm in all directions. A controller is developed and implemented for real-time actuation of the end-effector and

is shown that it is possible to arbitrarily position the end-effector tip by actuating a thumbstick.

4. *Forward kinematics using optimization methods*

A new optimization based forward kinematics approach is developed using discretization of the entire length of the end-effector and identifying the configuration of segments by comparing them with 4-bar parallel mechanisms. Since MPAM-based end-effector cannot afford the use of guiding discs, the existing theoretical kinematic analyses in the literature were not applicable to the fabricated actuator and the developed model shows good agreement with the experimental results. By changing the minimization function, the same approach could also be used for continuum robots with guiding discs, which is mathematically proved.

5. *Motion planning of hyper-redundant robot in confined spaces*

Different strategies to represent ducts in 2D as well as 3D are discussed. For each stratagem, tractrix based optimization algorithm for redundancy resolution of a hyper-redundant robot, which adheres to the constraint of confinement within the duct is developed. A simulation of motion of endoscope through GI tract is carried out using a model obtained from human CT scan data. The solution based on the derived approach generates a natural-like motion of the robot while travelling through the duct.

1.3 Preview of the thesis

The thesis focuses on two topics which are discussed in detail: 1) The development and analysis of miniaturized pneumatic artificial muscles and a novel endoscopic end-effector. 2) Motion planning of a cable-driven hyper-redundant continuum endoscopic robot. For the first topic, since it is essential to understand the pressure-deformation characteristics of MPAMs for their implementation in an end-effector, and thereby facilitating end-effector control, chapters 2 and 3 are dedicated for this purpose. In chapter 2, a detailed literature review on the static modelling of pneumatic artificial muscles is presented. Due to the incongruence between the experimental results and theoretical results from existing models for statics of MPAM, a new and improved model is developed in chapter 3. The model is found to be more accurate and consistent compared to the existing models in literature. This chapter also discusses the fabrication characteristics as well as the experimental set-up used for the study. Once the MPAMs are characterized, they are employed in a novel design of end-effector for actuating endoscopic catheters. Details of the design and fabrication of the end-effector are discussed in chapter 4.

The chapter also discusses the formulation of a new model for the forward kinematics of the end-effector as well as the validation of the theoretical model using experiments. In chapter 5, the second topic of motion planning of endoscopic robots is discussed in detail. The kinematic analysis of a continuum endoscopic robot is carried out using two study modules. Firstly, a new formulation to describe the forward kinematics of a single segment of cable driven continuum robots is developed and is proven to be in accordance with the solutions found in the literature. Secondly, a novel approach in resolving the redundancy of the multi-segmented continuum robot is developed, with the motion planned such that it is always confined to the interior of the GI tract. A motion simulation conducted on the GI tract profile obtained from an actual human CT scan data is also presented in this chapter. Finally, in chapter 6, conclusions of this thesis as well as the scope for future studies are presented.

Chapter 2

A survey on static modelling of pneumatic artificial muscles

2.1 Introduction

In order to understand the behaviour and influence of MPAM employed in a robot, it is imperative that accurate mathematical description of underlying mechanics is formulated. However, due to the complex interaction of forces in a PAM, this task is not trivial. Nonetheless, many attempts have been made in this regard due to two reasons. Firstly, a mathematical model would help to improve the control system of robots, especially in implementing model based control systems (see [90], [91], [92]). In such cases however, it is desired to have an easily implementable and computationally efficient model to improve the response of the controller. Secondly, a model with sufficient parameters helps to efficiently choose or fabricate an actuator with optimized qualities intended for a particular task. In this case, an accurate model which describes the mechanics of PAM based on actuator dimensions, braiding characteristics, material properties etc. is preferred. Like any other pneumatic systems, PAM exhibits hysteresis which is a major hindrance in modeling statics and dynamics of PAM. Due to static frictional forces and nonlinearity in the material of the bladder, a quasi-static contraction (or elongation) of PAM shows different curves for force vs length and pressure vs length plots for compression as well as decompression of air. In force modeling methods, this additional frictional force is generally added (or subtracted) from a mean curve for contraction (and elongation) of PAM. This frictional force, as may be seen in the later sections of this chapter, are mostly empirically calculated. For modelling the dynamics of PAM, the rate of change of state of PAM is related to the change in input parameters where kinetic friction is also included in the model.

In the review paper by Tondu [93], the author meticulously reviewed the major static and

dynamic modeling improvements carried out by well-known researchers in the field. Starting from the simple and one of the earliest static model proposed by Schulte [94], the author carefully addressed different physical considerations which could improve the basic model such as the inclusion of material properties, non-cylindrical end-effects, representation of PAM as a fiber-reinforced membrane model as well as muscle hysteresis. The author lists the necessary considerations, reasonable assumptions as well as precautions to be taken in deriving the static and dynamic formulae representing the actuation of PAM. However, since the objective of Tondu's paper is to identify accurate means to describe the physics of PAM, a few models in the literature which rely on empirical formulations as well as the models which provide only minor improvements from the standard equations are not detailed in Tondu's article. In this chapter, a thorough review of models which are not mentioned in Tondu's paper is presented.

2.2 Review of static modeling of PAMs

In this section, models used by different research teams to describe the statics of PAM are introduced. Many models which assume quasi-static motion do not consider hysteresis into account since accurate phenomenological description of hysteresis is not yet available and many control system strategies use the mean value between contraction and extension profiles ([90], [95], [96]). As described before, in case of force balance formulations, these hysteresis forces can be added (or subtracted) in case the hysteresis effect is non-negligible. Also, extensile PAMs are not commonly used compared to the contractile PAMs since additional arrangements are required to avoid the buckling effect. In reference [97] the authors compare the performance differences between contractile and extensile muscles. It is shown that the derived mathematical models are valid for extensile muscles as well. Hence, most models stated here will assume the primary actuation mode of PAMs as contractile. Finally a few fundamental models mentioned in Tondu's paper are also discussed here for completeness.

The following nomenclature will be used in the rest of this chapter, unless stated otherwise (refer Fig. 2.1):

l_0 , r_0 and t_0 represent the length, outer radius and thickness of the bladder before deformation, respectively. After deformation, these quantities change to l , r and t . The quantity $r_i = r_0 - t_0$ represents the initial inner radius of the bladder. Initial and final winding angle of braid are denoted as θ_0 and θ , respectively. The symbol N , m and b represent the number of turns of the braid along the length, number of strands of braid as well as the length of a single braid strand, respectively. The symbol P_i represents the input pressure and $\epsilon = \frac{l_0 - l}{l_0}$ represents the strain in the bladder along the axial direction. Notations F and κ will be used to represent force and constants in general.

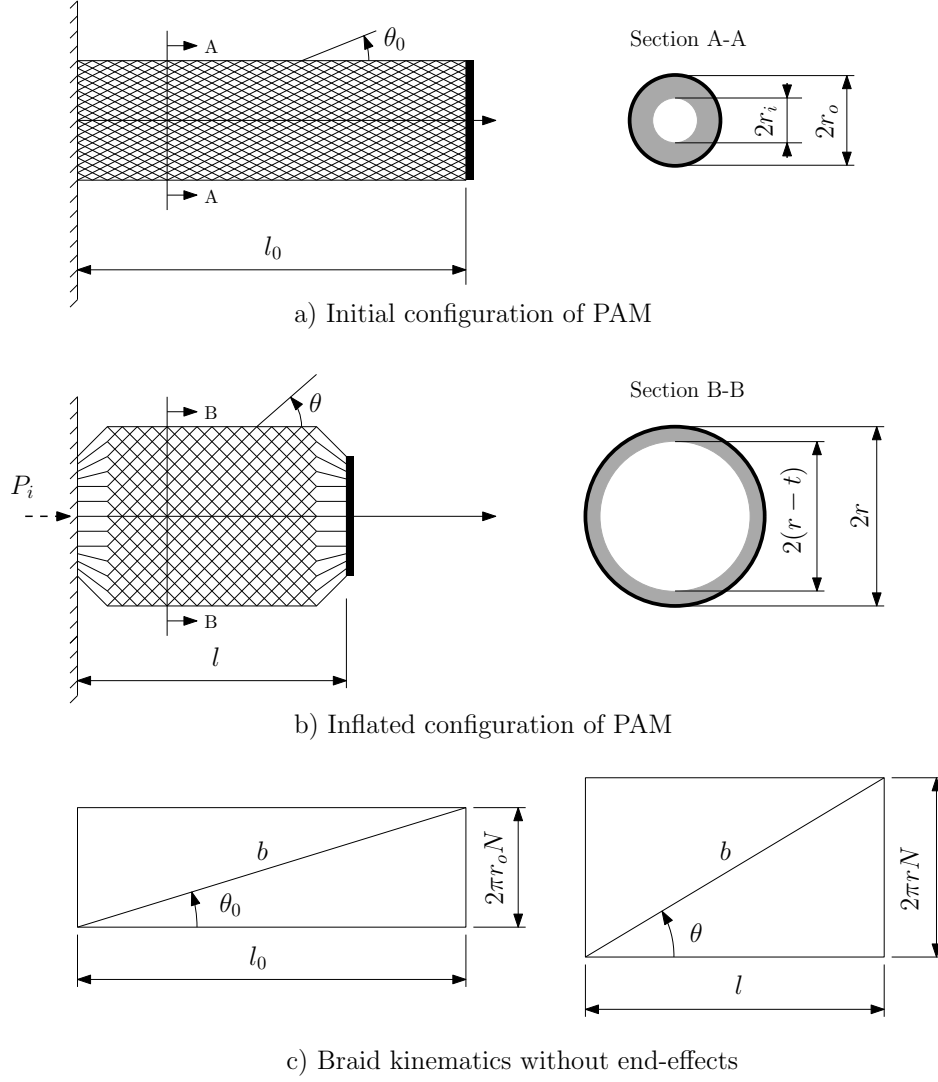


Figure 2.1: MPAM nomenclature

If it is assumed that the PAM remains cylindrical after deformation i.e., if the tapering effects at the ends are not considered, we can write the following equations [98]

$$l_0 = b \cos \theta_0, \quad 2\pi r_0 N = b \sin \theta_0 \quad (2.1)$$

$$l = b \cos \theta, \quad 2\pi r N = b \sin \theta \quad (2.2)$$

In the above equations, it is assumed that the braid is in contact with the outer surface of the tube at all times and the thickness of the braid is neglected. It is also assumed that the braid material is inextensible.

2.2.1 Basic modeling strategies

The earliest mathematical model which takes into account the mechanics of a PAM can be found in Gaylord's patent [22]. For static equilibrium of the compressed muscle, the energy provided by the applied pressure ($P_i dV$) must be balanced by the work done by the PAM which is carrying the load applied at the tip to a particular distance ($F dz$). By expressing the change in volume enclosed by the braided sheath dV and the displacement of the PAM tip dz in terms of the angle of winding, the energy balance formula yield the following expression for force:

$$F_{\text{Gaylord}}^{(1)} = \frac{b^2}{4\pi N^2} P_i (3 \cos^2 \theta - 1) \quad (2.3)$$

In the above equation, the initial cylindrical shape of the bladder is assumed to stay cylindrical even after deformation and the simple kinematic equations of the braid given by (2.1) and (2.2) are used. The above relation gives the value of final braid angle θ for the applied pressure and axial loading from which we can find the final length of PAM using equation (2.2). The limiting value of braid angle (and hence, the length) for which the force exerted is maximum can be found by differentiating the above equation with respect to θ and setting to zero. The value $\theta_{\text{limit}} = 54.7^\circ (54^\circ 44')$ hence becomes a locking angle for deformation of PAM. In other words, a PAM wound with a braid at any initial winding angle will theoretically approach this locking angle with an increase in pressure. This model is also found in the literature in its alternate form,

$$F_{\text{Gaylord}}^{(2)} = \pi r_0^2 P_i [q_1 (1 - \epsilon)^2 - q_2] \quad (2.4)$$

$$q_1 = \frac{3}{\tan^2 \theta_0}, \quad q_2 = \frac{1}{\sin^2 \theta_0}$$

which shows the primary behaviour of PAM as a non-linear spring. In this simplistic and first approximation of PAM statics, the volume occupied by air inside the bladder is assumed to be the same as the volume enclosed by the braided sheath. However, this assumption is an over-estimation of pressure energy since the the volume of air inside the bladder is only the volume enclosed by the cylinder formed by its inner radius. In [98], Chou gives an expression for the force taking into account the thickness of bladder:

$$F_{\text{Chou}}^{(1)} = \frac{b^2}{4\pi N^2} P_i (3 \cos^2 \theta - 1) + \pi P_i \left[\frac{bt_0}{N\pi} \left(2 \sin \theta - \frac{1}{\sin \theta} \right) - t_0^2 \right] \quad (2.5)$$

The experimental comparisons shown in Chou's paper suggest that even though the model is derived based on simplified assumptions, this is a good first approximation. In the coming years, researchers mostly improvised on this basic model by adding correction factors, relaxing the modelling assumptions or by adding force terms arising from other physical phenomena contributing to the statics of a PAM.

2.2.2 Correction factors for Gaylord's model

Gaylord's model assumes the initial cylindrical shape of the PAM to remain cylindrical even after deformation. However, since one end of the PAM is connected to the pressure inlet system and the free end is always sealed, the radial expansion of bladder will be non-uniform. In the clamped ends, the radius of bladder will be the initial radius after deformation. Hence, on either ends of a PAM, the cylinder takes approximately, the shape of a conical frustum. In [99], Tondu modified the basic equation by Gaylord to include a factor ' k_ϵ ' which was intended to account for this non cylindrical tip effects. The force was given as

$$F = \pi r_0^2 P_i [q_1 (1 - k_\epsilon \epsilon)^2 - q_2] \quad (2.6)$$

In their work, to match the experimental results, the factor k_ϵ is chosen as $k_\epsilon = \kappa_1 e^{-P_i} + \kappa_2$, where the constants κ_1 and κ_2 are experimentally calculated. In another work by Itto and Kogiso [100], the value of k_ϵ is chosen as $k_\epsilon = \kappa_1 e^{\kappa_2 P_i} + \kappa_3$ to add more flexibility. In Tondu's model, static frictional force is also included to improve the static characteristics:

$$F_{\text{fstat}} = \mu_s P_i \left(\frac{S_{\text{contact}}^{(1)}}{S_{\text{scale}}^{(1)}} \right) \quad (2.7)$$

where $S_{\text{contact}}^{(1)} = 2\pi r_0 l_0 \frac{\sin \theta_0}{(1 - k_\epsilon \epsilon) \sqrt{1 - \cos^2 \theta_0 (1 - k_\epsilon \epsilon)^2}}$

is the contact surface between the strands of the braid, μ_s is the coefficient of friction between the braid strands and $S_{\text{scale}}^{(1)}$ is a correction factor for the surface area of contact $S_{\text{contact}}^{(1)}$, since the formulation of the contact surface area assumes flat strands of braid. Taking into account these considerations, the force is given as

$$F_{\text{Tondu}} = \pi r_0^2 P_i [q_1 (1 - k_\epsilon \epsilon)^2 - q_2] \pm \mu_s P_i \left[\frac{S_{\text{contact}}^{(1)}}{S_{\text{scale}}^{(1)}} \right] \quad (2.8)$$

where the quantity $S_{\text{scale}}^{(1)}$ is experimentally determined. This model is applied in many works such as in the control system design of a multi joint arm in [95] as well as in variable recruitment

of PAM bundles in [41] and [44].

An improvement in Tondu's model was proposed by Davis and Caldwell [101], by including a more detailed derivation for the surface area of contact between the braid strands. For a PAM of given dimensions and braiding pattern, the surface area is defined in terms of the minimum angle of winding possible in the stretched state (θ_{\min}):

$$S_{\text{contact}}^{(2)} = \frac{b^2 \sin \theta_{\min} \cos \theta_{\min}}{N \sin \theta \cos \theta} \quad (2.9)$$

where

$$\theta_{\min} = \frac{1}{2} \sin^{-1} \left(\frac{r_n m}{\pi r_0} \right), \quad (2.10)$$

with r_n denoting half the diameter of a single strand. Since the contact area calculated in the above equations is also that of flat strands, a scaling factor is used just like in [99]. However, while the scaling factor is empirically determined by Tondu, an attempt to quantify this factor can be found in their work, and the scaling factor is taken as the ratio of surface areas formed by two flat strands in contact to two spheres in contact. The contact between spheres is calculated using Hertz's contact theory and the final scaling factor is given as:

$$S_{\text{scale}}^{(2)} = \frac{r_n}{1.442 \left[P_i r_n^3 \frac{(1-\nu_n^2)}{E_n} \right]^{\frac{1}{3}}} \quad (2.11)$$

where ν_n and E_n represent Poisson's ratio and Young's modulus of the braid strand, respectively. The modified expression for force takes the form:

$$F_{\text{Davis}} = \pi r_0^2 P_i \left[q_1 (1 - k_\epsilon \epsilon)^2 - q_2 \right] \pm \mu_s P_i \left[\frac{S_{\text{contact}}^{(2)}}{S_{\text{scale}}^{(2)}} \right] \quad (2.12)$$

While Tondu added the correction factor term in the form of k_ϵ in Gaylord's equation, in [42], another correction term is added by Meller et al. The expression for force takes the form:

$$F_{\text{Meller}} = \pi r_0^2 P_i k_f^{(1)} \left[q_1 (1 - k_\epsilon^{(1)} \epsilon)^2 - q_2 \right] \quad (2.13)$$

where the the newly added correction terms $k_f^{(1)}$ as well as $k_\epsilon^{(1)}$ are both determined as functions

of input pressure as

$$k_f^{(1)} = k_{f(P_i)}^{(1)} = \frac{F_{\text{meas,max}}(P_i)}{\pi r_0^2 P_i (q_1 - q_2)}, \quad k_\epsilon^{(1)} = k_{\epsilon(P_i)}^{(1)} = \frac{1}{\epsilon_{\text{meas,max}}(P_i)} \left(1 - \frac{1}{\sqrt{3} \cos \theta_0} \right)$$

The quantities $F_{\text{meas,max}} = \kappa_1 P_i + \kappa_2$ and $\epsilon_{\text{meas,max}} = \kappa_3 \ln(P_i)$ are calculated using curve fit on experimental data. This model is applied in the analysis of a climbing robot actuated using FAM in the work of Chapman et al. [102].

While the factors $F_{\text{meas,max}}$ and $\epsilon_{\text{meas,max}}$ contributed by Meller are empirical functions, in [103], Andrikopoulos et al. used constant values to these functions for simplicity. The expression for the force is given as

$$F_{\text{Andrikopoulos}}^{(1)} = \pi r_0^2 P_i k_f^{(2)} \left[q_1 (1 - k_\epsilon^{(2)} \epsilon)^2 - q_2 \right] \quad (2.14)$$

where the factors $k_f^{(2)}$ and $k_\epsilon^{(2)}$ are not functions of pressure, but take the values

$$k_f^{(2)} = \frac{F_{\text{max}}}{\pi r_0^2 P_{\text{test}} (q_1 - q_2)}, \quad k_\epsilon^{(2)} = \frac{l_0}{x_{\text{max}}} \left(1 - \sqrt{q_2/q_1} \right)$$

To get the values of constants, a test pressure P_{test} is applied with zero end load to get the displacement $l_0 - l = x_{\text{max}}$. Then F_{max} is the value of end force which will pull the actuator back to zero displacement position. Both quantities are experimentally determined.

2.2.3 Inclusion of material properties for bladder: linear elastic model

The earliest model which takes into account the material property of the bladder and thickness of the tube is probably that of Schulte [94] mentioned in the appendix of National Research Council's report on the application of external power in prosthetics and orthotics. The force according to this work is given by

$$F_{\text{Schulte}} = \frac{b^2}{4\pi N^2} P_i (3 \cos^2 \theta - 1) + \frac{bE}{N} \left[l_0 \sin \theta - \frac{\cos^2 \theta}{\sin \theta} \left(\frac{b}{N} \sin \theta - 2\pi r_0 \right) \right] - \frac{l_0 b}{N} (P_i - P_u) (\mu_s + \mu_{\text{st}}) \sin \theta \quad (2.15)$$

The first term on the right hand side of the equation (2.15) represents the original pull equation by Gaylord. The second term is the resultant of considering the material properties of the bladder— the constant E being the Young's modulus of bladder material. The third term

represents the friction force where P_u is the pressure required to inflate the unconstrained inner tube to a diameter equivalent to the device diameter at any value of θ . The constant μ_{st} is the coefficient of friction between the braid and the tube. Many researchers have used this model in their study (see, for example, [104]) in a different form:

$$F_{\text{Ferraresi}} = \frac{P_i}{4\pi N^2}(3l^2 - b^2) - Et_0l \left(\frac{1}{N\sqrt{l^2 - b^2}} - \frac{1}{2\pi N^2 r_i} \right) + EA \left(\frac{l}{l_0} \right) \quad (2.16)$$

where A is the cross sectional area of the cylinder.

This model by Ferraresi can also be seen in another format in the works of Kothera et al. [105]. The model derived in their paper, using force balance techniques, is essentially Chou's model which accounts for the thickness of bladder and Schulte's model which considers its linear elasticity. The force according to Kothera et al. is taken as

$$F_{\text{Kothera}}^{(1)} = \frac{P_i}{4\pi N^2}(3l^2 - b^2) + P_i \left(\frac{V_b}{l} - \frac{tl^2}{2\pi r N^2} \right) + EV_b \left(\frac{1}{l_0} - \frac{1}{l} \right) + \frac{El}{2\pi r N^2}(tl - t_0l_0) \quad (2.17)$$

From the experimental data shown in the works of Kothera et al, it is observed that modelling bladder as linear elastic material, even though simplistic, is fairly accurate. This is an interesting observation since this shows that the PAM operation is limited to within the linear regime of deformation of bladders which otherwise usually belong to hyper-elastic material category. Since determining accurate values for constants in non-linear models often require precise experimentation, linear material model may suffice for PAMs undergoing small deformation. However, if the material properties can be accurately described and if extensive computation can be afforded, then non-linear material modelling may provide better accuracy.

2.2.4 Inclusion of material properties for bladder: non-linear elastic model

If the bladder material is considered non-linear elastic, then obtaining analytical expressions of force using force-balancing techniques is difficult (if not impossible). The stress components are obtained from strain energy density functions and are directly used in the balance equations. In reference [106], the authors used a non-linear Mooney-Rivlin material ([107], [108]) to account for the elastic properties of the bladder. The strain energy density of a Mooney-Rivlin material

takes the form:

$$W = C_{10} (\lambda_1^2 + \lambda_2^2 + \lambda_3^2 - 3) + C_{01} \left(\frac{1}{\lambda_1^2} + \frac{1}{\lambda_2^2} + \frac{1}{\lambda_3^2} - 3 \right) \quad (2.18)$$

$$\text{where } \lambda_1 = \frac{l}{l_0}, \lambda_2 = \frac{2r - t}{2r_0 - t_0}, \lambda_3 = \frac{t}{t_0} \quad (2.19)$$

are the three stretch ratios. It may be noted that the median diameter is used in this formulation and the thickness is accounted for, unlike in the model used in [109], where the stretch ratios were defined assuming an incompressible material model and is given by

$$\lambda_1 = \frac{l}{l_0}, \lambda_2 = \frac{r}{r_0}, \lambda_3 = \frac{1}{\lambda_1 \lambda_2} \quad (2.20)$$

The final expression for force is derived from the energy balance equation can be written as

$$F_{\text{Delson}} = P_i \frac{dV}{dl} + V_b \frac{dW}{dl} \quad (2.21)$$

$$\text{and } \pi l t (2r - t) = \pi l_0 t_0 (2r_0 - t_0)$$

where $V = \pi r^2 l$ is the volume occupied by the device and $V_b = \pi l t (2r - t)$ represents the volume of the bladder. Since the above equation cannot be directly integrated, a numerical integration scheme may be required for the solution.

The Mooney-Rivlin material model can also be found in [105] where an energy balance method is used to derive the following expression for force:

$$\begin{aligned} F_{\text{Kothera}}^{(2)} = & \frac{P_i}{4N^2\pi} (3l^2 - b^2) - V_b \left(2C_{10} \left[\lambda_1 \frac{d\lambda_1}{dl} + \lambda_2 \frac{d\lambda_2}{dl} + \lambda_3 \frac{d\lambda_3}{dl} \right] + \right. \\ & \left. 2C_{01} \left[\lambda_1 (\lambda_2^2 + \lambda_3^2) \frac{d\lambda_1}{dl} + \lambda_2 (\lambda_3^2 + \lambda_1^2) \frac{d\lambda_2}{dl} + \lambda_3 (\lambda_1^2 + \lambda_2^2) \frac{d\lambda_3}{dl} \right] \right) \\ & - \frac{P_i^2 b^3 l}{4\pi^2 m r_n E_b N^4} \end{aligned} \quad (2.22)$$

where the quantity E_b is the Young's modulus of braiding material. An application of this model can be seen in the works of Wereley's team [110] where PAM is used to produce large trailing edge flap in a helicopter. To this model, a friction force of the form $F_f = -\mu_f F_{\text{Kothera}} \text{sgn}(v)$ is added to Kothera's model where v is the tip velocity of PAM and the constant μ_f (which is not the coefficient of friction) is found out from experiments. It is worth noting that the authors suggest the use of derivations using force balance method compared to energy balance method since the former was shown to have a better performance compared to the latter [105].

In reference [111], a neo-Hookean material [112] is assumed for the bladder which gives the strain energy density in terms of the stretch ratios as

$$W = \frac{E}{6} (\lambda_1^2 + \lambda_2^2 + \lambda_3^2 - 3) \quad (2.23)$$

Due to the relative simplicity in the material definition as opposed to the Mooney-Rivlin model, the authors could derive analytical expression for pressure in terms of deformation as

$$P_i = \frac{E}{3} \left(\frac{r_0^2}{r_i^2} - 1 \right) \frac{\left(\lambda_1^8 \cos^4 \theta_0 \cos 2\theta_0 - 2\lambda_1^6 \cos^2 \theta_0 \cos 2\theta_0 + \lambda_1^4 \cos 2\theta_0 + 2\lambda_1^2 \cos^2 \theta_0 \cos 2\theta_0 - \cos 2\theta_0 - 2\lambda_1^2 \cos^6 \theta_0 + \cos^4 \theta_0 \right)}{\lambda_1^3 (1 - 5\lambda_1^2 \cos^2 \theta_0 + 7\lambda_1^4 \cos^4 \theta_0 - 3\lambda_1^6 \cos^6 \theta_0)} \quad (2.24)$$

From the above equation, for a given value of input pressure, the axial stretch ratio is calculated numerically. This is then used in the calculation of the force using the following force formulation:

$$F_{\text{Trivedi}} = \pi E (r_0^2 - r_i^2) (\lambda_1 - 1) \quad (2.25)$$

The above expression however, makes the assumption that the material is linear elastic in the axial direction, which is inconsistent with the initial assumption for deriving the expression for pressure.

Another description of static model considering Mooney-Rivlin material model can be found in [113] by Wang et al. In their model, the Hoop's force F_z and axial force F_θ acting on bladder during inflation are found analytically in terms of λ_1 and P_i . These values in conjunction with the static force balance equations from braid, gives the final expression for blocked force (applied load) as

$$F_{\text{Wang}} = F_z - P_i \pi r_i^2 - \frac{P_i r_i l^2 - F_\theta l^2}{2\pi N^2 r_o^2} \quad (2.26)$$

2.2.5 End-effects consideration

In the models described so far, the correction factor k_ϵ was used to take care of the effects of non-cylindrical ends. A few researchers have attempted to quantify this effect hoping to obtain better static characteristics of PAM. For example, in [114], the model developed considers the end-effect of PAM with ends modeled as conical frustums. The mathematical model derived

takes the form:

$$F_{\text{Doumit}} = m \left[\begin{aligned} & \left(\frac{P_i(r-t_0-2r_n)-\sigma_1 t_0}{mN \sin \theta} \right) l_{\text{cyl}} \\ & + \left(\frac{P_i(r+r_c-2t_0-2r_n) \cos \beta - 2\sigma_1 t_0}{mN \sin \left(\frac{\theta+\theta_c}{2} \right)} \right) l_{\text{cone}} \\ & - \frac{P_i(r-2r_n-t_0)^2}{2mr \cos \theta} \frac{l}{N} \tan \theta \end{aligned} \right] \cos \beta \cos \theta_c - PS_{\text{contact}}^{(2)} \mu_s \quad (2.27)$$

The first term in the expression refers to the model taking into account the characteristics of conical ends while the second term is the frictional force component (σ_1 is the Hoop's stress on the bladder). The symbol l_{cyl} refers to the length of cylindrical section of PAM, l_{cone} refers to the slant length of conical frustum at the ends and r_c refers to the radius at the clamped end of the PAM. The quantity $S_{\text{contact}}^{(2)}$ is the effective area of contact between braids which is calculated by assuming the contact to be same as the contact between two cylinders and applying Hertz's contact theory. The validity and propriety of this assumption is, however, criticized in Tondu's review paper [93].

A more involved formulation for end tapering can be found in [90] where the force model used is the same as the one suggested by Ferraresi and found in [115] and [105]. At the ends, the bladder is assumed to take the shape of a section of elliptic toroid instead of conical frustum. The section of ellipse from $\pi/3$ radians to $\pi/2$ radians measured from the major axis is assumed to be the shape of PAM at the clamped ends. An expression relating the deformed radius of PAM with the eccentricity of ellipsoid is derived. Making use of this expression, a theoretical estimate for the length of a single strand of braid is formulated. By reducing the error between the actual length of braid strand and numerically calculated value of the same for a given contracted length, the radius profile of deformed PAM is estimated. The obtained radius profile $f(z)$ at the outer surface is assumed to differ from the profile at the inner surface $g(z)$ by a constant thickness t . Then using incompressibility condition (the volume of bladder at rest and volume of bladder after deformation is same) the error between the initial and final volume is set to zero. This gave the final value of thickness of bladder and hence, the deformed shape of PAM. The estimate of thickness predicted from this approximation is compared with the models assuming fully cylindrical tips and is shown to have better conformation with results at higher contraction—where the end-effect is prominent.

2.2.6 Bladder as a thin walled tube

A few modeling attempts considering the bladder as a thin walled tube can also be found in the literature. In reference [116], the authors use large deformation theory on the deflation of a fiber-reinforced thin cylinder to determine the statics of PAM ([117], [118]). To reflect

the embedding of the nylon braiding cords, the stress resultant of thin cylinder is resolved as $\sigma_\alpha = \sigma_\alpha^1 + \sigma_\alpha^{11}$ where σ_α^1 is stress component due to deformation of bladder while σ_α^{11} is the stress component due to the braid strands. The solution procedure consists of guessing an initial value of the transverse stretch ratio λ_2 and iteratively adjusting the guess by comparing the value of initial length of tube obtained from formulation with the actual initial length. The closest choice of λ_2 will eventually predict the shape of outer surface of actuator and hence, the final deformed length. The main equations used are:

$$F_{\text{Liu}} = 2\pi E r_0 \left(\frac{2\sigma_2(0)}{\lambda_2(0)} - \frac{P_i E}{r_0} \right), \quad l_0 = - \int_{\lambda_2(0)}^1 \frac{d\lambda_2}{\lambda_1 \sin \gamma(\lambda_2)} \quad (2.28)$$

Where the axial stress $\sigma_2(0)$ and radial stretch ratio $\lambda_2(0)$ are at the initial configuration and $\gamma(\lambda_2)$ is the angle made by the meridian of PAM (on the surface) with the z axis given as a function of the stretch ratio. However, it may be noted that in most PAMs, the fiber is not embedded inside the bladder, but forms a sheath on the outer surface. Hence, the application of this model on a general PAM structure is debatable.

Another model by Ball et al. [119] also considers thin wall approach in modeling PAM. In this case, the expression for force is given as

$$F_{\text{Ball}} = F_{\text{strands}} + F_{\text{pressure}} + F_{\text{elastic}} \pm \mu_f P_{\text{eff}} \quad (2.29)$$

where, $F_{\text{strands}} + F_{\text{pressure}} = \frac{P_o l^2}{2\pi N^2} - P_i \left(\frac{b^2 - l^2}{4\pi N^2} - \frac{V_b}{l} \right), \quad P_o = P_i - \frac{\sigma_2(r_0 - r_i)}{\lambda_1 \lambda_2 \sqrt{\frac{b^2 - l^2}{n^2 \pi^2} - \frac{4}{\pi} \frac{V_b}{l}}}$

and $F_{\text{elastic}} = \frac{\sigma_1 V_b}{l}$

with P_o as the pressure acting at the outer radius by the bladder on the sleeve and $\sigma_{1,2}$ is given in terms of material constants and stretch ratios. In case of thick walled bladder as well as pre-strained bladders, the thin wall tube model is applied sequentially as if the thick cylinder is an array of concentric nested thin tubes. The computational method calculates the pressure P_o of the innermost layer and works sequentially outwards. The derivations based on thin film approach on the same lines of [116] may also be found in the fiber-reinforced electro-pneumatic PAM shown in [120].

2.2.7 Advanced modeling of PAMs

A few recently developed models try to capture the forces in PAM in greater detail. For example, in Chen et al. [121], two expressions for pressurization as well as de-pressurization of

a MPAM are derived. For pressurization, axial force is given as:

$$F_{\text{Chen}}^{(1)} = \frac{\pi P_i}{4} \left(\frac{b}{N\pi} \right)^2 (3 \cos^2 \theta - 1) - \frac{4m^2 N}{b \sin \theta} (M_f + M_d + M_r + M_{tr}) \quad (2.30)$$

For de-pressurization, the axial force is given as

$$F_{\text{Chen}}^{(2)} = \frac{\pi P_i}{4} \left(\frac{b}{N\pi} \right)^2 (3 \cos^2 \theta - 1) + \frac{4m^2 N}{b \sin \theta} (M_f - M_d - M_r + M_{tr}) \quad (2.31)$$

where detailed expression are given for moments, M_f , M_d , M_r and M_{tr} representing the effects of friction between strands of threads, bending deformation of thread strand, bulging of bladder between the threads in braided sleeve and the friction between threads and bladder, respectively. The highly detailed model requires numerical integration tools and the accuracy of the model may depend heavily on the coefficients of friction between the braid strands, between the braid and tube as well as the guess on the contact surface area between the strands.

Another example is the description of statics in [103], where the model considers the effect of thermal expansion in PAM during actuation. The improved model from [103] takes the form:

$$F_{\text{Andrikopoulos}}^{(2)} = \pi r_0^2 P_i k_f^{(2)} \left[q_1 (1 - k_\epsilon^{(2)} (\epsilon + \alpha_l \Delta T))^2 - q_2 \right] - \left(\frac{2\pi r_0 l_0 \mu_s}{S_{\text{scale}}^{(1)}} \right) \times \frac{\sin \theta_0}{(1 - k_\epsilon (\epsilon + \alpha_l \Delta T)) \sqrt{1 - \cos^2 \theta_0 (1 - k_\epsilon (\epsilon + \alpha_l \Delta T))^2}} \times P_i \text{sgn}(v) \quad (2.32)$$

where α_l , ΔT and v represent the coefficient of thermal expansion of bladder, the change in temperature as well as the velocity of MPAM tip, respectively.

Apart from the usual methods which focus on finding an exact analytical expression to relate pressure, force and displacement of a PAM, a few models use numerical methods such as finite element methods to solve the statics of PAM. For example in [122], the authors use FEA to analyze the dynamics of PAM used in parachute systems. The preliminary model used is:

$$\epsilon = 1 - \sqrt{\frac{F \tan^2 \theta_0}{2\pi r_0^2 P_i}} \quad (2.33)$$

where F is the applied force. The application of FEA can also be found in reference [123] as well as the analysis of a pneumatic bending fiber re-inforced actuator in reference [46]. Such analyses could be proven useful especially for actuators with non-uniform physical structure.

2.2.8 Modeling MPAMs

In case of modeling miniaturized PAMs, thin walled tube approximation is not appropriate since the ratio between bladder material volume and the inner volume of bladder is usually high. Also, it has been found that many models for normal sized PAM need to be adjusted by adding correction factors so as to include the effects of forces which are difficult to measure. Reference [38] shows the analysis of a miniaturized FAM with outer diameter 1.5 mm and length between 22 mm and 62 mm intended to use in a fluidic actuated surgical tool. The equation for the force used is

$$F_{\text{de Volder}} = \max \left[\left(F_{\min}, \frac{(P_i - P_{i,\text{corr}})b^2}{4\pi N^2} \right) \left(\frac{3(l - l_{\text{corr}})^2}{b} - 1 \right) \right] + \max [0, k_b (l - l_{b0})] \quad (2.34)$$

where l_{corr} , $P_{i,\text{corr}}$ are factors used to correct length and dead-band pressure, respectively. The term F_{\min} is used as a threshold so that the PAM does not generate pushing forces. Finally, the term $k_b (l - l_{b0})$ is added to generate a linear spring force equivalent in the model.

Another analysis and validation of statics of a MPAM with outer diameter between 3.02 mm and 4.19 mm is shown by Hocking et al. [115]. The basic force equation derived from Ferraresi shown below has the Hoop's stress (σ_1) and axial stress (σ_2) terms which consider the elasticity of material [104]. The force is obtained as

$$F = \frac{P_i}{4\pi N} (3l^2 - b^2) + \sigma_1 \frac{V_b}{l} - \frac{\sigma_2 t l^2}{2\pi N^2 r} \quad (2.35)$$

In Hocking's paper, these stresses are chosen as nonlinear (polynomial) functions of strain and the equation is modified to:

$$F_{\text{Hocking}}^{(1)} = \frac{P_i}{4\pi N} (3l^2 - b^2) + \frac{V_b}{l} \sum_{i=1}^n E_i \left(\frac{l}{l_0} - 1 \right)^i - \frac{t l^2}{2\pi N^2 r} \sum_{i=1}^n E_i \left(\frac{r}{r_0} - 1 \right)^i \quad (2.36)$$

where the material constants E_i are empirically identified from experimental results.

To the above model, friction is added as

$$F_{\text{Hocking}}^{(2)} = F_{\text{Hocking}}^{(1)} \pm \mu_f F_{\text{Hocking}}^{(1)} \text{sgn}(v) \quad (2.37)$$

One modification in the friction term compared to the other models is that, μ_f is assumed to vary with pressure. A dead-band pressure which is the threshold value of pressure upto

which contraction does not start is usually observed in the case of MPAMs. In this paper, correction to account for dead-band pressure is made as $P_i^{\text{corr}} = P_i - P_c$ where P_c is calculated from experiments. Similarly, the tip effect is considered by using a corrected length, $L^{\text{corr}} = l - 2 \left[\left(\frac{\pi}{2} - 1 \right) (r - r_0) \right]$ in the above equation. A similar strategy is used in reference [25] where the model used is essentially that of Hocking [115] with the thickness term included from Chou's model [98]. In this model, the stress is empirically related to strain as a function of pressure as

$$\sigma = \sum_{j=1}^n (E_{jI} + E_{jS} P_i) \epsilon^j \quad (2.38)$$

where the constants are experimentally determined.

In another paper by Sangian et al. [124], the authors characterizes miniaturized FAM of outer diameter 5.6 mm taking into account the pressure deadband. Gaylord's model is modified to include the threshold pressure (\bar{P}_i) required to initialize the contraction. The final force expression takes the form:

$$F_{\text{Sangian}} = \pi r_0^2 [q_1 (1 - \epsilon)^2 - q_2] \left[P_i - \bar{P}_i + \frac{E t_0 b}{2 \pi N r_0^2} \left\{ \left(1 - \frac{l^2}{l_0^2} \cos^2 \theta_0 \right)^{\frac{1}{2}} + \sin \theta_0 \right\} \right] \quad (2.39)$$

Use of empirical model formulation for MPAM (outer diameter 1.8 mm) can also be found in [45] where the static model used is

$$\epsilon_l = 1 - \sqrt{\frac{1}{\kappa_1} \left(\frac{F - \kappa_2}{P_i} - \kappa_3 \right)} \quad (2.40)$$

$$\epsilon_r = \sqrt{\frac{\kappa_4 \epsilon_l^2 + \kappa_5 \epsilon_l + \kappa_6}{\kappa_6 (1 - \epsilon_l)}} - 1 \quad (2.41)$$

2.2.9 Empirical considerations

As mentioned in section 2.1, advanced and more involved models are often quite difficult to implement in real-time control systems. Additionally, the measurement of exact values for parameters necessary for these advanced models will not be possible in all cases – it is hard to measure the deformed outer diameter of miniaturized muscles and axial strain of PAMs which are already employed in a robot. Hence, many models use empirical formulation derived from the basic models for practical purposes. In reference [24], the equation (2.6) is modified to

obtain

$$F_{\text{Takosoglu}} = 4\pi r_0^2 P_i [q_1 (1 - \epsilon)^n - q_2] \quad (2.42)$$

the factor n and also the parameter q_1 are later empirically determined to be:

$$n(P_i) = \kappa_1 e^{\frac{-P_i}{\kappa_2}} + \kappa_3, \quad q_1(P_i) = \kappa_4 e^{\frac{-P_i}{\kappa_5}} + \kappa_6$$

In a model in reference [100] the expression is further empirically adjusted to:

$$F_{\text{Itto}} = \pi r_0^2 P_i \left[q_1 \left\{ 1 - \kappa_1 (1 + e^{\kappa_2 P_i}) \epsilon \right\}^2 - q_2 \right] \quad (2.43)$$

and the above model so formed is shown to agree well with experimental values.

In reference [96], the authors analyse the static model of a PAM used as ‘pedestrian dummy device’ in the test set up of pedestrian safety system. The model derived takes the form:

$$F_{\text{Doric}} = F_{\text{Chou}} - F_{\text{PAM, e}} - F_{\text{PAM, s}} \quad (2.44)$$

where $F_{\text{PAM, e}} = \left(1 - \frac{w}{w_0} \right) \kappa_1$, $F_{\text{PAM, s}} = \frac{P\epsilon}{l_0} \kappa_2$

The second and third terms take into account the effects of thickness, elasticity of bladder as well as the form of PAM. The correction factors for elasticity as well as the shape of PAM, κ_1 and κ_2 are experimentally determined.

Purely empirical formulations are also presented in the works of [92], [125], [126], [127], [128] and [129] for its relative ease in control system design. In these papers, the empirical expressions for blocked force as a function of applied pressure and axial strain take different forms such as

$$F(P_i, \epsilon) = (\kappa_1 + \kappa_2 \epsilon + \kappa_3 \epsilon^2) P_i + (\kappa_4 + \kappa_5 \epsilon + \kappa_6 \epsilon^2 + \kappa_7 \epsilon^3 + \kappa_8 \epsilon^4) \quad (2.45)$$

$$F(P_i, \epsilon) = \kappa_1 + \kappa_2 \epsilon + \kappa_3 \epsilon^2 + \kappa_4 P_i + \kappa_5 \epsilon P_i \quad (2.46)$$

$$F(P_i, \epsilon, \dot{\epsilon}) = (\kappa_1 P_i^2 + \kappa_2 P_i + \kappa_3) \epsilon + \kappa_4 P_i + \kappa_5 + \kappa_6 \dot{\epsilon} \quad (2.47)$$

$$F(\epsilon) = \kappa_1 F_{\text{max}} \left(1 - \frac{\epsilon}{\epsilon_{\text{max}}} \right) \quad (2.48)$$

where constants κ are determined from prior experimentation.

2.2.10 Modeling hysteresis

In almost all the models described in the previous sections, hysteresis is accounted by adding or subtracting a frictional force term to the static equation for axial force. A convincing representation of the added frictional force term is not yet developed in the literature. In most cases, an approximating function is chosen to represent this frictional force term which is empirically determined. For example, in [90], this additional frictional force term F_{fstat} is calculated from the static force term F_{stat} obtained from phenomenological models as

$$F_{\text{fstat}} = -\mu_f F_{\text{stat}} = (\kappa_1 + \kappa_2 P_i) F_{\text{stat}} \quad (2.49)$$

While the term F_{stat} gives the mean curve of force-deformation plot, adding or subtracting this frictional force term will give the pressurizing and the de-pressurizing curve. In the above equation, the coefficient of friction is assumed to be linearly dependent on applied pressure and the constants k_1 and k_2 are determined from experiments.

In a few research works, a few empirical formulations are derived for force-displacement curves for expansion and compression of a PAM in a manner different from the method mentioned above. In cases where accurate hysteresis modeling is required— especially for practical applications, force-length and pressure-length hysteresis profiles of PAM are found out for compression and expansion curves separately. For example, in [130], van Damme et al. derived a hysteresis profile for pleated PAM using Preisach hysteresis model [131]. The math model takes the form

$$F_{\text{hyst}} = P_i l_0^2 f_{t_0}^{\text{fit}} (1 + \kappa_{\text{scale}} (W[\epsilon_s] - W_{(\epsilon_s)}^{\text{fit}})) \quad (2.50)$$

where $f_{t_0}^{\text{fit}} = \kappa_0 \epsilon^{-1} + \kappa_1 + \kappa_2 \epsilon + \kappa_3 \epsilon^2 + \kappa_4 \epsilon^3$ is the approximated mean curve of force-displacement hysteresis. The function $W[\epsilon_s]$ is the output of Preisach model which is a weighted summation of small discrete hysteresis relays and the function $W_{(\epsilon_s)}^{\text{fit}}$ represents a curve fitted between the two curves generated by $W[\epsilon_s]$ and κ_{scale} is a scaling factor. The proposed model is shown to estimate hysteresis phenomenon in PAM for contractile range below 20%.

A Maxwell slip model [132] for hysteresis is described in references [133], [134]. In this method, the force-length hysteresis of the PAM – the hysteresis component in PAM force curve due to the motion of PAM as well as the stretching of bladder – is experimentally determined and modeled. In order to achieve this, at first the force is measured from a constrained model where the motion of PAM is arrested. Then isobaric experiments are carried out where the pressure is kept constant and force value corresponding to change in length is obtained. The

difference between the two values gives the force-length hysteresis in PAM. This component of hysteresis appears to be qualified as ‘non-local memory hysteresis’ which can be modeled using Maxwell slip model. In non-local memory hysteresis modeling, when the PAM is actuated towards a particular contracted length (following a particular force-length curve) and is allowed to dilate (following a different curve), by ‘remembering’ the parameters of return points (F_m and ϵ_m), the subsequent contraction and dilation can be modeled by the knowing the characteristic curve called the ‘virgin curve’. In mathematical form, this procedure can be written as:

$$F_{\text{hys}} = F_m + 2f((\epsilon - \epsilon_m)/2); \quad f = y(\epsilon), v \geq 0, \quad f = -y(-\epsilon), v \leq 0 \quad (2.51)$$

where $y(\cdot)$ represents the virgin curve. In their papers, this virgin curve is identified as piecewise linear curve. For each piece of the curve, a slip element with stiffness ‘ k ’ and maximum saturation force ‘ w ’ can be attributed. The piecewise continuous stiff elements can also be visualized as a parallel arrangement of spring systems with each element having different values of stiffness and a saturation force limit (representing the pressure in pressure-length hysteresis plot) beyond which displacement does not take place for that particular element. From the knowledge of each slip elements, the hysteretic force can be calculated for any choice of length, by intuitively choosing the right number of elements that would contribute to the section of curve. The total hysteresis force, F_{hys} , is the sum $\sum_1^n F_i$.

In another paper by Jin et al. [135], the authors show a Bouc-Wen model [136] to represent the pressure-length hysteresis of PAM for use in control system design. In this work, the hysteresis loop for pressure-length curve is represented using the expression:

$$l(t) = k(k_1 P_i(t) - h(t)) + \rho \quad (2.52)$$

where $h(t)$ is a solution of the equation

$$\dot{h} = \alpha \dot{P}_i(t) - \gamma \dot{P}_i(t) |h|^n - \beta z |\dot{P}_i(t)| |h|^{n-1} \quad (2.53)$$

with the parameters $n, k, k_1, \rho, \alpha, \beta, \gamma$ identified by minimizing the least square error between the model and experimental data. The paper also presents a Prandtl-Ishlinskii (PI) [137] model for pressure-length hysteresis representation where the loop is given by the equations:

$$l(k) = \mathbf{w}^T \mathbf{H}_r[P_i, l_0](k) = \sum_{i=0}^{n-1} w_i \cdot \max \{P_i(k) - r_i, \min \{P_i(k) + r_i, l(k-1)\}\} \quad (2.54)$$

In the above \mathbf{H}_r are the backlash (play) operators of PI model and k is the sampling number of the operator. The weights w_i and threshold r_i are found out using least square error minimization as mentioned in the case of Boruc-Wen model. The application of Prandtl-Ishlinki model on trajectory control of PAM can be found in [138] (see also [139]).

The models suggested in [135], however are suitable mostly for symmetric hysteresis loops. In reference [140], a modification to this model which can be used in asymmetric hysteresis loop is proposed. Here, in the basic PI model, the backlash operator is divided into two, one for ascending and one for descending curves and is written as

$$l(t) = \kappa_1 P_i(t) + \sum_{i=1}^n w_i^a (\mathbf{H}_{r_i}^a[P_i, l_0](t) - P_i(t)) + \sum_{i=1}^n w_i^d (\mathbf{H}_{r_i}^d[P_i, l_0](t) - P_i(t)) \quad (2.55)$$

where $\mathbf{H}_{r_i}^{a,d}$ are different for ascending and descending; κ_1 is a constant. The two operators are subject to constraints:

$$\begin{aligned} \mathbf{H}_{r_i}^a[1, l_0](t) &= 1, \quad \mathbf{H}_{r_i}^a[1, l_0](k) = 1, \\ \kappa_1 + \sum_{i=1}^n w_i^a \mathbf{H}_{r_i}^a[1, l_0](t) + \sum_{i=1}^n w_i^d \mathbf{H}_{r_i}^d[1, l_0](t) &= 1 \end{aligned}$$

In the above equations, there are $(2n+3)$ parameters that need to be identified – the additional 3 parameters compared to the classic PI model are from determining coefficients of a quadratic function used in the descending play operator. Another variant in PI hysteresis model is shown in [141] where an ‘Extended Unparallel PI’ model is proposed. Here, the PI model is modified so that the ascending and descending edges are multiplied with factors α and β , which change the respective slopes. The final backlash operator becomes:

$$\mathbf{H}_{r_i, \alpha_i, \beta_i}[P_i](k) = \max \left\{ \alpha_i (P_i(k) - r_i), \min \left\{ \beta_i (P_i(k) + r_i), \mathbf{H}_{r_i, \alpha_i, \beta_i}[P_i](k-1) \right\} \right\} \quad (2.56)$$

2.3 Conclusions and summary of review

Tondu’s review paper [93] concludes with an open question of whether it is possible to achieve an accurate mathematical description of the physics behind the actuation of Pneumatic Artificial Muscles. Till date, many researchers have attempted to answer this question, which resulted in a variety of modeling techniques some of which, even though are not exact representation of the physical phenomena, seem to suit the purpose of application in PAM enabled robots and mechanisms. A detailed survey of various modeling considerations for PAM in this regard

have been carried out in this chapter and this is the first contribution of the thesis. Table 2.1 shows the summary of major phenomenological modelling strategies discussed above with the key equations used in the same. The models shown in rows marked with * are experimentally validated in literature, on miniaturized versions of PAMs or FAMs. From the first model mentioned in Gaylord's patent for fluidic muscle actuators, many improvements have been made so far, by adding correction factors, considering better modeling assumptions and including factors arising from other physical aspects of the PAM which are detailed. As shown in [142], where the authors picked static force component from [41] and the frictional forces from [99] for their model, it may be possible to combine only relevant component of forces as per the application. Since understanding the hysteresis of PAM in a phenomenological point of view is still a challenge, many applications rely heavily on empirical formulations. In this regard, a few empirical formulations are also discussed.

Though there are numerous models available in the literature for the statics of PAM, it is shown in the next chapter that the models do not conform to the experimental data for the fabricated MPAM due to the miniaturized size of the actuator. In order to address this shortcoming, a new approach to model the statics of MPAM is proposed and this is shown to be in good agreement with experimental results.

Author	Key equation(s)	Important considerations
Gaylord [22]	$F = \frac{b^2}{4\pi N^2} P_i (3 \cos^2 \theta - 1)$, eq. (2.3)	Kinematics of braid
Schulte [94]	$F = \frac{b^2}{4\pi N^2} P_i (3 \cos^2 \theta - 1) + \frac{bE}{N} \left[l_0 \sin \theta - \frac{\cos^2 \theta}{\sin \theta} \left(\frac{b}{N} \sin \theta - 2\pi r_0 \right) \right]$ $- \frac{l_0 b}{N} (P_i - P_u) (\mu_s + \mu_{st}) \sin \theta$, eq. (2.15)	Inclusion of material properties
Chou [98]	$F = \frac{b^2}{4\pi N^2} P_i (3 \cos^2 \theta - 1) + \pi P_i \left[\frac{bt_0}{N\pi} \left(2 \sin \theta - \frac{1}{\sin \theta} \right) - t_0^2 \right]$, eq. (2.5)	Thickness of bladder
Tondu [99]	$F = \pi r_0^2 P_i [q_1 (1 - k_\epsilon \epsilon)^2 - q_2] \pm \mu_s P_i \left[\frac{S_{\text{contact}}^{(1)}}{S_{\text{scale}}^{(1)}} \right]$, eq. (2.8)	End-effects and friction term
Ferraresi [104]	$F = \frac{P_i}{4\pi N} (3l^2 - b^2) + \sigma_1 \frac{V_b}{l} - \frac{\sigma_2 tl^2}{2\pi N^2 r}$, eq. (2.35)	Inclusion of Hoop and axial stress
Liu [116]	$F = 2\pi E r_0 \left(\frac{2\sigma_2(0)}{\lambda_2(0)} - \frac{P_i E}{r_0} \right)$, $l_0 = - \int_{\lambda_2(0)}^1 \frac{d\lambda_2}{\lambda_1 \sin \gamma(\lambda_2)}$, eq. (2.28)	Iterative procedure
Delson [106]	$F = P_i \frac{dV}{dl} + V_b \frac{dW}{dl}$, eq. (2.21)	Non-linear elastic material
Davis [101]	$F = \pi r_0^2 P_i [q_1 (1 - k_\epsilon \epsilon)^2 - q_2] \pm \mu_s P_i \left[\frac{S_{\text{contact}}^{(2)}}{S_{\text{scale}}^{(2)}} \right]$, eq. (2.12)	Improved friction term
Trivedi [111]	$F = \pi E (r_0^2 - r_i^2) (\lambda_1 - 1)$, eq. (2.25)	Neo-Hookean material model
Doumit [114]	$F = m \cos \beta \cos \theta \left[\left(\frac{P_i(r-t_0-2r_n)-\sigma_1 t_0}{mN \sin \theta} \right) l_{\text{cyl}} - \frac{P_i(r-2r_n-t_0)}{2mr \cos \theta} \frac{l}{N} \tan \theta \right]$ $+ \left(\frac{P_i(r+r_c-2t_0-2r_n) \cos \beta - 2\sigma_1 t_0}{mN \sin(\frac{\theta+\theta_c}{2})} \right) l_{\text{cone}} \Big] - P S_{\text{contact}}^{(2)} \mu_s$, eq. (2.27)	Improved end-effect term
de Volder* [38]	$F = \max \left[\left(F_{\min}, \frac{(P_i - P_{i,\text{corr}})b^2}{4\pi N^2} \right) \left(\frac{3(l-l_{\text{corr}})^2}{b} - 1 \right) \right] + \max [0, k_b (l - l_{b0})]$, eq.(2.34)	Model for MPAM
Hocking* [115]	$F = \frac{P_i}{4\pi N} (3l^2 - b^2) + \frac{V_b}{l} \sum_{i=1}^n E_i \left(\frac{l}{l_0} - 1 \right)^i - \frac{tl^2}{2\pi N^2 r} \sum_{i=1}^n E_i \left(\frac{r}{r_0} - 1 \right)^i$, eq. (2.36)	Polynomials for stress and strain
Chen [121]	$F = \frac{\pi P_i}{4} \left(\frac{b}{N\pi} \right)^2 (3 \cos^2 \theta - 1) \mp \frac{4m^2 N}{b \sin \theta} (M_f \pm M_d \pm M_r + M_{tr})$, eq. (2.30),(2.31)	Improved friction terms
Wang [113]	$F = F_z - P_i \pi r_i^2 - \frac{P_i r_i l^2 - F_\theta l^2}{2\pi N^2 r_0^2}$, eq. (2.26)	Using Mooney-Rivlin model
Robinson [90]	Same as Ferraresi, eq. (2.16)	Elliptical shape for end
Pillsbury* [25]	$\sigma = \sum_{j=1}^n (E_{jI} + E_{jS} P_i) \epsilon^j$, eq. (2.38)	Pressure dependent stress term
Sangian* [124]	$F = \pi r_0^2 [q_1 (1 - \epsilon^2) - q_2] \times$ $\left[P_i - P_{\text{th}} + \frac{Et_0 b}{2\pi N r_0^2} \left\{ \left(1 - \frac{l^2}{l_0^2} \cos^2 \theta_0 \right)^{\frac{1}{2}} + \sin \theta_0 \right\} \right]$, eq. (2.39)	Threshold pressure deadband
Andrikopoulos [103]	$F = r_0^2 P_i k_f^{(2)} \left[q_1 \left(1 - k_\epsilon^{(2)} (\epsilon + \alpha_l \Delta T) \right)^2 - q_2 \right]$ $- \left(\frac{P_i \text{sgn}(v)}{S_{\text{scale}}^{(1)}} \right) \frac{2\pi r_0 l_0 \mu_s \sin \theta_0}{(1 - k_\epsilon (\epsilon + \alpha_l \Delta T)) \sqrt{1 - \cos^2 \theta_0 (1 - k_\epsilon (\epsilon + \alpha_l \Delta T))^2}}$, eq. (2.32)	Temperature effects on PAM
Ball* [119]	$F = F_{\text{strands}} + F_{\text{pressure}} + F_{\text{elastic}} \pm \mu_f P_{\text{eff}}$, eq. (2.29)	Concentric thin walled tubes

Table 2.1: Summary of phenomenological models of PAM

Chapter 3

Fabrication and characterization of miniaturized PAMs

3.1 Introduction

From the literature as well as from the experiments conducted on a MPAM, it is noted that static characteristics of miniaturized PAMs are not always consistent with the models used for normal sized PAMs. This is primarily due to the larger ratio between the volume occupied by bladder and the internal volume of the bladder as well as the end effects. Hence, most of the models for MPAMs require prior experimentation to accurately determine the correction factors, friction coefficients as well as the empirical constants used in the stress equations. Also, simpler models such as the one proposed by Sangian et al. [124] is quite inaccurate in predicting the pressure-deformation characteristics of MPAM (as shown in the later section of this chapter), while the numerical iterative method used by Ball et al. [119] is computationally expensive and non-trivial to implement. Moreover, it is also observed that many models proposed in the literature are inconsistent to the changes in initial parameters when applied on MPAMs. For measurements taken from specimens belonging to same fabricated lot, the accuracy of theoretical models vary considerably when only the initial length or braid angle is different, while keeping all the other material and fabrication parameters constant. This anomaly and the gap in literature necessitates the development of an improved statics model for MPAM.

In this chapter, a new approach to model the statics of MPAM is proposed, which is shown to be consistent with variation in MPAM parameters and in good agreement with experiments done on MPAMs. A miniaturized PAM with diameter less than 2 mm is fabricated and is characterized. The fabrication procedure as well as the experimental set-up is discussed in section 3.2. The derivations of proposed model is explained in detail in section 3.3 followed by



Figure 3.1: Fabricated miniaturized pneumatic artificial muscles–1.5 and 1.2 mm diameter

experimental validation of the proposed model in section 3.4. Finally, conclusions are presented in section 3.5.

3.2 MPAM characteristics and experimental set-up

Before the model is discussed in detail, characteristics of the MPAMs fabricated as well as the set-up used for experimentation is discussed. Two MPAMs are used in this study, consisting of inner silicone tubes with outer radii $r_o = \{0.55, 0.75\}$ mm and inner radii $r_i = \{0.25, 0.25\}$ mm respectively. The tubes are braided on the outer surface using nylon cords of radius $\sim 50\mu\text{m}$ at angles $\alpha = \{36^\circ, 38^\circ, 40^\circ\}$ (refer Fig. 3.1) from the meridian of tube. Since the angle of winding is less than 54.7° , the actuator contracts upon application of pressure [98]. The overall outer diameter of MPAM is 1.2 mm and 1.6 mm. Braiding is carried out using a standard Horn gear braiding machine used in the fabrication of coaxial communication cables. Most commercially available braiding machines are designed for braiding the tubes up to a minimum of 5 mm. However, by manually adjusting the configuration of machine, it was possible to braid the silicone tube so that the gap between silicone tube and braid is minimized. In spite of the care taken during fabrication, in the MPAMs used for experiments, there exist a small gap δ between the outer radius of the silicone tube r_o and the inner surface of braid with the radius r_b . The fabrication process also limits the range of helix angles with which the nylon fibers could be braided – in the fabricated MPAMs helix angles between 36° and 40° could be obtained. One end of the braided tube is sealed with epoxy adhesive which forms the free end of the MPAM. In the other end, a micro-pipette is inserted and fixed using a gelatinous adhesive. The free end of the pipette is connected to a polyurethane tube which is used to supply pressurized air. The ends of pipette are then secured using epoxy adhesive. The actual fabricated MPAMs are shown in Fig. 3.1. The contraction of 60 mm long MPAM after pressurization is demonstrated in Fig. 3.2.



Figure 3.2: MPAM before and after pressurization

The layout of pneumatic circuit used to actuate MPAM is shown in Fig. 3.3. A pneumatic compressor of maximum output pressure 1034 kPa (150 psi) is connected to a 1 liter air (at NTP) reservoir which is used to deliver high pressure air to the MPAM. A pressure regulating circuit operates the compressor when the value of pressure in reservoir falls below certain threshold thereby maintaining availability of 827 kPa (120 psi) pressure at all times. Two proportional valves are used to control pressure inside air muscle – one for pressurizing the MPAM and the other for bleeding. A Honeywell pressure transducer (with range of 0 to 1034 kPa) is connected in series with MPAM to measure the inner pressure. An ATmel ATmega2560 micro-controller board interfaced with MATLAB [143] controls the proportional valves through a current driver circuit to maintain user defined value of pressure inside the MPAM. To keep a straight alignment of the MPAM, a 5 gram weight (0.05 N) is applied on the free end. For a 40 mm air muscle, the maximum deformation of 15 gram (0.15 N) end-loading varies from 5 gram by less than 0.3 mm (less than 3% of total deformation). Since this variation in deformation is comparable to the error bounds of the measurements in the experiments, the effect of this small end-loading is ignored in the formulations. The experimental set up used is shown in Fig. 3.4¹.

The deformation of MPAM is captured using a high resolution camera and changes in length are computed using image processing. The measurement method consists of taking photos of MPAMs in its operational state using high resolution camera and identifying the length of MPAM by measuring the displacement between the image pixels corresponding to the tips of MPAM. At first, size of each pixel in the HD camera image is calculated based on

¹In the actual experiments, the MPAM is positioned vertically with a weight of 5 grams hanging on the free end. The horizontal position shown in figure is for better visualization.

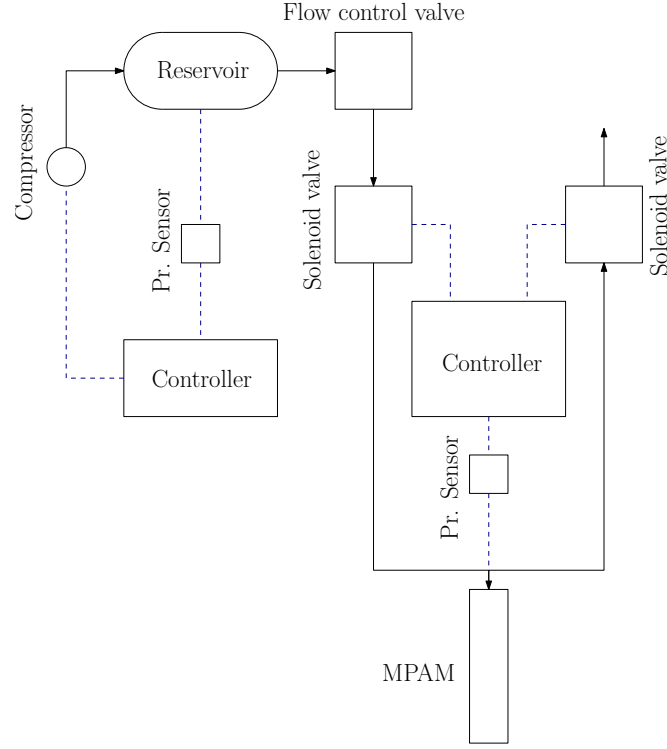


Figure 3.3: Layout of pneumatic circuit and controller

a benchmarking with a standard object with known dimensions. Then the distance between two markers set in the either ends of MPAM is calculated in terms of pixels and using the scale mentioned above, it is converted in terms of millimetres. The possible error in this method is in identifying the marker pixels which is not more than 2 pixels size in each ends. For the scale and measurement set up used, this value is about 0.2 mm. By conducting the scale determination as well as the MPAM operation in the same focal plane of camera, perspective issues in measurement are also avoided. All measurements are repeated more than 5 times and the results are reported as mean of the obtained vales and measurement errors shown in error bars.

Fig. 3.5 shows the end-point displacement of MPAM during inflation as well as deflation with dead load ($F = 0.05N$) attached at the end. The MPAM clearly shows hysteresis. The maximum error due to measurement is about 0.1 mm and error bars in the plot are obtained from at least 5 sets of experiments. In the comparisons with existing approaches, the hysteresis is not shown and the mean value, between the inflation and deflation, is used (see Fig. 3.5). Experiments were performed with different lengths of MPAMs and results are compared with theoretical values obtained from various models available in literature. Since the focus is on identifying the mechanics of MPAM, the comparison plots are limited to only phenomenological



Figure 3.4: Experimental set-up for MPAM characterization

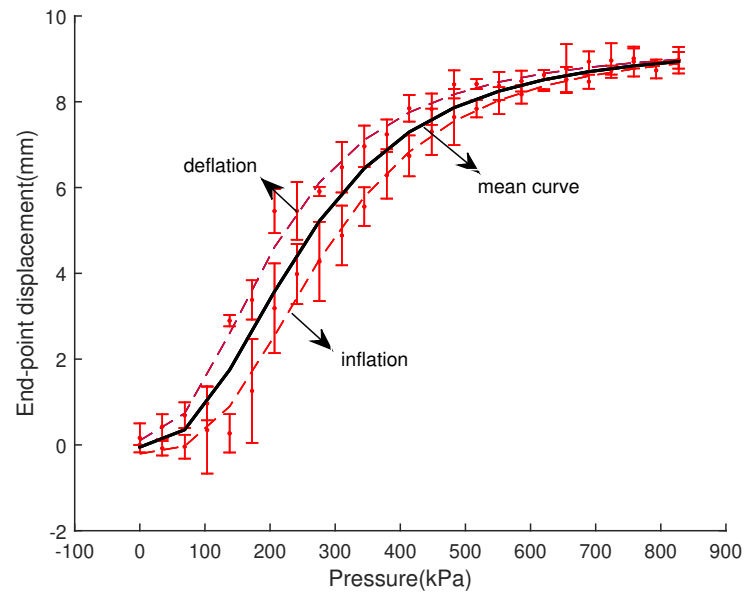


Figure 3.5: MPAM hysteresis profile

models as opposed to the models which rely on empirical data as well as parameters which require sophisticated measurement set-up for identification.

3.3 Proposed statics model for MPAM

This section details the new approach for modelling statics of MPAM.

3.3.1 Characterization of pressure dead-band

In Fig. 3.6, we can see the pressure deadband which is the range of pressure below which contraction of MPAM is not apparent. This pressure deadband is mentioned in [115] as due to the Mullin's effect [144], which is unlikely in the case of MPAM used in this work. In our case, the MPAM was pre-stretched and inflated multiple times, so as to form a permanent set before it is braided on the outer surface. This ensured the repeatability of bladder inflation characteristics while employed in the MPAM. It is also observed that the un-braided bladder inflates considerably at values of pressure within this dead-band range. On closer observation, it is found that the MPAM expands instead of contracting in this range (see inset of Fig. 3.6) and this is due to the small gap δ (of the order of 0.04 mm) between the tube and nylon sleeve during fabrication, as mentioned in earlier section. It may be noted that this expansion is not usually seen in commercial PAMs as well as fiber embedded PAMs where this gap is unlikely to occur while it was prominent in the fabricated braided sleeve PAMs as in the case of the MPAM used in this work and in the work presented in [115]. Due to this gap, the initial stage of pressurization results in the expansion of silicone tube till the outer surface of silicone tube makes contact with the nylon sleeve. The pressure at which contact occurs is termed the critical dead-band pressure \bar{P}_i . Since the forces acting on MPAM before and after the critical deadband pressure are different, we may consider this as two phases of contraction which has to be treated separately. The bladder material is assumed as linear elastic for simplicity in derivations and also since the linear elastic model is shown to be sufficient to capture model characteristics as observed from Kothera's model [105].

3.3.2 Model for first phase—expansion

In the first phase of deformation, the bladder expands without the constraint of the outer braid sheath. In this phase, a linear thick cylinder approach is used to find the displacements in axial and radial directions. The equilibrium equations for inflation of thick cylinder are given by [145]

$$\frac{\partial}{\partial r} \left(\frac{1}{r} \frac{\partial(r u_r)}{\partial r} \right) = 0, \quad \frac{\partial^2 u_z}{\partial z^2} = 0 \quad (3.1)$$

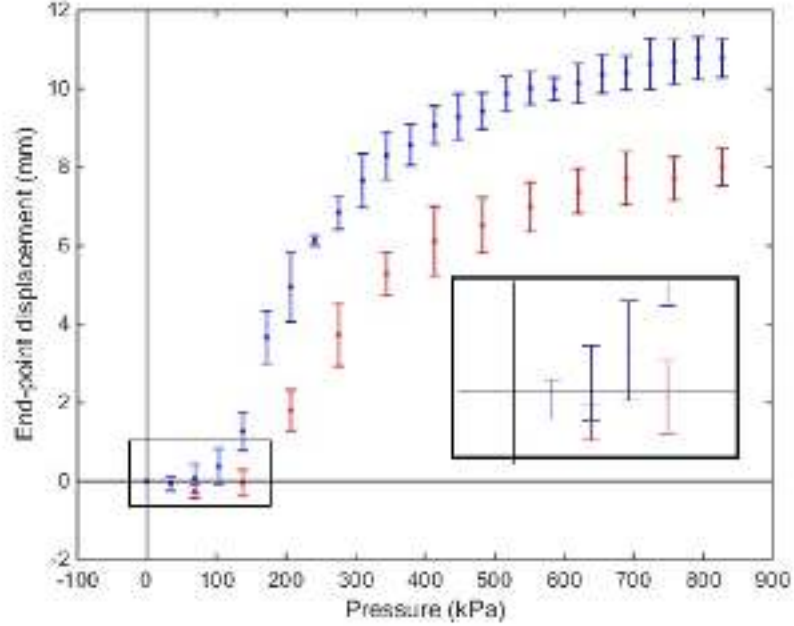


Figure 3.6: Deformation phases of MPAM (inset – elongation part zoomed)

where u_r and u_z are the displacements of silicone tube in radial and axial directions respectively¹. Solving the equations, we get the displacements

$$u_r = c_1 r + \frac{c_2}{r}, \quad u_z = c_3 z + c_4 \quad (3.2)$$

where c_i , $i = 1, 2, 3, 4$ are constants. In the initial phase of deformation, since the braid has not come in contact with the tube, the outer surface will be pressure free. The applied pressure P_i will act in the inner cylindrical surface while in the axial ends, inflation pressure as well as the pressure due to applied axial load will act. This pressure component will be $P_s = P_i \frac{r_i^2}{r_o^2 - r_i^2} + P_{\text{sil}}$, where P_{sil} is the pressure acting on the silicone tube due to the applied axial load F . Using these boundary conditions as well as the zero displacement condition on the fixed end of the MPAM, we get the values of constants as:

$$\begin{aligned} c_1 &= \frac{(\Lambda_1 + 2\Lambda_2)}{2\Lambda_2(3\Lambda_1 + 2\Lambda_2)} \left[\frac{P_i r_i^2}{r_o^2 - r_i^2} + \frac{P_o r_o^2}{r_o^2 - r_i^2} - \frac{P_s \Lambda_1}{\Lambda_1 + 2\Lambda_2} \right] \\ c_2 &= \frac{1}{2\Lambda_2} \left[\frac{r_i^2 r_o^2}{r_o^2 - r_i^2} \right] (P_i - P_o) \end{aligned}$$

¹The variable r in this section would represent the radial co-ordinate in the cylindrical co-ordinate system as opposed to the deformed outer radius of tube in chapter 2.

$$\begin{aligned} c_3 &= \frac{\Lambda_1}{\Lambda_2 (3\Lambda_1 + 2\Lambda_2)} \left[-\frac{P_i r_i^2}{r_o^2 - r_i^2} + \frac{P_o r_o^2}{r_o^2 - r_i^2} + P_s \frac{\Lambda_1 + \Lambda_2}{\Lambda_1} \right] \\ c_4 &= 0 \end{aligned} \quad (3.3)$$

where Λ_1 and Λ_2 are Lamé's parameters. Substituting the constants, we get the displacements as:

$$u_r|_{r=r_o} = \frac{r_o}{\Lambda_2 (3\Lambda_1 + 2\Lambda_2)} \left[\frac{2(\Lambda_1 + \Lambda_2) r_i^2}{(r_o^2 - r_i^2)} P_i - \frac{\lambda}{2} \left(P_i \frac{r_i^2}{r_o^2 - r_i^2} + P_{\text{sil}} \right) \right] \quad (3.4)$$

$$u_z|_{l=l_0} = \frac{\Lambda_1 l_0}{\Lambda_2 (3\Lambda_1 + 2\Lambda_2)} \left[-\frac{P_i r_i^2}{r_o^2 - r_i^2} + \left(P_i \frac{r_i^2}{r_o^2 - r_i^2} + P_{\text{sil}} \right) \frac{\Lambda_1 + \Lambda_2}{\Lambda_1} \right] \quad (3.5)$$

The MPAM expands according to the above equations till the tube makes contact with the braid. The pressure components at this point remains the same as that of the initial expansion phase, since there is no radial pressure on the outside surface of the silicone tube at the onset of contact. As the tube expands, the braid deforms as per the kinematics rule given in equations (2.1) and (2.2). Taking into account the gap between braid and the tube, the modified kinematics model of the braided sleeve can be written as:

$$l_0 = b \cos \theta_0, \quad 2\pi r_b N = b \sin \theta_0 \quad (3.6)$$

$$l_0 + \hat{u}_z = b \cos \theta, \quad 2\pi (r_b + \hat{u}_r) N = b \sin \theta \quad (3.7)$$

where $r_b = r_0 + \delta$ is the initial radius of the braided sleeve and the quantities \hat{u}_r and \hat{u}_z represent the radial as well as the axial displacements of the braided sleeve. The above equations can also be written as a single expression which relates the radial and axial displacements of the sleeve:

$$\hat{u}_r = r_b \left\{ \frac{1}{\sin \theta_0} \sqrt{1 - \cos^2 \theta_0 \left(1 + \frac{\hat{u}_z}{l_0} \right)^2} - 1 \right\} \quad (3.8)$$

Since the braid and sleeve are sealed at the tips, the axial displacement of the sleeve and the tube is the same. Hence, $\hat{u}_z = u_z|_{l=l_0}$ at all times. At the critical inflection pressure, the tube makes contact with the braid surface. This is the point where the radius of deformed bladder becomes equal to the radius of the displaced sleeve. Hence,

$$r_o + u_r|_{r_o} = r_b + \hat{u}_r = r_o + \delta + \hat{u}_r \quad (3.9)$$

and we have

$$r_o + c_1 r_o + \frac{c_2}{r_o} = r_o + \delta + r_b \left\{ \frac{1}{\sin \theta_0} \sqrt{1 - \cos^2 \theta_0 \left(1 + \frac{\hat{u}_z}{l_0} \right)^2} - 1 \right\} \quad (3.10)$$

Simplifying and substituting for \hat{u}_z , we get

$$c_1 r_o + \frac{c_2}{r_o} = \delta + r_b \left\{ \frac{1}{\sin \theta_0} \sqrt{1 - \cos^2 \theta_0 (1 + c_3)^2} - 1 \right\} \quad (3.11)$$

In the above expression, the constants c_1 , c_2 and c_3 depend only on applied P_i which is the inflection pressure \bar{P}_i . Substituting the values of constants, we get the following equation

$$\begin{aligned} r_b \left\{ \frac{1}{\sin \theta_0} \sqrt{1 - \cos^2 \theta_0 \left(1 + \frac{\Lambda_1}{\Lambda_2 (3\Lambda_1 + 2\Lambda_2)} \left[-\frac{\bar{P}_i^2}{r_o^2 - r_i^2} + P_s \frac{\Lambda_1 + \Lambda_2}{\Lambda_1} \right] \right)^2} - 1 \right\} \\ - \frac{r_o}{\Lambda_2 (3\Lambda_1 + 2\Lambda_2)} \left[\frac{2(\Lambda_1 + \Lambda_2) r_i^2 \bar{P}_i}{(r_o^2 - r_i^2)} - \frac{\Lambda_1}{2} P_s \right] + \delta = 0 \end{aligned} \quad (3.12)$$

where $P_s = \bar{P}_i \frac{r_i^2}{r_o^2 - r_i^2} + \frac{F}{\pi r_i^2}$. This equation can be numerically solved to find the inflection pressure. For values of applied pressure below \bar{P}_i , equation (3.5) can be used to find the end-point elongation of the MPAM.

3.3.3 Model for second phase-contraction

For values of pressure above \bar{P}_i , the contact is established and in this phase, the radial as well as axial displacement of braided sheath will be same as that of the outer surface of silicone tube i.e., $u_r|_{r_o} = \hat{u}_r$ and $u_z|_{l_o} = \hat{u}_z$. Then from the kinematics of braid, equation (3.7), and from equation (3.2) we can write

$$c_1 + \frac{c_2}{r_o^2} = \left(\frac{\sin \theta}{\sin \theta_0} - 1 \right), \quad c_3 = \left(\frac{\cos \theta}{\cos \theta_0} - 1 \right) \quad (3.13)$$

The above equations represent the constrain on the motion of silicone tube imposed by the braided sleeve.

In this phase, an axial pull on sleeve generates a radial pressure on the outer surface of the silicone tube and vice versa. The total axial end force on the MPAM, F_e , has contributions from three components which are 1) the manually applied axial load F , 2) force acting on the walls due to the applied inner pressure $F_{P_i} = P_i (\pi r_i^2)$ and 3) any other unaccounted forces such as the static frictional force between the threads and the axial component of force due to the

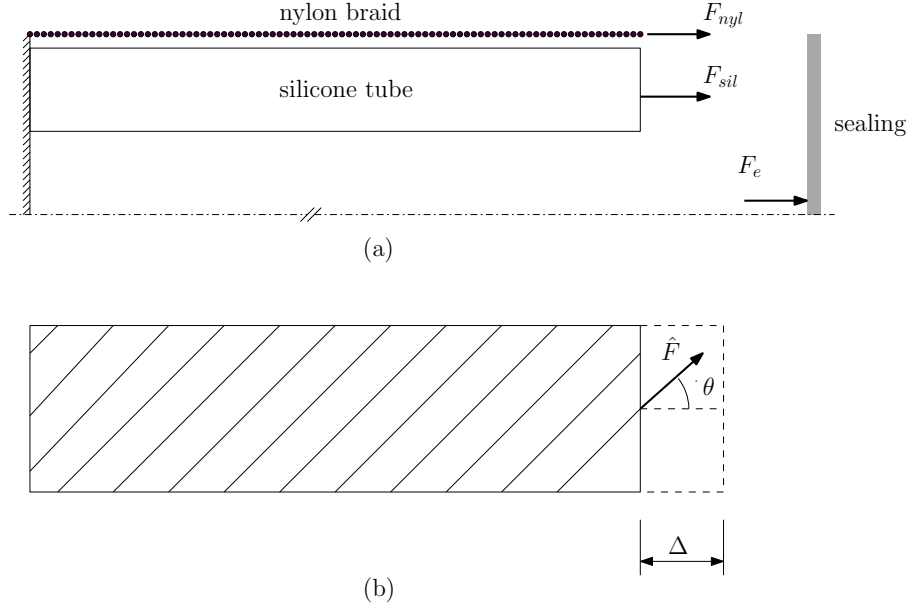


Figure 3.7: MPAM statics

conical shape at the ends which are essential to maintain the static equilibrium of the MPAM. These unaccounted force components are collectively termed F_u . This total axial force F_e is borne unequally by the axial end of silicone tube as well as the nylon braid (ref Fig. 3.7).

$$F_e = F + F_{P_i} + F_u = F_{sil} + F_{nyl} \quad (3.14)$$

where F_{sil} represents the axial force acting on silicone tube and F_{nyl} represents the axial force acting on the nylon braid. The force component acting on the braided sleeve is then converted into a radial force based on the kinematics of the braid. The pressure generated by this radial force will constitute the component P_o in the equations (3.3). Derivation of this radial pressure is detailed in what follows.

Since the displacement of end of MPAM Δ is same as the deformation of the nylon sleeve Δ_{nyl} as well as the silicone tube Δ_{sil} , it is possible to write the individual components of forces in terms of the end force F_e . The material properties of the tube and sheath can be used to calculate the axial displacement of nylon sheath,

$$\Delta_{nyl} = \frac{\hat{F}b}{\hat{A}_{nyl}E_{nyl}} \cos \theta_0 = \frac{F_{nyl}l_0 \cos \theta_0}{m\hat{A}_{nyl}E_{nyl}} \quad (3.15)$$

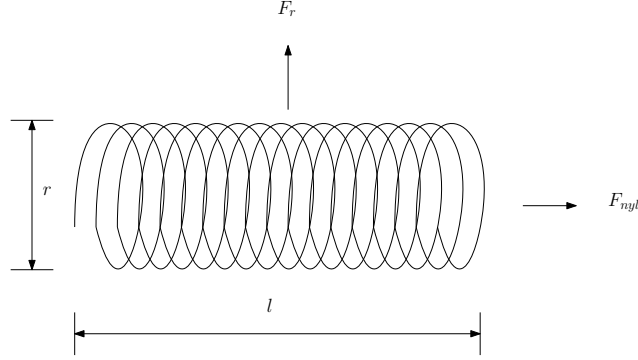


Figure 3.8: Braid statics

where $\hat{F} = \frac{F_{nyl}}{m} \cos \theta_0$ is the force acting on a single strand of braid and \hat{A}_{nyl} is the area of cross section of single nylon strand and E_{nyl} is the modulus of elasticity of nylon (refer Fig. 3.7). Similarly, the axial displacement of silicone tube can be written as

$$\Delta_{sil} = \frac{F_{sil} l_0}{A_{sil} E_{sil}} \quad (3.16)$$

where A_{sil} and E_{sil} are the cross section area and Young's modulus of silicone tube. From equations (3.14), (3.15) and (3.16), we get the individual components of forces in terms of end force acting on MPAM as:

$$F_{nyl} = \frac{F_e m \hat{A}_{nyl} E_{nyl}}{m \hat{A}_{nyl} E_{nyl} + \cos \theta_0 A_{sil} E_{sil}} \quad (3.17)$$

and

$$F_{sil} = \frac{F_e \cos \theta_0 A_{sil} E_{sil}}{m \hat{A}_{nyl} E_{nyl} + \cos \theta_0 A_{sil} E_{sil}} \quad (3.18)$$

The radial force applied by the braid on the outer surface of tube due to the axial pulling force F_{nyl} to maintain static equilibrium of the sheath can be calculated using virtual work principle. From Fig. 3.8, we get

$$F_r \delta r + F_{nyl} \delta l = 0 \quad (3.19)$$

where δr and δl are the virtual displacements in radial and axial directions, respectively. This quantity can be obtained by taking the variational derivatives of equations (3.7)

$$\delta l = -b \sin \theta \delta \theta, \quad \delta r = b \frac{r_b \cos \theta}{l_0 \tan \theta_0} \delta \theta \quad (3.20)$$

where $l = l_0 + \hat{u}_z$, $r = r_b + \hat{u}_r$ are the length and radius of sleeve at angle θ . Substituting in equation (3.19) and rearranging, we get

$$F_r = F_{\text{nyl}} \frac{l_0}{r_b} \tan \theta \tan \theta_0 \quad (3.21)$$

The pressure acting on the surface of tube due to this radial force can be calculated by dividing the radial force with the surface area of contact S_{contact} between the tube and nylon sheath. The value of S_{contact} is difficult to measure due to the small size of the MPAM. However, we assume that the contact area between the braid and sheath is same as the area of contact between braid in the cross-over points as shown in Fig. 3.9. An analytical expression for the same is given by Davis (mentioned in chapter 1). Rearranging the expressions (2.9) and (2.10), we get

$$S_{\text{contact}} = \left(\frac{\sin^2 \theta_{\min} \cos^2 \theta_{\min}}{\sin^2 \theta \cos^2 \theta} \right) S^{\text{cyl}}$$

where S^{cyl} represents the outer surface area of the silicone tube after deforming to the angle θ . The quantity in brackets represents the fraction of total outer surface area of silicone tube where the contact occurs. However, in the either ends of MPAM, the braid stretches, so as to assume the shape of a conical frustum as pointed out in [93] (refer section 2.2). In this region, the braid densely covers the surface of tube due to the stretching effect (ref Fig. 3.10). Due to this reason, we may assume full contact at these ends which are about a length $\phi = 5$ mm from either ends. Since this end-effect accounts for approximately 25% of the total length of MPAM, this effect needs to be included in the formulation. Then the cylindrical portion of the MPAM will only be $(l_0 - 2\phi)$ mm long. Taking into account the end-effect factor, we can write the total area of contact as:

$$S_{\text{contact}} = \frac{\sin^2 \theta_{\min} \cos^2 \theta_{\min}}{\sin^2 \theta \cos^2 \theta} [2\pi r (l_0 - 2\phi) (1 + c_3)] + 2\pi (r_b + r) \phi (1 + c_3) \quad (3.22)$$

The pressure P_o acting on the surface of the silicone tube will be due to the braided sleeve, $P_o = P_b = \frac{F_r}{S_{\text{contact}}}$. Substituting the values from equations (3.17), (3.21) and (3.22), we get the

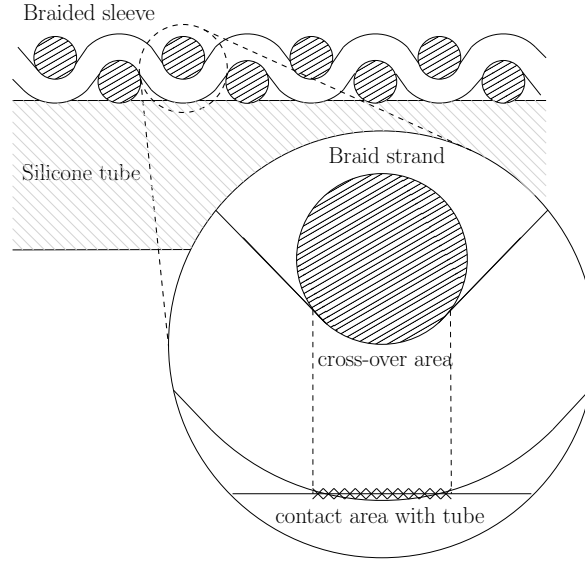


Figure 3.9: Area of contact between silicone tube and braided sleeve

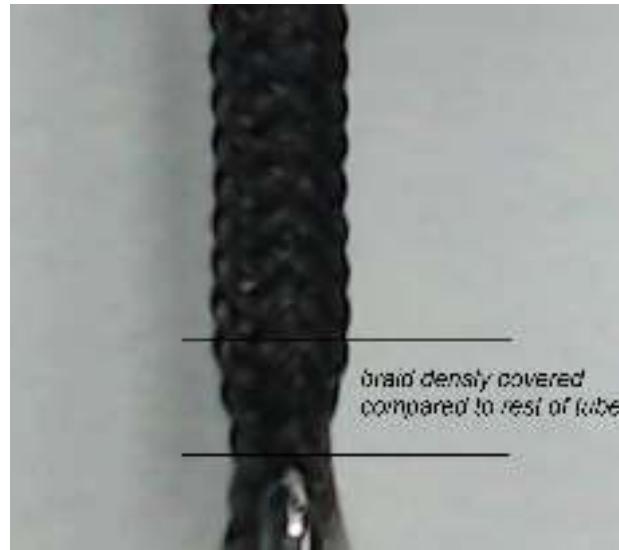


Figure 3.10: End-effect due to braiding

braid pressure

$$P_o = \frac{\left[\frac{2(F + \pi r_i^2 P_i + F_u) m \hat{A}_{ny1} E_{ny1}}{2m \hat{A}_{ny1} E_{ny1} + 3 \cos \theta_0 A_{sil} E_{sil}} \right] \frac{l_0 \sin^2 \theta \sin \theta_0}{r_b \cos \theta \cos \theta_0}}{\left[\left\{ \frac{\sin^2 \theta_{\min} \cos^2 \theta_{\min}}{\sin^2 \theta \cos^2 \theta} \left[2\pi \left(c_1 r_o + \frac{c_2}{r_o} \right) (l_0 - 2\phi) (1 + c_3) \right] \right\} + 2\pi \left(r_b + c_1 r_o + \frac{c_2}{r_o} \right) (\phi + c_3 \phi) \right]} \quad (3.23)$$

The six equations in (3.3) and (3.13) along with the outer pressure value given by equa-

tion (3.23) can be solved for the six unknown quantities $c_1, c_2, c_3, c_4, \theta$ and F_u . Then the final displacements in this contraction phase can be found using the expressions:

$$u_r|_{r=r_o} = c_1 r_o + \frac{c_2}{r_o} \quad (3.24)$$

$$u_z|_{l=l_o} = c_3 l_o \quad (3.25)$$

For ease of implementation and to simplify the calculations in second phase, it is possible to consider the second phase as a problem of deformation with the dimensions of tube and sleeve reset to the values at the inflection point [115]

$$r_o \rightarrow r_o + \hat{u}|_{r_o} \quad r_i \rightarrow r_i + \hat{u}|_{r_i} \quad l_o \rightarrow l_o + \hat{u}|_{l_o}$$

where $(\bar{\cdot})$ denote the corresponding values at the inflection point. For the new arrangement to be in equilibrium, all the traction forces on surfaces must be zero. Hence, we also modify the input pressure to $P_i \rightarrow P_i - \bar{P}_i$, pressure at the axial end to $P_s \rightarrow P_s - \bar{P}_s$ and the radial outer surface pressure on silicone tube (equal to the pressure applied by braid) to $P_o = P_b \rightarrow P_b - \bar{P}_b$.

3.3.4 Summary of proposed model

To summarize, the model proposed above constitutes two phases of deformation—an initial elongation phase followed by the contraction phase. In the first phase, the statics of PAM is essentially the statics of the inner tube which is expressed as an inflation problem of a linear thick cylinder. In the second phase, the braided sleeve constraints the tube motion by adding radial pressure on the outer surface of tube. Expression for this radial pressure is formulated based on the kinematics of braid as well as an estimate of the contact surface area between the sleeve and the tube. By applying the derived surface pressure on the tube, the static equations of inner tube is solved along with the kinematic constraint equations, to form the contraction model. One major advantage of using the developed model is that all the axial forces required to maintain the static equilibrium of MPAM—given the values of other applied forces and known components of forces – are collectively termed as F_u and is solved from the six set of equations. Hence finding exact mathematical descriptions of the individual components acting in this direction such as static frictional force, axial force component from the conical ends and other non-linearities are not necessary. If one wishes to study the dependencies of individual axial components of force, one needs to break down F_u into its individual components such as $F_u = F_{\text{static}} + F_{\text{conical}}$ for example. However, in doing so, it is highly likely that many other contributing factors may be overlooked for the axial load which would result in an incomplete

formulation. Another advantage of the model is that except the length of the conical section of muscle after deformation which needs to be measured, all other parameters can be obtained during fabrication itself.

3.4 Experimental validation of proposed model

The above derived equations for deformation of MPAM is solved using `fsolve` routine in MATLAB on an desktop PC with 2.0 GHz processor. The routine takes approximately 0.04 seconds to converge with zero initial conditions. Results from the experiments on 40 mm MPAM are plotted against the theoretical values alongside other models for comparison in Fig. 3.11. We can see that the derived model predicts the end-point displacement better than the other compared models with standard error of 4.6% from the maximum deflection. The error values for other models considering the parameters which are obtained from the best curve fit, are 40%, 12%, 7%, 8%, 29%, 8% and 35% for Chou [98], Liu [116], Kothera [105], Andrikopoulos [103], Trivedi [111], Hocking [115] and Sangian's [124] models respectively. The length of conical end section is measured experimentally for this calculation while all the other data are obtained from fabrication. By keeping all the parameters constant, the results for 60 mm MPAM is plotted in Fig. 3.12. Except for the Hocking's model (error = 13%), the other models are quite inconsistent in predicting the theoretical contraction with standard error above 20%. The derived model is found to be better, with values predicted within 2% error. In order to check the consistency of winding angle, the theoretical results for three different winding angles of MPAM are plotted and are compared with the experimental values (refer Fig. 3.13). The MPAM wound at higher braid angle was found to have larger gap due to the limitation in winding process. However, the experimental results match the theoretical values with less than 5% error. Theoretical and experimental results for MPAMs of three different lengths wound at 38° initial winding angle are shown in Fig. 3.14. The standard errors between theoretical and experimental values are less than 5%. In order to check the consistency of change in thickness, experiments are conducted on MPAMs fabricated with silicone tube of 1.5 mm outer diameter and 0.5 mm thickness. The results are shown in Fig. 3.15 with error values at a maximum of 6.9%.

The stiffness of a 45 mm MPAM compressed at 785 kPa pressure is calculated by plotting axial force vs displacement and calculating the slope (ref Fig. 3.16). The value is found to be 0.94 N/mm. This value over-predicts the actual deflection of 0.63 N/mm by 49%. Except Andrikopoulos' model¹ which gives 0.92 N/mm and Liu's model which gives 1.96 N/m stiffness,

¹Since the factor $k_f^{(2)}$ in Andrikopoulos' model is evaluated using experimental data, the better prediction of stiffness is expected.

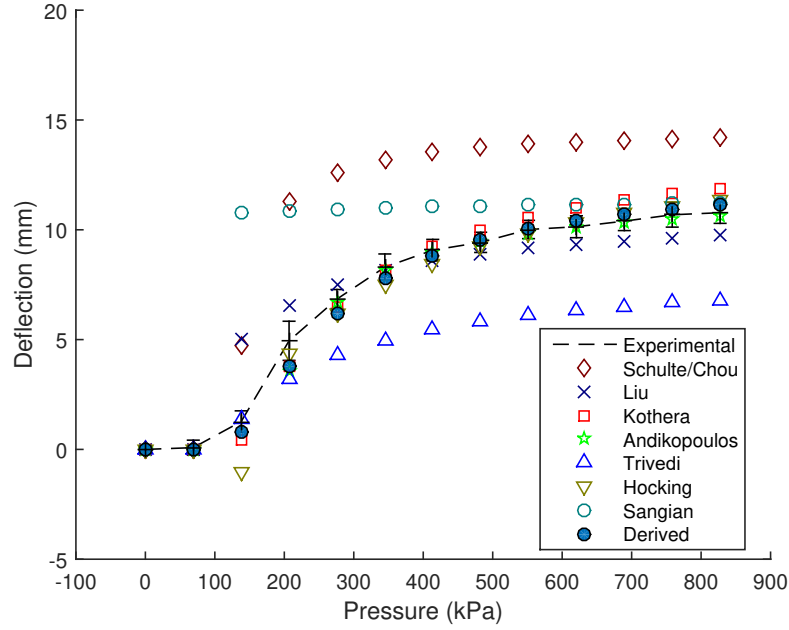


Figure 3.11: Experimental validation for 40 mm MPAM $\theta_0 = 36^\circ$, $r_i = 0.25$ mm, $r_o = 0.55$ mm, $r_n = 0.04$ mm, $m = 30$, $\phi = 5$ mm, $E = 0.35$ MPa, $\nu = 0.499$.

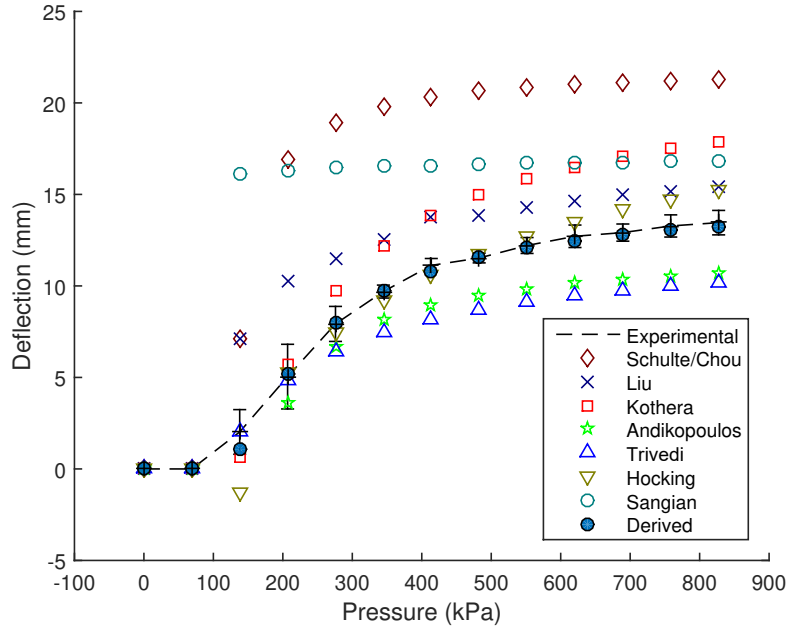


Figure 3.12: Experimental validation for 60 mm MPAM. $\theta_0 = 36^\circ$, $r_i = 0.25$ mm, $r_o = 0.55$ mm, $r_n = 0.04$ mm, $m = 30$, $\phi = 5$ mm, $E = 0.35$ MPa, $\nu = 0.499$.

other models show very large error in the stiffness value (in the order of 10) and are not plotted hence. Upon observation, it is found that at higher loads, the effect of conical ends are

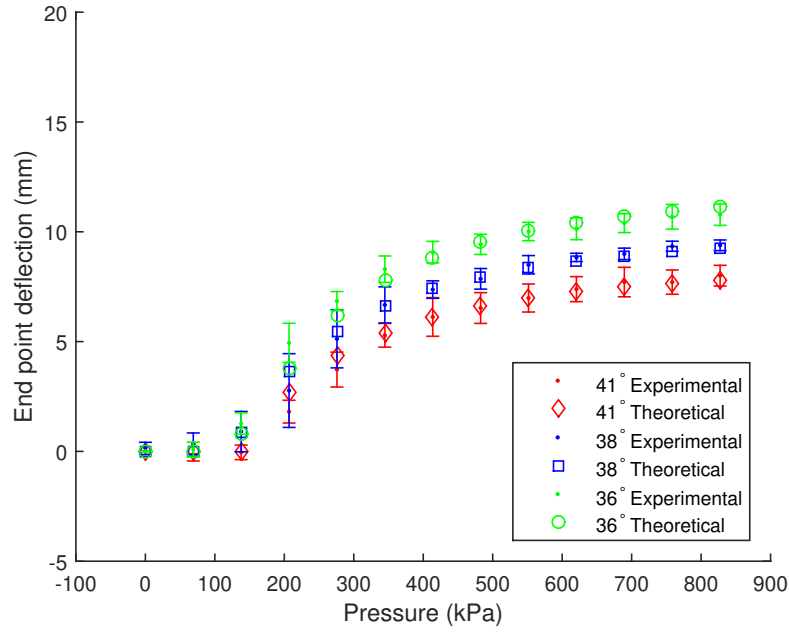


Figure 3.13: Experimental validation for different angle of windings $l_o = 40$ mm, $r_i = 0.25$ mm, $r_o = 0.55$ mm, $r_n = 0.04$ mm, $m = 30$, $\phi = 5$ mm, $E = 0.35$ MPa, $\nu = 0.499$.

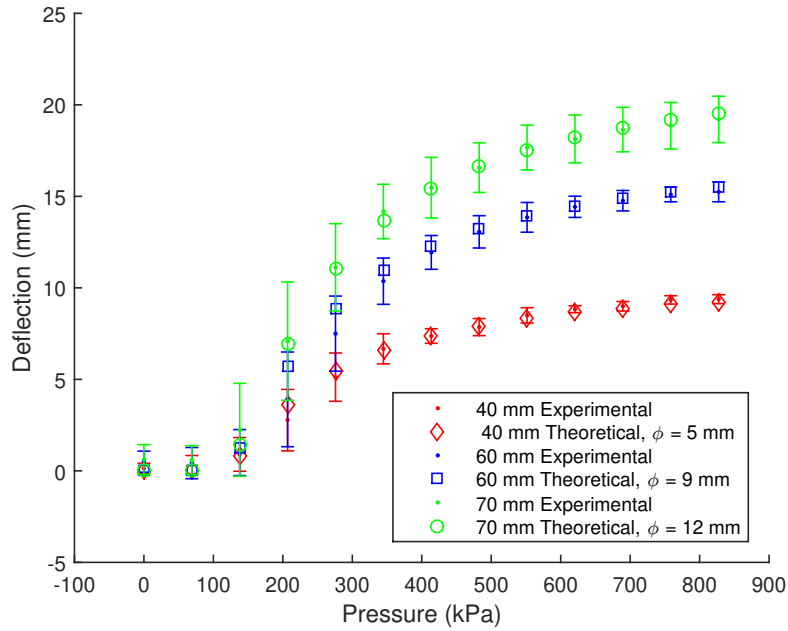


Figure 3.14: Experimental validation for MPAM wound at 38° angle. $r_i = 0.25$ mm, $r_o = 0.55$ mm, $r_n = 0.04$ mm, $m = 30$, $E = 0.35$ MPa, $\nu = 0.499$.

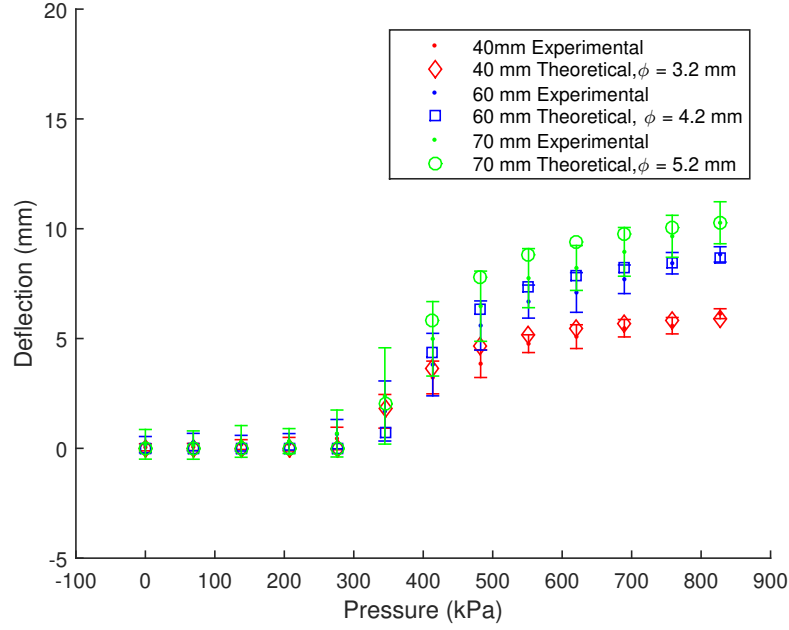


Figure 3.15: Experimental validation for MPAM with tube O.D 1.5 mm. $\theta_0 = 35^\circ$, $r_i = 0.25$ mm, $r_n = 0.04$ mm, $m = 30$, $E = 0.35$ MPa, $\nu = 0.499$.

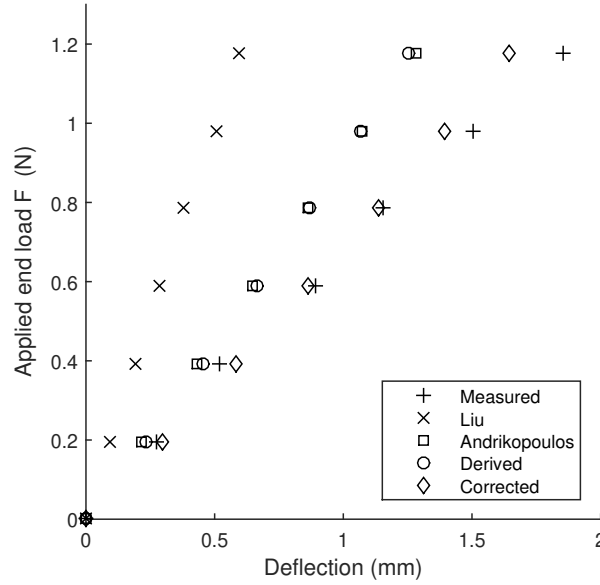


Figure 3.16: Axial force vs displacement comparison $P_i = 758$ kPa, $\alpha = 36^\circ$, $l_o = 45$ mm, $r_i = 0.25$ mm, $r_o = 0.55$ mm, $r_n = 0.04$ mm, $m = 30$, $\phi = 5$ mm, $E = 0.35$ MPa, $\nu = 0.499$

prominent, since the MPAM is axially stretched due to this loads. Due to this stretching caused by applied loads, the value ϕ is higher. An analytical model for this effect is not developed

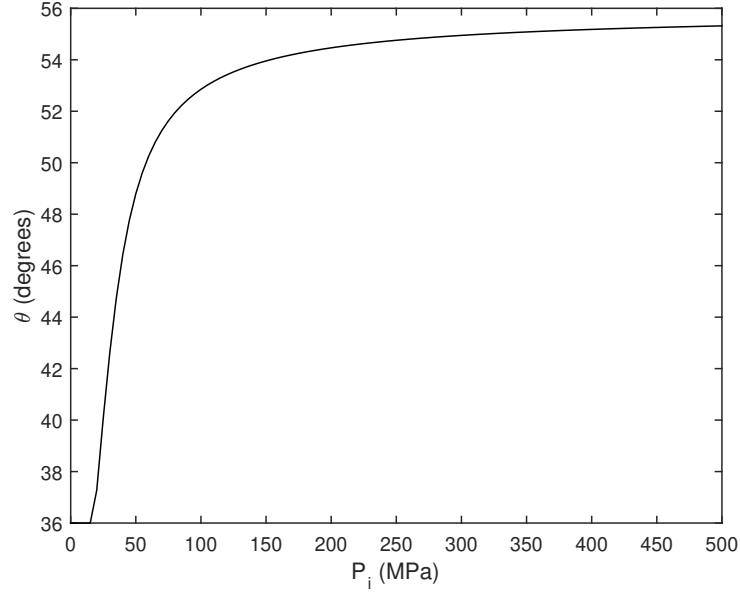


Figure 3.17: Evolution of final braid angle for large pressure range

for calculating the value of ϕ , but a proportional increase of the value ϕ based on the applied force, say $\hat{\phi} = \phi \frac{F}{k}$ (where k is a scaling factor), is shown to give much better approximation at higher loads. This corrected model is also plotted in Fig. 3.16.

The final theoretical braid angle for an extrapolated pressure value is plotted in the Fig. 3.17. We can see that the braid angle asymptotically reaches the locking limit of 54.7° . In this case, the limit is slightly overshoot at higher pressures. This is because the scaling factor $S_{\text{scale}}^{(1)}$ for contact area mentioned in the Cadwell's derivation is not considered in this formulation, which, is in fact a correction factor for the underestimation of radial force on tube. However, since we do not have definitive calculations to determine S_{scale} except by empirical measures, the same is not considered further.

From the above validation experiments we can conclude that, the developed model is able to predict the deformation of MPAM with good accuracy and consistency compared to other models. Theoretical model is able to predict the actual deformation with less than 7% error. The consistency of the model with respect to change in parameters such as initial length, initial braiding angle as well as the thickness of inner tube is experimentally validated. The developed model shows large error in predicting the stiffness of MPAM. However, an increase in the length of conical section proportional to the applied force shows much better conformation with the experimental value of stiffness. The application of this model on PAMs of diameter larger than 5 mm is not verified by the validation experiments and hence it is not possible to claim the

accuracy of this modeling strategy on regular sized PAMs.

3.5 Conclusions

It was found that most of the phenomenological models for PAM seem to be inconsistent with the statics of miniaturized PAMs especially to the change in initial parameters. A novel modeling strategy different from the conventional energy balance concept and which considers two major physical aspects of MPAM – the material property of the Silicone tube and the non cylindrical end-effects – has been derived. As opposed to the conventional modelling strategy, the complex axial components of force such as friction as well as the component of radial force from conical ends required to maintain static equilibrium of the MPAM are obtained by solving the model. Hence, separate accurate formulation of these terms are not necessary. The derived model could accurately predict the deformation of MPAM for a given applied pressure with less than 7% error. The consistency of model with changes in initial parameters such as length, braid angle as well as the thickness of tube is verified by validation experiments. The standard error between experimental results and theoretical results for different initial parameters is much less compared to the other models available in the literature. While the model under predicts the stiffness of pressurized MPAM, this is identified as due to the limitation in the model in addressing the stretching of conical end-section due to the applied force. A correction applied to the end-section length proportional to the applied force showed better conformation with the experimental results. The model also predicts the theoretical limiting angle of 54.7° at extrapolated pressure values.

Next chapter discusses the development and analysis of a novel flexible end-effector which makes use of three MPAMs for actuation. For kinematics analysis, the model of MPAM developed in this chapter is used to estimate the the pressure-deformation relationship of the MPAMs employed in the end-effector.

Chapter 4

Design, fabrication and analysis of flexible end-effector for endoscopic catheters

4.1 Introduction

Previous chapter detailed the fabrication, testing and characterization of miniaturized PAMs with maximum outer diameter of 2 mm. Since the muscle shows approximately 1 N/mm stiffness at 758 kPa pressure, a collection of muscles can be utilized in an endoscopic end-effector to successfully deflect the catheter tip. As mentioned in chapter 1, it is possible to find a few robotic designs in the literature which utilize pneumatic muscles for actuation. For example, in [26] and [146], three or more PAMs are grouped together along the circumference of a circle to form the robot. The tool is placed at the sealed end of the muscle bundle and by actuating the muscles individually, the tip can be deflected in different directions. Here, the stiffness of the robot in the unactuated state is imparted by the stiffness of the PAM bundle and will be ideal for robots which use PAMs with thick bladder. For the current application, such method will result in very low stiffness of end-effector and hence, an explicit stiffener should be provided. In reference [38], the author borrowed the design concept from cable-driven continuum robot which essentially is a flexible rod (backbone) actuated using a set of cables. This design could be used for the endoscopic end-effector as well, where MPAMs replacing the cables. One drawback in this design is that the guiding disks provided could impart friction which will result in rupture of the muscles unless the muscles are fixed to the disks. However, for short actuators, this would mean a reduction of the effective working length of the actuator and hence, reducing the overall contraction. Reference [147] shows another design where multiple

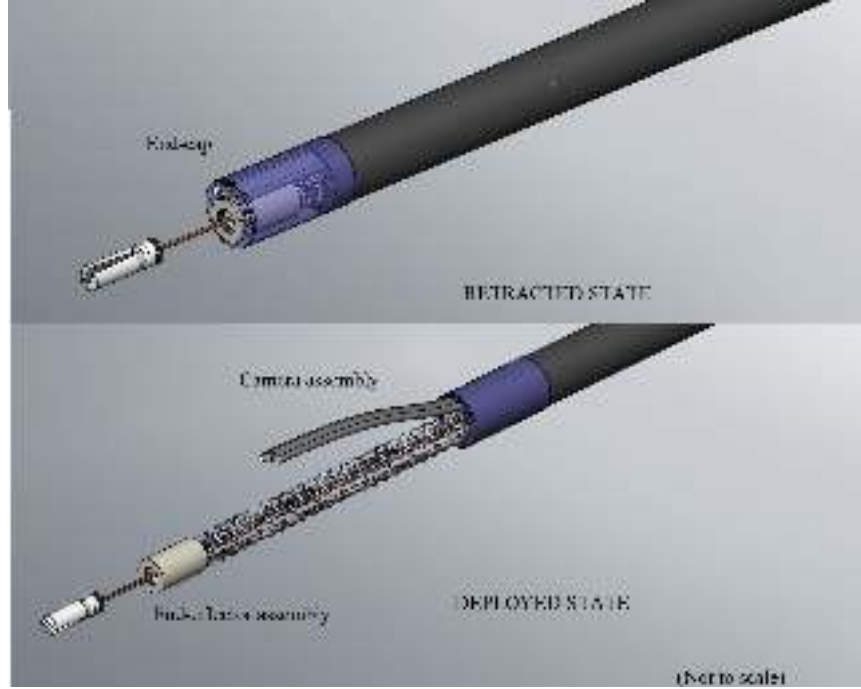


Figure 4.1: Conceptual design of endoscopic tip assembly

parallel manipulators are stacked to form a serial system with end-effector attached at to the surface of distal segment. The prismatic joints of the manipulators are pneumatic muscles in this case. It may be noted that this design will also not be efficient for the endoscopic end-effector since the overall length of the end-effector is limited to about 50 mm and incorporating multiple short MPAMs within the dimensions and thereby obtaining large deflections of the tip will be non-trivial, if not impossible.

Borrowing largely from these existing designs, an innovative end-effector design which provides both unactuated stiffness as well as enough force to deflect the endoscopic catheters, while conforming to the available dimensions is presented in this chapter. Section 4.2 details the design and fabrication of the novel end-effector. Since the proposed design does not utilize guiding discs as is the case of other robots available in the literature, a new forward kinematics model is proposed in section 4.3. Experimental validation of the model is shown in section 4.4. The inverse kinematics which takes input from the projected workspace of the end-effector and real-time implementation of the kinematic models are discussed in sections 4.5 and 4.6 respectively. Some representative examples of the implementation to demonstrate the concepts are shown in section 4.7 before summarizing the conclusions of the chapter in section 4.8.

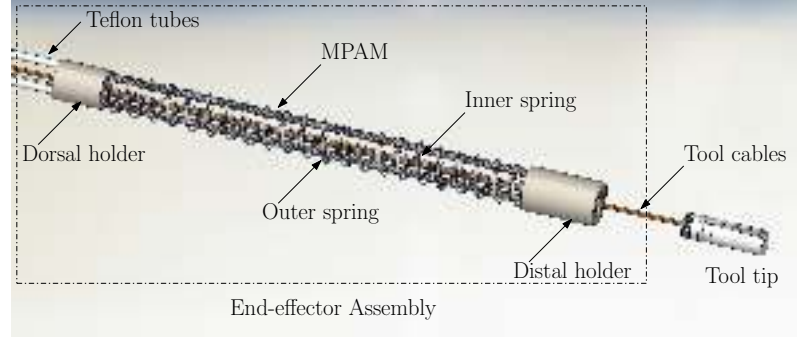


Figure 4.2: End-effector Design

4.2 End-effector design

The proposed modification at the distal end of endoscope is shown in Fig. 4.1. The system consists of three main components:

- A camera assembly which holds camera, lighting system and a nozzle for spraying water as well as pump air. The assembly may be pre-stressed to the shape shown in Fig. 4.1 such that it acts like an overhead camera during deployed state.
- An end-effector assembly with endoscopic tool/catheter attached to the tip. This assembly can be deflected independent to the camera assembly.
- A spring loaded end-cap which can be retracted using cables to reveal the end-effector assembly as well as the camera assembly whenever necessary.

The work presented in this thesis focuses on the end-effector assembly (here onwards called end-effector). The design of end-effector is shown in Fig. 4.2. The end-effector consists of two holders on either ends, each having a central hole of 3.5 mm diameter for catheter entry and three holes of 2 mm diameter, 120° apart for placement of MPAMs. When only one MPAM is pressurized, it contracts and the end-effector moves along the plane containing the MPAM and the catheter. When two MAPM's are actuated, the end-effector moves approximately along the bisector of actuation planes formed from individual actuation of MPAMs. Hence, by actuating one or two MPAMs, the end-effector can be positioned anywhere on the surface of a section of a hemisphere.

The separation between dorsal and distal holders decides the overall length of end-effector and hence the length of the MPAM used. A minimum end-effector deflection of 10 mm is desired for convenient positioning of the tip of a catheter and this is kept as a design target during the fabrication. It has been experimentally observed that air muscle length below 40 mm does

not produce a large enough force to bend standard commercial forceps catheter to required deflection. In addition, since the depth of view of a typical endoscopic camera is between 0 to 90 mm, 45 mm long air muscles were chosen in the design.

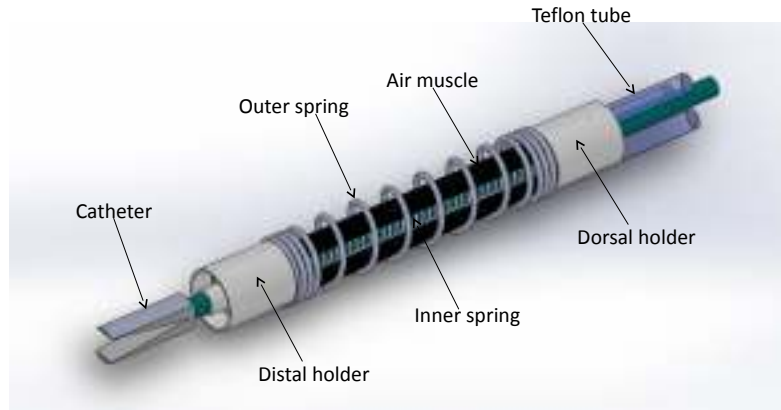


Figure 4.3: Design with separate catheter

As shown in Fig. 4.2, a wound coil of 4 mm outer diameter is fixed in the center. This coil serves two purposes—it acts as a passage for catheter without interfering with the pneumatic air muscles and also acts as a fulcrum on which the catheter will bend when air muscle is energized. The coil has high axial stiffness with minimal motion along the axis of the coil and low lateral stiffness thereby allowing it to bend easily—as a consequence, the end-effector workspace is a section of hemispherical surface. Almost all endoscopic catheters have a common design which consists of a closely wound coil which protects one or two cables used to actuate the catheter mechanism at the tip and a plastic sheath covering the coil. In the proposed design, it is possible to remove the catheter coil which is in fact redundant, since the inner-spring of the end-effector itself can act as the protective sheath. This will reduce the overall stiffness of the end-effector, resulting in better deflection and will also reduce the overall diameter of the end-effector. The design shown in Fig. 4.2 is in fact, the catheter integrated design. The design which uses separate catheter is shown in Fig. 4.3. The outer coil is highly flexible and is used to maintain the shape of the end-effector. The pneumatic air muscles are rigidly fixed to the top and bottom holders. While it is sealed at the top holder, the air muscles are connected at the bottom to Teflon tubes of 2 mm diameter which in turn is connected to the pneumatic circuitry. A maximum pressure of 827 kPa (120 psi) is applied to the MPAM. The volume of air inside the MPAM is approximately 30mm^3 and hence, even in case of MPAM rupture, this volume will not result in a safety issue. In addition to this, the flow control valve limits the volume flow rate of air into the MPAM to avoid sudden bleeding of compressed air from the reservoir to the MPAM. Fig. 4.4 shows the fabricated end-effector prototype with standard

forceps catheter inside. In its current form, the end-effector is 55 mm long and has a diameter of 9 mm.

In the following section, kinematics of the designed end-effector based on the static characteristics of the fabricated MPAM is discussed. A catheter-less end-effector is used for the initial study. This is because the stiffness of catheter used in end-effector will depend on the type of catheter used as well as the manufacturer. From the later sections, it can be seen that for an end-effector which actuates commercial catheters, the kinematic formulation will remain the same, since only the flexural rigidity of the end-effector will change with the inclusion of catheter, and this value could be experimentally calculated before implementation.



Figure 4.4: End-effector prototype with forceps

4.3 Forward kinematics of end-effector

The developed end-effector is similar to the tendon driven robots based on the actuation technique. The inner spring acts as the backbone and the tendons are replaced by MPAMs. A major difference between the current model with the conventional tendon driven models is the lack of guiding discs in our prototype as mentioned in section 4.1. Due to the absence of guiding discs, the MPAMs could drift sideways once the end-effector is deflected as shown in Fig. 4.5. Hence existing kinematic equations available in the literature for guided tendon routing (see for example [60] and [70]) shows large deviation from the experimental observations. To take into account the absence of guiding disks, a new kinematic model is developed which relates the position of the tip of the end-effector as a function of the deformation in the three MPAMs. This model is required for real-time control of the end-effector.

The main assumption is that when the end-effector is deflected, the system tries to move minimum distance so as to achieve an equilibrium position. Fig. 4.6 shows the backbone-actuator assembly along an axial section of end-effector (section AA from Fig. 4.5). The entire

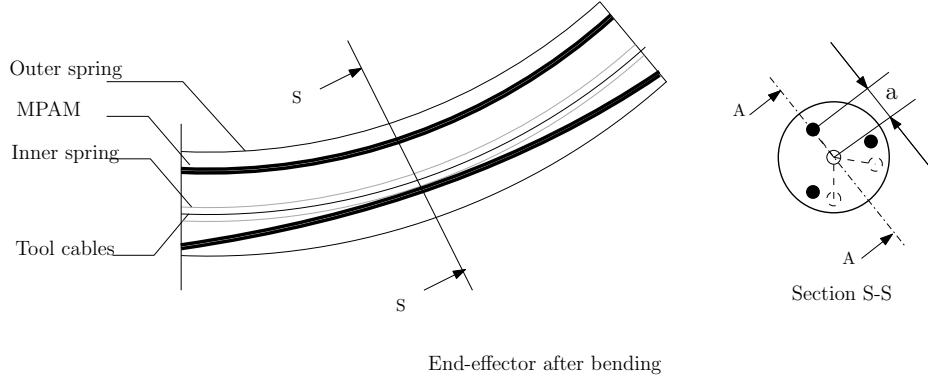


Figure 4.5: Tendon driven robot analogy

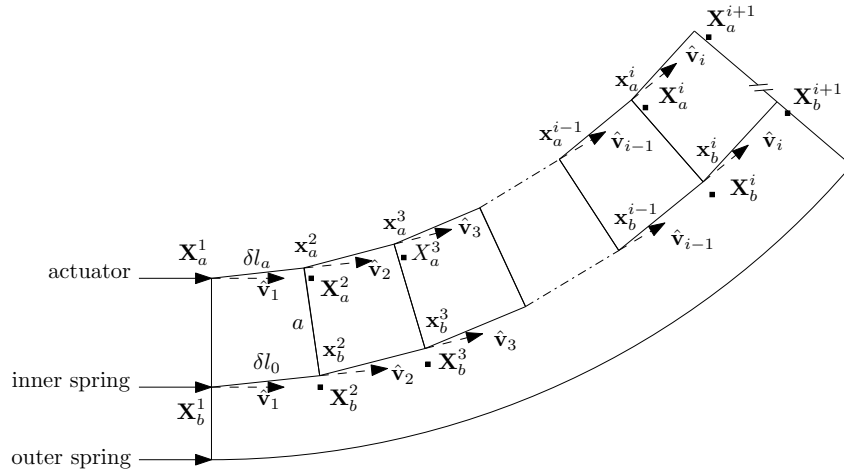


Figure 4.6: Backbone-actuator profile

length of end-effector is discretized into n segments, each segment representing the length at which the outer spring comes in contact with the MPAM. An axial load will cause change in length in inner spring. However, since three MPAMs are not actuated simultaneously, the loading on the end-effector is primarily the moment applied by the MPAMs and hence, the spring (backbone) is assumed to be of constant length throughout the actuation. The length of a backbone in a segment is given as $\delta l_0 = \frac{l_0}{n}$ and the length of actuator in a segment is $\delta l_a = \frac{l_a}{n}$ where l_a is the final length of MPAM after pressurizing. In un-actuated state, the segment forms a quadrilateral with co-ordinates $\mathbf{X}_b^i, \mathbf{X}_b^{i+1}, \mathbf{X}_a^{i+1}, \mathbf{X}_a^i$ as shown in the figure where the subscripts b and a represent backbone and MPAM respectively. For segment at the base of end-effector, $i = 1$ and $i = n$ at the tip. The natural undeformed initial positions \mathbf{X}_b^{i+1} and \mathbf{X}_a^{i+1} are found

out as

$$\mathbf{X}_b^{i+1} = \mathbf{X}_b^i + \delta l_0 \hat{\mathbf{v}}_i \quad (4.1)$$

$$\mathbf{X}_a^{i+1} = \mathbf{X}_a^i + \delta l_a \hat{\mathbf{v}}_i \quad (4.2)$$

$$\text{where, } \hat{\mathbf{v}}_i = \frac{\mathbf{X}_b^i - \mathbf{X}_b^{i-1}}{\|\mathbf{X}_b^i - \mathbf{X}_b^{i-1}\|} \quad (4.3)$$

For the initial segment ($i = 1$), the unit vector $\hat{\mathbf{v}}_1$ is perpendicular to the vector $\mathbf{X}_b^1 - \mathbf{X}_a^1$ along the initial axis of end-effector.

After deformation, the quadrilateral changes to $\mathbf{X}_b^i, \mathbf{x}_b^{i+1}, \mathbf{x}_a^{i+1}, \mathbf{X}_a^i$ where vectors in lower case characters represent deformed position. Since the distance between backbone and MPAMs are constrained by the outer spring to a fixed value, the length $\|\mathbf{x}_b^{i+1} - \mathbf{x}_a^{i+1}\| = a$ at all times. The deformed quadrilateral could be positioned in different configurations depending on the angle formed by $\mathbf{x}_a^{i+1} - \mathbf{X}_a^i$ and $\mathbf{X}_b^i - \mathbf{X}_a^i$. During actuation, since the MPAM becomes stiff compared to the other components, the natural configuration is assumed to be the one where MPAM has the least motion. Hence, the configuration of the deformed parallel manipulator is assumed to be the one which minimizes the displacement of tip \mathbf{x}_a^{i+1} (where the MPAM contacts the outer spring). To find the deformed configuration, we formulate the problem as

$$\min_{\mathbf{x}_b^{i+1}, \mathbf{x}_a^{i+1}} \|\mathbf{X}_a^{i+1} - \mathbf{x}_a^{i+1}\|$$

Subject to:

$$\begin{aligned} \|\mathbf{x}_b^{i+1} - \mathbf{X}_b^i\| &= \delta l_0 \\ \|\mathbf{x}_a^{i+1} - \mathbf{X}_a^i\| &= \delta l_a \\ \|\mathbf{x}_b^{i+1} - \mathbf{x}_a^{i+1}\| &= a \end{aligned} \quad (4.4)$$

The solution to the above optimization problem gives the co-ordinates of tips \mathbf{x}_b^{i+1} and \mathbf{x}_a^{i+1} . The iterative method starts from the base segment and proceeds towards the tip of the end-effector to determine the final pose of the end-effector backbone and the actuated MPAM. Since the other two MPAMs are not pressurized, they are very flexible and can move freely within the end-effector and their exact pose need not be considered in the formulation.

In the case of two MPAMs actuated together, the resultant moment due to these actuations can be written as

$$\mathbf{M} = \mathbf{a}_i \times \mathbf{F}_i + \mathbf{a}_j \times \mathbf{F}_j = \mathbf{a}_r \times \mathbf{F}_{\text{res}} \quad (4.5)$$

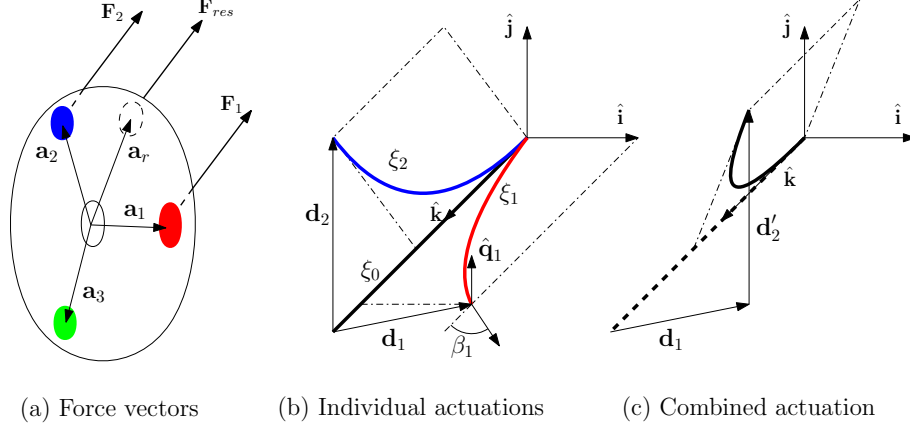


Figure 4.7: Displacement vector addition

where $\mathbf{a}_{i,j}$ are the position vectors of the tip of i^{th} and j^{th} MPAM and $\mathbf{F}_{i,j}$ are the applied forces on end-effector by the MPAMs. Let \mathbf{a}_r be the position vector of a hypothetical actuator whose resultant force $F_{\text{res}} = F_1 + F_2$ will provide the same moment as due to the other two MPAMs actuated together. In terms of direction cosines l_i and m_i , the equation can be rewritten as

$$\begin{aligned} a \left(l_1 \hat{\mathbf{i}} + m_1 \hat{\mathbf{j}} \right) \times F_1 \hat{\mathbf{k}} + a \left(l_2 \hat{\mathbf{i}} + m_2 \hat{\mathbf{j}} \right) \times F_2 \hat{\mathbf{k}} \\ = a \left(l_r \hat{\mathbf{i}} + m_r \hat{\mathbf{j}} \right) \times (F_1 + F_2) \hat{\mathbf{k}} \end{aligned} \quad (4.6)$$

where $\hat{\mathbf{i}}$, $\hat{\mathbf{j}}$ and $\hat{\mathbf{k}}$ denote the unit vectors along the co-ordinate axes. Simplifying the above and equating the components of $\hat{\mathbf{i}}$ and $\hat{\mathbf{j}}$, we get the direction cosines of the hypothetical actuator

$$l_r = \frac{(l_1 F_1 + l_2 F_2)}{F_1 + F_2}, \quad m_r = \frac{(m_1 F_1 + m_2 F_2)}{F_1 + F_2} \quad (4.7)$$

and hence, the plane which contains the resultant profile of end-effector.

If two MPAMs are pressurized simultaneously, the axial force generated at the tip will be large enough to compress the inner spring. The resultant deflection will be inwards in the $\hat{\mathbf{k}}$ direction which is not desired. Hence, MPAMs are pressurized only one after the other. From Fig. 4.7, the tip deflection from initial position (ξ_0 in the figure) due to individual actuation of two MPAMs (given by curves ξ_1 and ξ_2) are along the direction of force vectors represented by \mathbf{d}_1 and \mathbf{d}_2 respectively. When these MPAMs are pressurized successively in the order MPAM-1 followed by MPAM-2, then the vector \mathbf{d}_2 is rotated about β_1 angle which is the angle at the tip of ξ_1 with respect to $\hat{\mathbf{k}}$ axis. The rotation will be along the axis of rotation of the end-effector

$\hat{\mathbf{q}}_1$ when only the first MPAM is actuated. The resultant deflection will be in the direction of vector sum of \mathbf{d}_1 and \mathbf{d}'_2 where $\mathbf{d}'_2 = \hat{\mathbf{R}}_{(\hat{\mathbf{q}}_1, \beta_1)} \mathbf{d}_2$ is the rotated vector.

From the static model of MPAM derived in chapter 3, we obtain the deformed length corresponding to a given applied pressure and axial load. From the forward kinematic equations derived in section 4.3, we get the pose of end-effector corresponding to given displacement of MPAMs/tendons. Combining both the models, we obtain the pose of end-effector corresponding to pressure applied at MPAMs.

4.4 Experimental validation

In order to validate the developed model, end-effector prototype is subjected to different values of pressure and the pose of end-effector after deflection is compared with the values obtained from theoretical model. Two cameras are used to capture images from different angles and the 3D co-ordinates of the central (backbone) curve of end-effector is obtained using multiple view image reconstruction techniques [148]. A thin flexible film of white colour is applied on the end effector surface to facilitate control point identification. A high contrast marking relative to the colour of end holder is made at the tip so that the marker is easily identified in the captured images. To find the co-ordinates of the tip, respective pixels in the two images corresponding to the marker position is manually selected. The possible error in this method is in incorrectly identifying the marker pixels which will not more than 4 pixels size for both the images. For the scale and measurement set up used, this value is about 2 mm. While this method is only suitable for the validation experiments conducted for the paper, in actual practice, the pose could be reconstructed using the methods suggested in [149] which will be much faster and better for control purposes. The maximum error in reconstruction is approximately ± 2 mm at the tip.

Fig. 4.8 shows the deformation of end-effector as well as the re-constructed profile when one MPAM is pressurized. It may be noted that the reconstructed profile is limited to the tip of MPAM which is at 45 mm from the base, while the end-effector tip extends up to 55 mm due to the distal holder. By actuating three MPAMs individually, it is found out that the MPAMs are positioned at 307.5° , 219° and 75° angles from the positive $\hat{\mathbf{i}}$ axis as shown in Fig. 4.9. They are named R , G and B respectively for identification. By applying a 0.1 N transverse load at the tip of the end-effector, a deflection of approximately 15 mm is obtained. The flexural rigidity is then calculated using the standard beam equation.

The solution to kinematics of end-effector considering the MPAM statics is carried out using an iterative scheme. At first, the deformation of a single MPAM for zero applied axial load is found out using the theoretical model of MPAM. This value of deformation is used to calculate

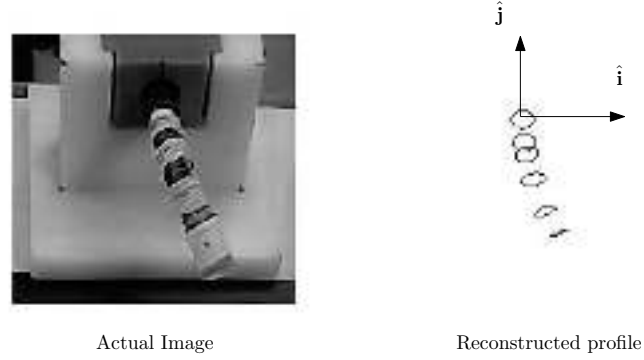


Figure 4.8: End-effector profile reconstruction using image analysis

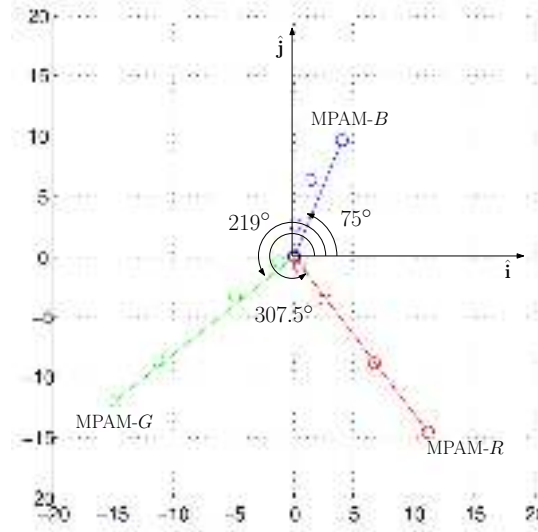


Figure 4.9: Angles showing MPAM arrangement in the end-effector

δl_a and the optimization problem in equation (4.4) is solved to get the pose of end-effector. The displacement of tip δ_e from the original position is calculated from the theoretical pose of end-effector. The moment that may be applied at the tip of end-effector in order to produce the same deflection is calculated using the equation $\delta_e = \frac{ML^2}{3EI}$, where EI is the flexural rigidity of the end effector. Since moment $M = a \times F$, we get the axial load F that should be produced by the MPAM in order to get the same deflection. Using this value of F , the deformation of single MPAM is re-calculated and the same procedure is repeated till the change in final deflection of end-effector is within a specified tolerance.

In order to validate the theoretical model, a pressure of 689.4 kPa(100 psi) is applied to MPAM- R . For no applied load, R gives $\Delta = 7.6$ mm contraction as per the derived theoretical model. The final length of MPAM will be $l_a = l_o - \Delta = 37.4$ mm. This value is used to predict

Table 4.1: Forward kinematics iteration for MPAM- R at $P_i = 689.4$ kPa

F (N)	Δ (mm)	δ_e (mm)	F^* (N)
0	7.6	22.8	1.69
1.69	6.9	20.4	1.51
1.51	6.9	20.4	1.51

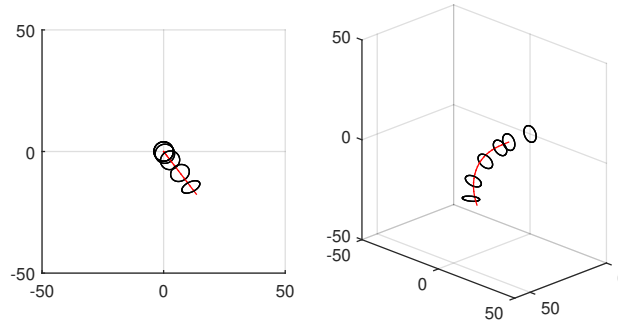


Figure 4.10: MPAM R actuated at 689.4 kPa

the pose of end-effector using the kinematic model where 15 segments are used for computation (length of one segment is equal to the pitch of the outer spring). The final pose of end-effector gives a tip deflection of $\delta_e = 24.5$ mm. The load F which MPAM has to apply on end-effector so as to obtain this value of deflection is calculated to be $F^* = 1.79$ N. Now, the deformation of MPAM is re-calculated with $F = F^* = 1.79$ N force where the deflection is 6.8 mm for 45 mm MPAM. The procedure is repeated as shown in Table 4.1. The value of deformation of MPAM to achieve equilibrium is found out to be 6.9 mm. The pose of end-effector obtained with final length of MPAM as $45 - 6.9 = 38.1$ mm is shown in Fig. 4.10 alongside the actual deflection of end-effector. The measured pose of the end-effector matches with the theoretical model with a maximum error of 1 mm at the tip. The time required to solve the forward kinematics is about 1.0 seconds on an Intel Pentium PC at 2.0 GHz.

As observed in chapter 3, there is an error in the calculated force-displacement profile for MPAM at higher values of axial load. The MPAM displacement is corrected for this error and the iteration table for the same pressure with the MPAM deflection corrected to Δ^* is shown in Table 4.2. It can be seen that the corrected value of MPAM deflection varies from the value predicted using the model by 0.2 mm. The change in tip deflection of end-effector due to this

Table 4.2: Forward kinematics iteration for MPAM- R at $P_i = 689.4$ kPa with MPAM deformation correction

F (N)	Δ (mm)	Δ^* (mm)	δ_e (mm)	F^* (N)
0	7.6	7.6	22.8	1.69
1.69	6.9	6.5	18.9	1.40
1.40	7.0	6.7	19.7	1.46
1.46	6.9	6.6	19.3	1.43
1.43	6.9	6.7	19.7	1.46

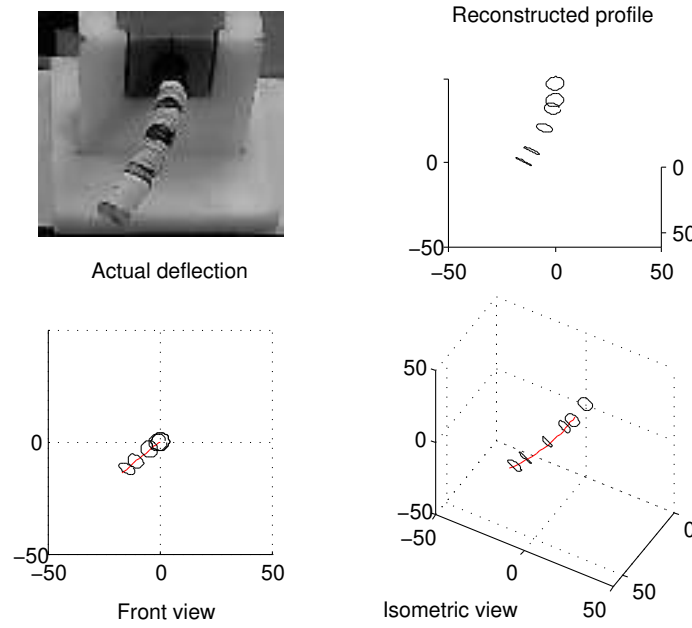


Figure 4.11: MPAM G actuated at 689.4 kPa

value is 1.05 mm which is well within the measurement error bounds.

Fig. 4.11 shows the actuation of MPAM- G with same value of pressure. Fig. 4.12 shows the comparison between theoretical and measured pose for MPAM- G actuated at 551.6 kPa (80 psi). The iteration table is shown in Table 4.3. The maximum error in tip deflection in this case is also found to be about 1 mm.

The following steps summarize the method in finding the final pose of end-effector when two MPAMs are actuated:

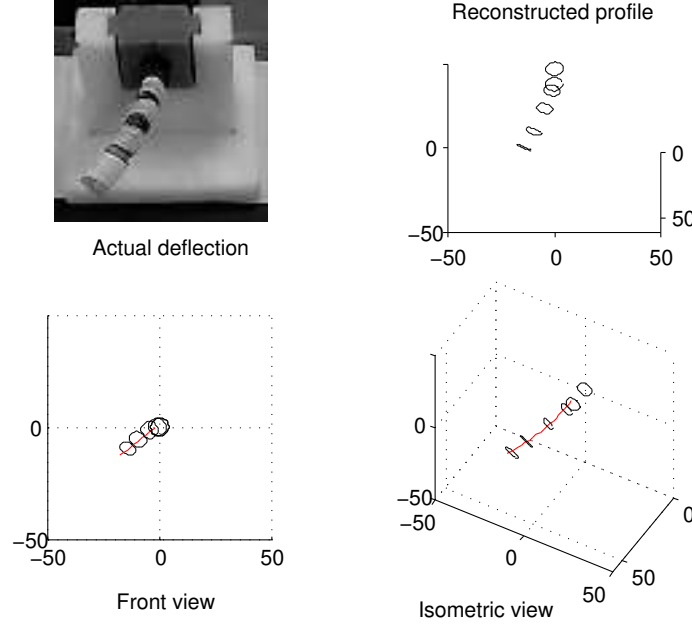


Figure 4.12: MPAM G actuated at 551.6 kPa

Table 4.3: Forward kinematics iteration for MPAM- R at $P_i = 551.6$ kPa

F (N)	Δ (mm)	δ_e (mm)	F^* (N)
0	7.1	21.2	1.57
1.57	6.4	18.5	1.37
1.37	6.4	18.5	1.37

1. Pose of end-effector ξ_1 when one MPAM, say, MPAM- R is pressurized individually is found out using the above formulation; tip deflection vector \mathbf{d}_1 is calculated.
2. Pose of end-effector ξ_2 when second MPAM, say, MPAM- G is pressurized individually is found out; tip deflection vector \mathbf{d}_2 is calculated.
3. Angle of end-point vector of MPAM- R is calculated using the equation:

$$\beta_1 = \cos^{-1} \left(\frac{\mathbf{x}_b^n - \mathbf{x}_b^{n-1}}{\|\mathbf{x}_b^n - \mathbf{x}_b^{n-1}\|} \cdot \hat{\mathbf{k}} \right) \quad (4.8)$$

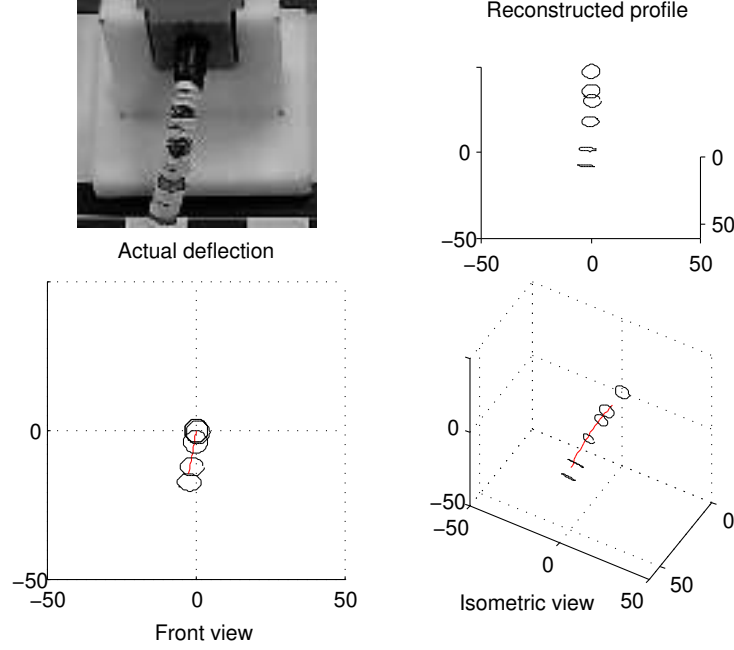


Figure 4.13: MPAMs R, G actuated at 689.4 kPa

4. Axis vector $\hat{\mathbf{q}}_1$ is found out using the equation:

$$\hat{\mathbf{q}}_1 = \frac{\mathbf{x}^n - \mathbf{x}^{n-1}}{\|\mathbf{x}^n - \mathbf{x}^{n-1}\|} \times \frac{\mathbf{x}^{n-2} - \mathbf{x}^{n-1}}{\|\mathbf{x}^{n-2} - \mathbf{x}^{n-1}\|} \quad (4.9)$$

5. Rotation matrix $\hat{\mathbf{R}}_{(\hat{\mathbf{q}}_1, \beta_1)}$ is populated using axis-angle method [150] and tip displacement of second MPAM, \mathbf{d}_2 is rotated to get \mathbf{d}'_2 .
6. Direction cosines of \mathbf{a}_r are calculated using equation (4.7). The plane containing the vector \mathbf{a}_r as well as the $\hat{\mathbf{k}}$ axis can be defined by its normal vector $(m_r)\hat{\mathbf{i}} + (-l_r)\hat{\mathbf{j}}$.
7. A straight line is drawn from the vector $l_0\hat{\mathbf{k}} + \mathbf{d}_1$ in the direction of \mathbf{d}'_2 . The intersection of this line with the plane defined in step 4) gives the final tip position.
8. The iteration is repeated with $n \rightarrow n - 1$ for the entire length of end-effector to obtain the final pose.

Fig. 4.13 shows the final deformation of end-effector when two MPAMs are actuated by 689.4 kPa (100 psi). The experimental results agree with the theoretical model well. The model is

Table 4.4: Forward kinematics iteration for $P_i = 413.6$ kPa

F (N)	Δ (mm)	δ_e (mm)	F^* (N)
0	6.2	17.9	1.32
1.32	5.6	15.2	1.13
1.13	5.7	15.8	1.17
1.17	5.7	15.8	1.17

also validated using wide range of pressure values. For example, the iteration Table 4.4 gives the deformation and axial load for a 413 kPa (60 psi) pressure input. The direction cosines of \mathbf{a}_r calculated using $F_1 = 1.61$ N (corresponding to 689 kPa pressure) and $F_2 = 1.28$ N (corresponding to 413 kPa pressure) are $l_r = -0.17$ and $m_r = -0.7$ respectively—i.e, the plane forms an angle 13.3° with the \hat{j} axis. For a pressure combination of 413 kPa for MPAM-*R* and 689 kPa for MPAM-*G*, the results are shown in Fig. 4.14. The predicted data as well as the reconstructed image for all the results show that the theoretical model gives very good estimate of the final deformation of end-effector.

4.5 Inverse kinematics of end-effector

In this section, the inverse kinematics of the end-effector is discussed. The deflection of end-effector with a standard 2.5 mm diameter forceps is shown in the Fig. 4.15. The maximum displacement of ~ 22.4 mm is observed at the end of distal holder and ~ 26.5 mm at tip of catheter when the MPAM is pressurized to 827 kPa. The pressure versus deflection for single air muscle actuation is plotted in Fig. 4.16. As mentioned in the earlier section, solution to the forward kinematics of end-effector, using the iterative approach takes about 1 second to complete and is not possible for real-time implementation in the current form. Due to this reason, a cubic curve is fitted on the deflection vs pressure data. A maximum limit of 827 kPa (120 psi) is set, beyond which negligible change in deflection is observed. With this approximation, the following approach can be used to find the pressure required for the catheter-tip to reach a particular position in the end-effector workspace.

Fig. 4.17 shows the front view of the end-effector with three air muscles actuated independently at maximum pressure. Three unit vectors $\mathbf{e}_1, \mathbf{e}_2, \mathbf{e}_3$ represents direction of displacement of air muscles MPAM-*R*, MPAM-*B* and MPAM-*G* actuated independently. Projection of the end-effector workspace onto a plane perpendicular to the axis of the end-effector is shown in Fig. 4.18 where $A_1\mathbf{e}_1, A_2\mathbf{e}_2, A_3\mathbf{e}_3$ are the vectors corresponding to the maximum displacement

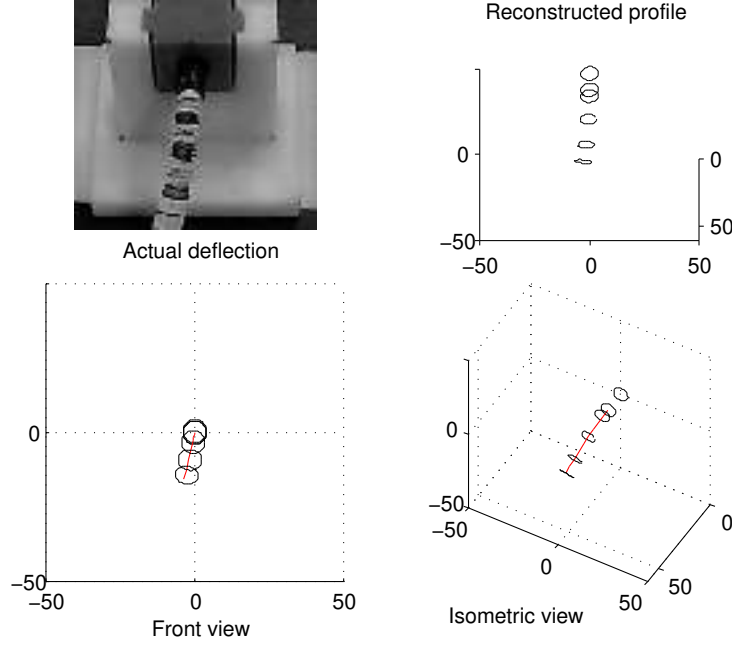


Figure 4.14: MPAM G at 689.4 kPa and R at 413 kPa



Figure 4.15: End effector with forceps at 827 kPa

in $\mathbf{e}_1, \mathbf{e}_2, \mathbf{e}_3$ directions respectively. The sector between \mathbf{e}_i and \mathbf{e}_j , $i, j = R, G, B$, $i \neq j$ is termed S_i . To access a particular point in S_i , say $\mathbf{v} = (v_x, v_y)^T$ (see Fig. 4.19), the air muscles i and j should be pressurized so as to obtain displacements \mathbf{a}_i and \mathbf{a}_j respectively.

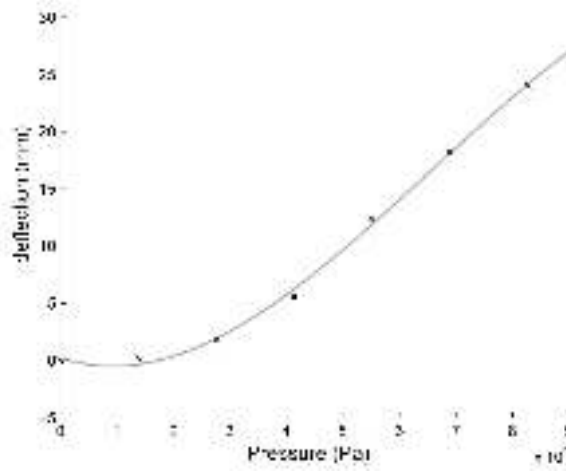


Figure 4.16: Pressure vs deflection, with catheter

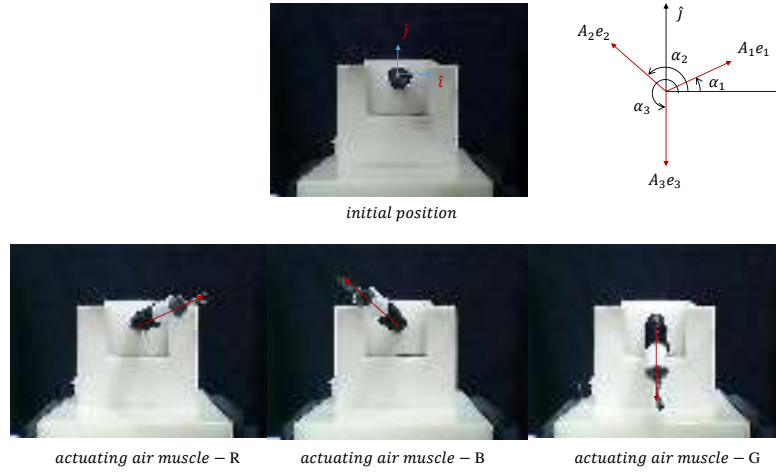


Figure 4.17: Front view of end-effector

With reference to Fig. 4.19, we get the following set of equations:

$$\begin{bmatrix} \mathbf{e}_i \\ \mathbf{e}_j \end{bmatrix} = \begin{bmatrix} \cos \alpha_i & \sin \alpha_i \\ \cos \alpha_j & \sin \alpha_j \end{bmatrix} \begin{bmatrix} \hat{\mathbf{i}} \\ \hat{\mathbf{j}} \end{bmatrix} \quad (4.10)$$

$$\begin{bmatrix} \hat{\mathbf{i}} \\ \hat{\mathbf{j}} \end{bmatrix} = \frac{\begin{bmatrix} \sin \alpha_j & -\sin \alpha_i \\ -\cos \alpha_j & \cos \alpha_i \end{bmatrix}}{\sin(\alpha_j - \alpha_i)} \begin{bmatrix} \mathbf{e}_i \\ \mathbf{e}_j \end{bmatrix} \quad (4.11)$$

$$v_x \hat{\mathbf{i}} + v_y \hat{\mathbf{j}} = \frac{\begin{Bmatrix} v_x [\sin \alpha_j \mathbf{e}_i - \sin \alpha_i \mathbf{e}_j] \\ + v_y [-\cos \alpha_j \mathbf{e}_i + \cos \alpha_i \mathbf{e}_j] \end{Bmatrix}}{\sin(\alpha_j - \alpha_i)} \quad (4.12)$$

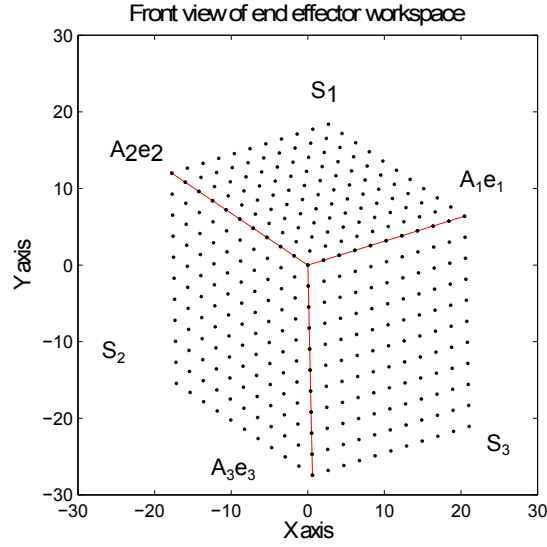


Figure 4.18: Projected workspace of end-effector

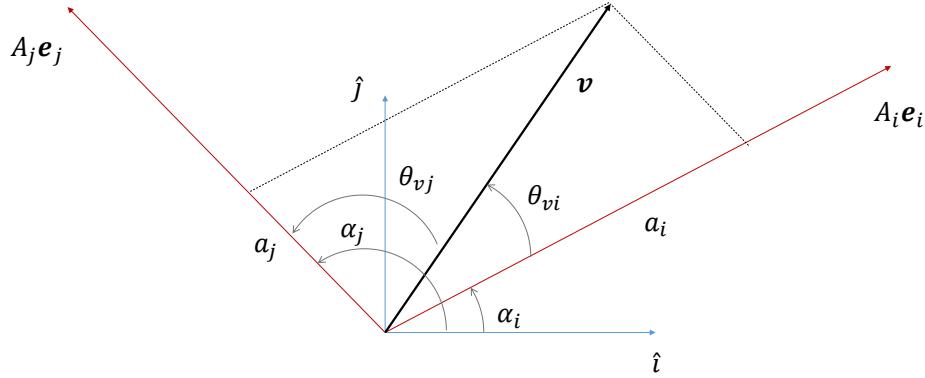


Figure 4.19: Vector in projected workspace

$$= \left[\frac{v_x \sin \alpha_j - v_y \cos \alpha_j}{\sin(\alpha_j - \alpha_i)} \right] \mathbf{e}_i + \left[\frac{-v_x \sin \alpha_i + v_y \cos \alpha_i}{\sin(\alpha_j - \alpha_i)} \right] \mathbf{e}_j \quad (4.13)$$

$$= a_i \mathbf{e}_i + a_j \mathbf{e}_j \quad (4.14)$$

The above expression gives the values of a_i and a_j which are the respective displacements from actuators i and j in order to access point (v_x, v_y) in the sector S_i . Fig. 4.20 and Fig. 4.21 show the experimental and expected end-effector position for a pre-defined input. The air muscle MPAM-G is pressurized at 689 kPa (100 psi) and MPAM-R is given maximum pressure. It can be seen that the predicted deflection and actual deflection varies by $\sim 9^\circ$.

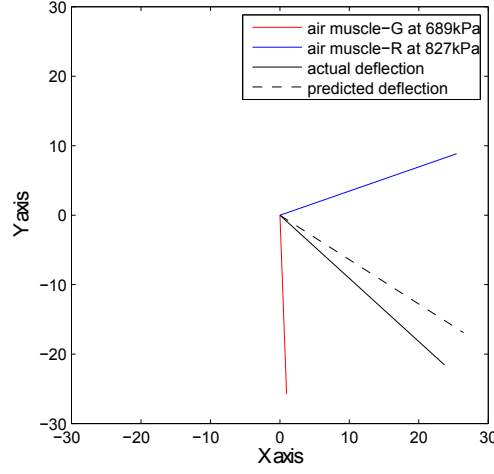


Figure 4.20: Experimental vs theoretical comparison of deflection in random direction



Figure 4.21: Deflection in resultant direction

4.6 Real-time implementation of end-effector actuation

The actuation of end effector is implemented in real time by taking input from a thumb stick which specifies the desired direction of motion. The analog signal from thumb stick is input to an Arduino Mega board which reads values from 0 to 1024 corresponding to 0 to 5 V— (0,0) is the top left corner and (1024,1024) is the bottom right corner. The origin of thumb stick, initially at (512,512) is made (0,0) by using the conversion

$$\begin{aligned} t_x &= (t_x - 512) \\ t_y &= -(t_y - 512) \end{aligned}$$

where (t_x, t_y) are the user input. The analog signals from thumb stick span a square surface from -512 to +512 in both left-right and top-bottom directions. The projected workspace of end-effector as given in previous section is then superimposed on this square surface, with

the projection completely inscribed in the square surface. One unit of thumb stick motion is equal to $\frac{\max\{A_i, \|A_i\mathbf{e}_i + A_j\mathbf{e}_j\|\}}{512}$ mm, with $i, j = R, G, B$. Using this conversion scale, the co-ordinates (v_x, v_y) can be found. Once (v_x, v_y) is obtained, sector S_i is found out using the condition $\theta_{vi} + \theta_{vj} = \alpha_j - \alpha_i$; θ_{vi} and θ_{vj} being the angle made by vector \mathbf{v} with the unit vectors \mathbf{e}_i and \mathbf{e}_j , respectively. The values a_i and a_j are then calculated using equation (4.14).

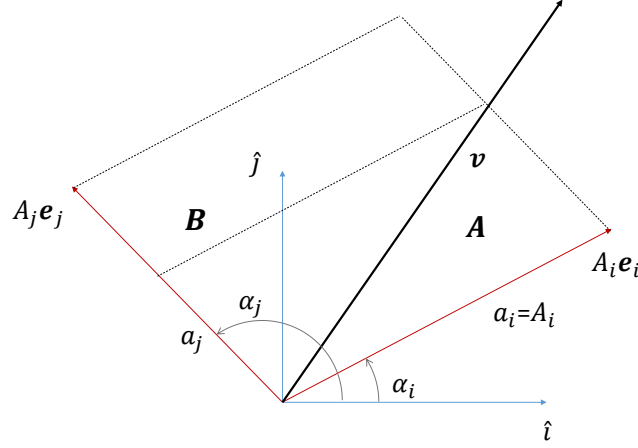


Figure 4.22: Vector outside workspace

Since some co-ordinates received from thumb stick lie outside the workspace of end-effector (see Fig. 4.22), these co-ordinates are accounted for, based on the algorithm given below:

- Find the subsection (A or B) which vector \mathbf{v} belongs to. The logic used is same as that of finding sectors, except that the vector \mathbf{e}_j is the resultant of $(\mathbf{e}_i + \mathbf{e}_j)$ for section A and \mathbf{e}_i is $(\mathbf{e}_i + \mathbf{e}_j)$ for section B.
- If \mathbf{v} is in sector A, $a_i = A_i$ (maximum displacement). For calculating a_j , let \mathbf{e}_v be unit vector in the direction of \mathbf{v} . From Fig. 4.22,

$$R\mathbf{e}_v = A_i\mathbf{e}_i + a_j\mathbf{e}_j \quad (4.15)$$

- If \mathbf{v} is in sector B, $a_j = A_j$, then

$$R\mathbf{e}_v = a_i\mathbf{e}_i + A_j\mathbf{e}_j \quad (4.16)$$

From the above equations, value of R and a_i are calculated.

Once (a_i, a_j) are found out, then the cubic equation for pressure is solved using `fsolve` function in MATLAB to get the required pressure in both the actuating air muscles.

4.7 Implementation examples

A number of experiments are performed to position the tip of a catheter by applying air pressure to three independent air muscles. In this section representative experimental results are shown.

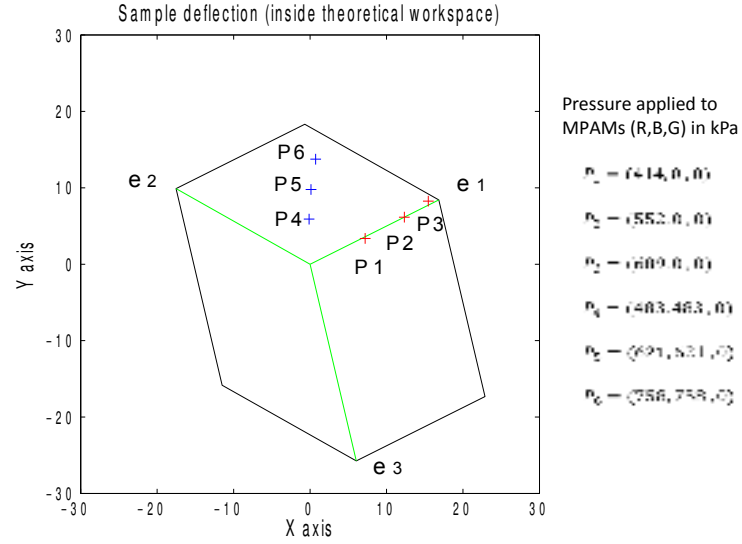


Figure 4.23: Tracing line in workspace

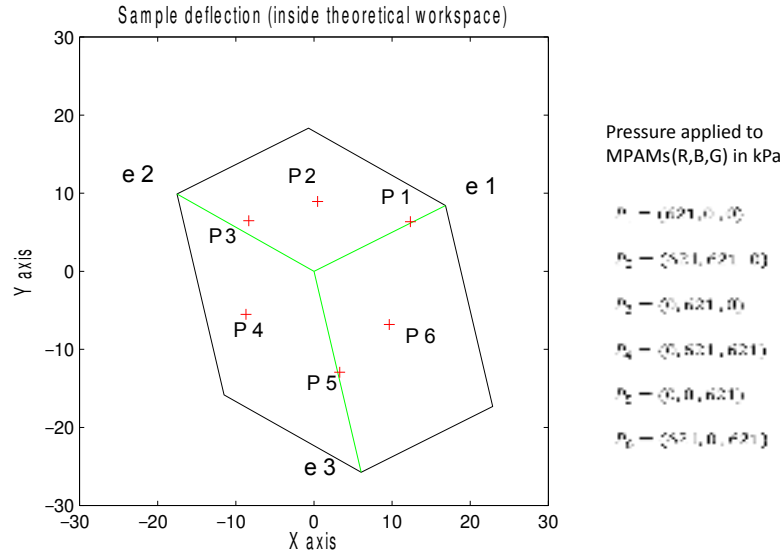


Figure 4.24: Tracing circle in workspace

The deflection at the tip of a standard forceps of outer diameter 2.5 mm and length 20 mm from the end-effector tip is measured and plotted. As mentioned earlier, the workspace is

divided into three sectors and a point P in workspace can be accessed by applying independent pressure (p_1, p_2, p_3) to the three air muscles (R, B, G) respectively. Fig. 4.23 shows the end-effector tracing a line in the workspace when a single air muscle is actuated. These are shown by points P_1, P_2 and P_3 (red markers). The applied pressure for each of these points is shown beside the figure. Fig. 4.23 also shows three representative points P_4, P_5 and P_6 (blue markers) obtained by actuating two air muscles. The pressures applied to the two actuators are mentioned beside the figure. An approximate circular tip motion of the catheter and the pressures applied to obtain the same is shown in Fig. 4.24. The results shows that arbitrary positioning of the forceps is possible in the workspace.

4.8 Conclusions

A novel end-effector for actuating endoscopic catheters is successfully designed and fabricated. The design uses three miniaturized pneumatic artificial muscle of 1.6 mm diameter enabling compactness while delivering required deflection and stiffness. The design differs from other robotic applications seen in the literature due to the absence of guiding discs to route the PAMs. Because of the absence of guiding discs, existing kinematic analyses available in the literature were not applicable to the end-effector and hence, a new forward kinematics model is developed. The model approximates the entire length of the end-effector as a series of connected parallelogram mechanisms and uses optimization based method to solve the pose of the actuated end-effector. A method to calculate the pose as well as the actuation plane for resultant actuation of two MPAMs is also discussed. An iterative method is derived to integrate the statics of the MPAM to the forward kinematics of end-effector. The experimental results show good agreement with the proposed model with maximum error less than 2mm at the tip. An algorithm to find the inverse kinematics of the end-effector, given the position of the end-effector tip at a particular point in the projection of workspace is proposed. The theoretical prediction varies from experimental results by $\sim 9^\circ$ in deflection angle. A method for real-time implementation of end-effector manipulation using a thumbstick is discussed and demonstrated.

Chapter 5

Motion planning of endoscopic robots

5.1 Introduction

As mentioned in chapter 1, the second issue faced by the endoscopists is in efficiently manoeuvring the scope through the GI tract. This chapter proposes an approach where the endoscope is considered as a continuum robot. The most popular and easily fabricated continuum robot is the cable driven elephant-trunk robot, which has multiple actuating segments, with each segment actuated using four cables placed 90° apart. Pulling the cable(s) result in the segment taking the shape of an arc of a circle. The forward kinematics of the cable driven continuum robot is to find the pose of the robot when the lengths of cables are given. In reference [60] Gravagne and Walker derived analytical expressions for the forward kinematics of elephant trunk robot using concepts from differential geometry. The co-ordinates of a point on the robot is determined using two parameters— α which is angle of rotation of the plane that contains the final configuration of the robot and about the initial axis of the robot¹ and the angle $\beta(s)$ made by the tangent of backbone with the initial axis (which varies along the length of the deformed backbone). In the paper by Starke et al [151], the authors cite the advantage of using robots with non-conventional tendon routing. Kinematic analysis of continuum robot with general tendon routing can be found in [67] as well. However, the derivations in [67] are applicable to tendon routes which can be analytically described and overall, the formulation is non-intuitive. Hence, a simpler and more direct formulation which can be applied to any general tendon routes will be advantageous.

The endoscope designed as a multi-segment continuum robot can be efficiently manoeuvred through the GI tract with the motion planned so as to avoid collision with the walls of the tract. As mentioned in chapter 1, the medial axis of the GI tract (locus of centroid of the cross-sections

¹The configuration of the robot will always be in a plane and is shown to take the shape of an arc of a circle.

of the tract) is a reasonable choice for the path through which the tip of the endoscopic robot shall trace. Once the path is given, finding the configuration of the robot which avoids collision with the tract walls constitutes redundancy resolution of the hyper-redundant robot. The collision avoidance can be achieved locally—by means of sensors [152], [153] or globally—where the obstacles are known apriori [53]. While the first method is mostly used for environments with moving obstacles, the latter is used for static environments. Considering the application in hand, global motion planning would suffice, since the patient will be stationary throughout the procedure, and also, the GI tract profile can be determined using MRI based imaging which is already being used in surgery ([154], [155]). Once the profile of the tract is known, tractrix based minimization approach mentioned in [88] can be used to plan a smooth and ‘realistic’ motion. However, in the special case of motion through confined spaces within a narrow bounded path—which hereafter we call “duct”, directly implementing the algorithm would require modelling the entire half space outside the duct as obstacles which is impractical. Hence, an efficient motion planning algorithm for motion inside confined narrow bounded paths may be developed.

The work presented in this chapter is organized as follows. In section 5.2, the kinematics of a single segment of continuum robot is analyzed. A new formulation is proposed for the forward kinematics of the continuum robot which uses optimization based method. The formulation for robot manipulation in 2D as well as the validation of the method is discussed in section 5.2.1. Section 5.2.2 details the method to extend the concepts for manipulation in 3D and as well as the validation of the method through simulations. After discussing the kinematics of a single segment of continuum robot, the motion planning of the entire hyper-redundant robot through the confinement of GI tract is discussed in section 5.3. Firstly, an overview of the tractrix-based motion planning is discussed. Then the proposed algorithm for motion planning through ducts in 2D and 3D with different ways of representing the ducts are discussed in detail in sections 5.3.2 and 5.3.3 respectively. Simulation of an endoscopic robot travelling through the GI tract is carried out in section 5.3.4. Finally, a few limitations of this method is discussed in section 5.3.5 before summarizing the conclusions in section 5.4.

5.2 Kinematics model for continuum robot

In this section, a new approach in modelling the forward kinematics of continuum robot is discussed. The modelling strategy is based on discretization of the continuum robot and using an optimization scheme similar to the approach discussed in section 4.3. The method is shown to be simpler in implementation and has the potential to be extended to robots with general tendon routing.



Figure 5.1: Discretization of robot in 2D plane

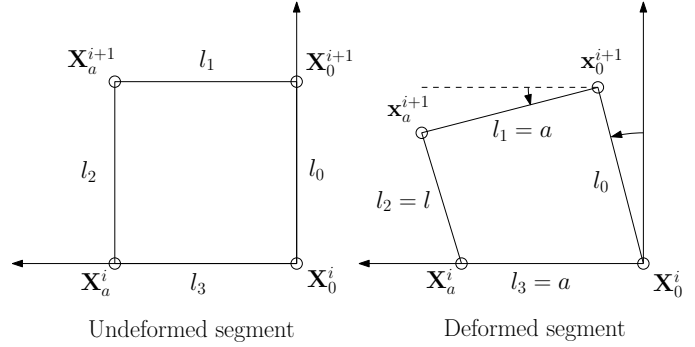


Figure 5.2: Nomenclature for single segment

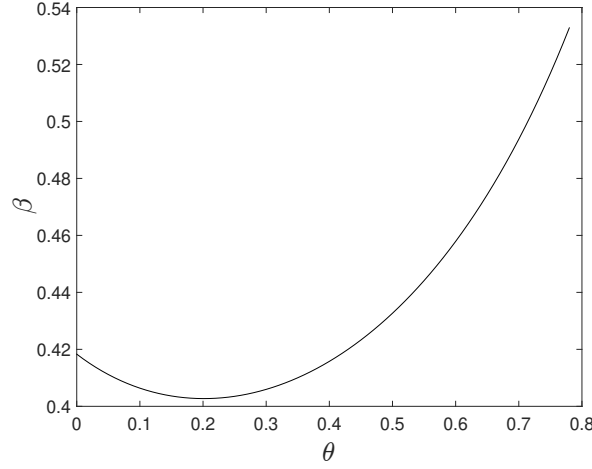
5.2.1 Forward kinematics of 2D continuum robot

In a cable driven continuum robot with two pairs of cables, if the two opposing cables in one of the pairs (cables which are 180° apart) are actuated, the robot will be restricted to move within a 2D plane. Among the opposing cable duo, only one cable is pulled at a time, since otherwise, the robot can buckle. In this section, a new method in formulating the forward kinematics of 2D planar continuum robot is discussed.

The proposed formulation assumes the profile of the continuum robot as a set of connected 4 bar parallel linkages. To this end, the robot is discretized into n number of segments along the backbone of the continuum robot as shown in Fig. 5.1. In this approach, only one cable from the opposing cable pair is considered, as it can be seen in the later part of the section that the other cable does not have any role in manipulation of the robot in the quadrants containing the actuated cable¹. With reference to Fig. 5.2, one segment of the continuum robot can be approximated as a 4-bar linkage, with the first crank, coupler, second crank and fixed link having lengths l_0 , l_1 , l_2 and l_3 respectively. Since the cables pass through holes present in the guide disks, the lengths $l_1 = l_3 = a$ where a is the constant spacing between the backbone and the cables. For the robot of length L_0 measured along the backbone, the length of the first crank $l_0 = \frac{L_0}{n}$. When the cables are actuated to a final length of $L_a = L_0 - \Delta L_a$ where ΔL_a is the prescribed change in length of the cable, the length of second crank, $l_2 = l = \frac{L_a}{n}$. From the loop-closure constraint equations of the 4-bar linkage located at the base of continuum robot, we get

$$f(\theta, \beta) = l_0^2 + 2a^2 - l^2 + 2al_0 \sin(\theta - \beta) - 2a(l_0 \sin \theta + a \cos \beta) = 0 \quad (5.1)$$

¹The opposing cable is used to retract the robot to its original position if the backbone material is not perfectly elastic, and for manipulation in the opposing direction of the first cable.


 Figure 5.3: variation of β with θ

where θ is the angle made by the first crank and the axis of backbone while β is the coupler angle measured relative to the fixed link. Plotting the values of θ and β , we can see from Fig. 5.3 that a minimum exists for $\beta - \theta$ curve for a given set of length parameters.

Differentiating the above equation with respect to θ and setting $\frac{d\beta}{d\theta} = 0$ and simplifying, we get

$$\cos(\theta - \beta) = \cos \theta$$

From the above equation, we can get the value of crank angle (and subsequently a configuration of the linkage) where the rate of change of coupler angle with respect to the crank angle is zero. This is given by

$$\beta = 2(\theta - k\pi) \quad (5.2)$$

where k is an integer.

In the initial un-actuated configuration, the lengths of link are $l_0 = l_2 = \frac{L_0}{n}$. In this position, the initial coupler angle is zero. After actuation, the nearest minimum for the coupler angle (from zero value) appears when $k = 0$, or $\beta = 2\theta$ for small displacements of the first crank. In what follows, it is shown that the configuration which produces minimum change of coupler angle is the same as the configuration obtained analytically by Gravagne and Walker [60].

Substituting $\theta = \frac{\beta}{2}$ in equation (5.1) and simplifying, we get

$$-l^2 + \left(l_0 - 2a \sin\left(\frac{\beta}{2}\right) \right)^2 = 0 \quad (5.3)$$

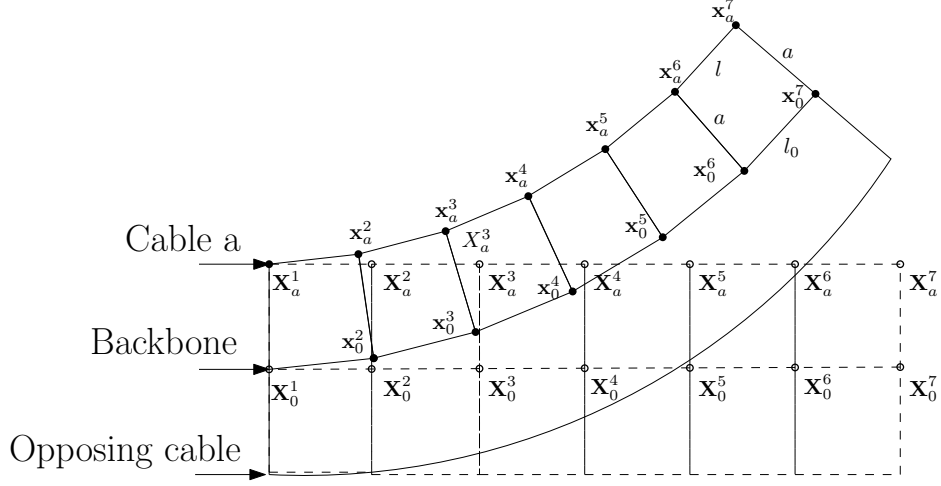


Figure 5.4: Assembly of 4 bar linkages for iteration procedure

Since l takes only positive values, we get

$$\sin \frac{\beta}{2} = \frac{l_0 - l}{2a} \quad (5.4)$$

The assembled discrete segments represent the robotic continuum for large values of n . In that case, the right-hand side of the above equation will be very small. For small angles, we get

$$\beta = \frac{l_0 - l}{a} \quad (5.5)$$

The value of coupler angle for the distal tip, which is same as the angle $\beta(L_0)$ in the derivation shown in [60], can be found by multiplying the above expression for β with the total number of segments n . The value of coupler angle so obtained,

$$\beta(L_0) = n \frac{l_0 - l}{a} = \frac{\Delta L_a}{a} \quad (5.6)$$

is same as the value obtained analytically in [60].

Since it has been shown that the forward kinematics of continuum robot can be obtained by minimizing the coupler angle of approximated 4 bar parallel linkages, the following formulation may be used to implement the optimization procedure:

Let the co-ordinates of the ends of the coupler attached to the first crank and the second crank in the undeformed position be denoted by \mathbf{X}_0^{i+1} and \mathbf{X}_a^{i+1} , respectively. The corresponding

deformed positions are denoted by \mathbf{x}_0^{i+1} and \mathbf{x}_a^{i+1} , respectively. Similarly, the co-ordinates of the ends of the fixed link attached to the first crank and the second crank are \mathbf{X}_0^i and \mathbf{X}_a^i , respectively. For the segment at the base of robot $i = 1$ and $i = n$ at the tip. With the above, the optimization problem may be formulated as:

$$\underset{\mathbf{x}_0^{i+1}, \mathbf{x}_a^{i+1}}{\operatorname{argmin}} \quad \arccos \left(\left(\frac{\mathbf{X}_0^i - \mathbf{X}_a^i}{\|\mathbf{X}_0^i - \mathbf{X}_a^i\|} \right) \cdot \left(\frac{\mathbf{x}_0^{i+1} - \mathbf{x}_a^{i+1}}{\|\mathbf{x}_0^{i+1} - \mathbf{x}_a^{i+1}\|} \right) \right)$$

Subject to:

$$\begin{aligned} \|\mathbf{x}_0^{i+1} - \mathbf{X}_0^i\| &= l_0 \\ \|\mathbf{x}_a^{i+1} - \mathbf{X}_a^i\| &= l \\ \|\mathbf{x}_0^{i+1} - \mathbf{x}_a^{i+1}\| &= a \end{aligned} \quad (5.7)$$

Given data: $\mathbf{X}_0^i, \mathbf{X}_0^{i+1}, \mathbf{X}_a^i, \mathbf{X}_a^{i+1}, l_0, l, a$

The solution to the above optimization problem gives the co-ordinates of tips \mathbf{x}_0^{i+1} and \mathbf{x}_a^{i+1} and the iterative method starts from the base segment and proceeds towards the tip of the robot. With reference to equation (5.4), in order to ensure that the right-hand side of the equation is always less than 1, the value of n may be chosen such that

$$n > \frac{L_0 - L_a}{2a} \quad (5.8)$$

Fig. 5.5 shows the profile plotted for a continuum robot using the solution obtained from analytical method as well as the discretized optimization method solved using `fmincon` in MATLAB. The solution, as proved before, is exact except for the tolerances in the numerical procedure. Fig. 5.6 shows that the profile remains similar with different number of segments.

The extension of this approach to 3D continuum robots is discussed in the next section.

5.2.2 Forward kinematics of 3D continuum robot

If both pairs of cables are actuated simultaneously, the continuum robot will assume a deformed pose in 3D space. For simultaneous actuation, the discretization of robot is carried out as shown in Fig.5.7. Here, the backbone along with the actuating cables which are placed at an angle $\phi = 90^\circ$ apart can be considered as a set of two adjoined 4 bar linkages (a 7-bar linkage). The two quadrilaterals have the vertices $(\mathbf{X}_0^i, \mathbf{X}_0^{i+1}, \mathbf{X}_a^{i+1}, \mathbf{X}_a^i)$ and $(\mathbf{X}_0^i, \mathbf{X}_0^{i+1}, \mathbf{X}_b^{i+1}, \mathbf{X}_b^i)$ initially. These quantities change to $(\mathbf{X}_0^i, \mathbf{x}_0^{i+1}, \mathbf{x}_a^{i+1}, \mathbf{X}_a^i)$ and $(\mathbf{X}_0^i, \mathbf{x}_0^{i+1}, \mathbf{x}_b^{i+1}, \mathbf{X}_b^i)$ after actuation. The

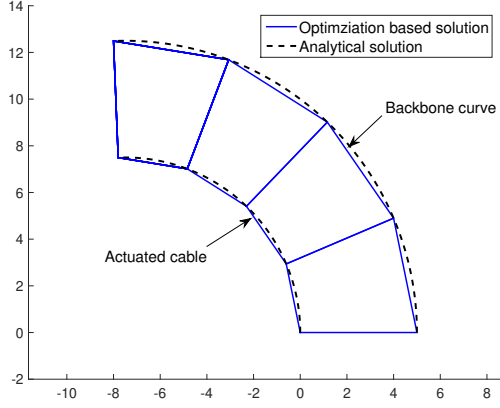


Figure 5.5: Comparison between analytical and optimization based solutions

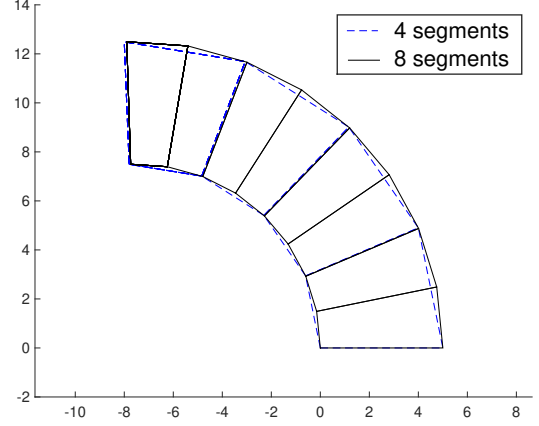


Figure 5.6: Solution with increased number of segments

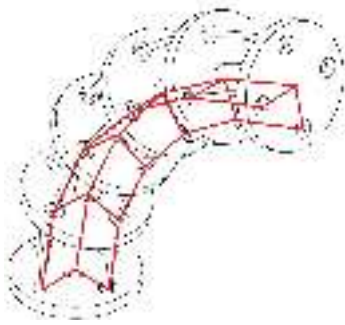


Figure 5.7: Discretization of robot in 3D

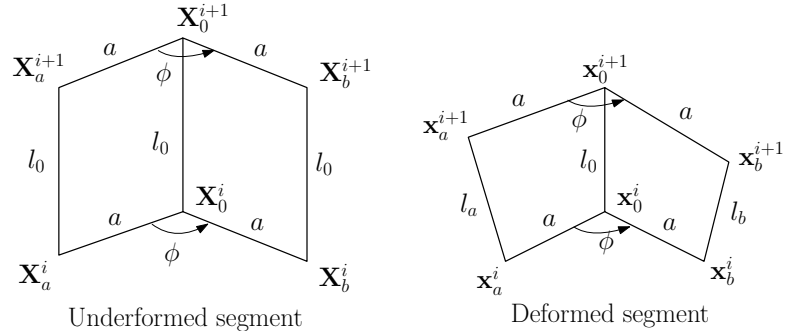


Figure 5.8: Nomenclature of segment in 3D

subscripts a and b are used to denote the respective values for the linkages formed by cable pairs a and b respectively. The coupler angles may be defined as β_a and β_b for the two 4-bar linkages.

Since the deformation of the robot is commutative– i.e., the actuation is the same irrespective of the order of actuating the cables, the final pose will be the one where coupler angles of both the linkages are minimized simultaneously and independently. Hence, the pose can be determined from solving the optimization problem

$$\begin{aligned} \underset{\mathbf{x}_b^{i+1}, \mathbf{x}_a^{i+1}}{\operatorname{argmin}} \quad & \left[\arccos \left(\left(\frac{\mathbf{X}_0^i - \mathbf{X}_a^i}{\|\mathbf{X}_0^i - \mathbf{X}_a^i\|} \right) \cdot \left(\frac{\mathbf{x}_0^{i+1} - \mathbf{x}_a^{i+1}}{\|\mathbf{x}_0^{i+1} - \mathbf{x}_a^{i+1}\|} \right) \right) \right]^2 + \\ & \left[\arccos \left(\left(\frac{\mathbf{X}_0^i - \mathbf{X}_b^i}{\|\mathbf{X}_0^i - \mathbf{X}_b^i\|} \right) \cdot \left(\frac{\mathbf{x}_0^{i+1} - \mathbf{x}_b^{i+1}}{\|\mathbf{x}_0^{i+1} - \mathbf{x}_b^{i+1}\|} \right) \right) \right]^2 \end{aligned} \quad (5.9)$$

Subject to:

$$\begin{aligned}
 \|\mathbf{x}_0^{i+1} - \mathbf{X}_0^i\| &= l_0 \\
 \|\mathbf{x}_a^{i+1} - \mathbf{X}_a^i\| &= l_a \\
 \|\mathbf{x}_b^{i+1} - \mathbf{X}_b^i\| &= l_b \\
 \|\mathbf{x}_0^{i+1} - \mathbf{x}_a^{i+1}\| &= a \\
 \|\mathbf{x}_0^{i+1} - \mathbf{x}_b^{i+1}\| &= a \\
 \arccos\left(\left(\frac{\mathbf{x}_0^i - \mathbf{x}_a^i}{\|\mathbf{x}_0^i - \mathbf{x}_a^i\|}\right) \cdot \left(\frac{\mathbf{x}_0^i - \mathbf{x}_b^i}{\|\mathbf{x}_0^i - \mathbf{x}_b^i\|}\right)\right) - \arccos\left(\left(\frac{\mathbf{X}_0^i - \mathbf{X}_a^i}{\|\mathbf{X}_0^i - \mathbf{X}_a^i\|}\right) \cdot \left(\frac{\mathbf{X}_0^i - \mathbf{X}_b^i}{\|\mathbf{X}_0^i - \mathbf{X}_b^i\|}\right)\right) &= 0
 \end{aligned} \tag{5.10}$$

Given data: $\mathbf{X}_0^i, \mathbf{X}_0^{i+1}, \mathbf{X}_a^i, \mathbf{X}_a^{i+1}, \mathbf{X}_b^i, \mathbf{X}_b^{i+1}, l_0, l_a, l_b, a$

where $l_a = \frac{L_a}{n}$, $l_b = \frac{L_b}{n}$ and the last equality constraint ensures that the separation between the cables remains constant even after deformation.

In Fig. 5.9 and Fig. 5.10, the pose of robot with two cables actuated by equal amounts as well as by different values are shown. As is the case with the 2D, analytical solution and optimization based solution varies only by the numerical error induced due to the optimization scheme.

To summarize, it is shown that the forward kinematics of a cable-driven continuum robot, with a fixed tendon spacing can be calculated using an optimization based approach. The actuating cable of the continuum robot as well as the backbone are discretized to a number of segments and the two are considered as the two cranks of a 4-bar linkage. The constant spacing between the cable and the backbone separates the cranks and form the fixed link as well as the coupler. Minimizing the coupler angle from the stationary initial position based on the constraints imposed by the cable lengths, backbone length as well as the constant spacing between the cable and backbone, a unique pose is obtained for the robot. This unique pose is shown to match the solution obtained using differential geometric approach [60].

It is worth noting that the approach is applicable only if the given lengths are constant. For a robot which does not have guiding disks to keep a constant cable spacing, a will vary and the approach detailed in section 4.3 may be used. For the case where the cables are passed through guiding disks with holes drilled with different spacings, the cables will not drift in circumferential direction. In reference [67], the forward kinematics of such a system with general tendon routing is posed using a set of differential equations based on Cosserat theory. However, as mentioned earlier in section 5.1, the expressions are non-intuitive and are applicable to tendon routes that can be analytically expressed. In the optimization based method proposed in this section, the

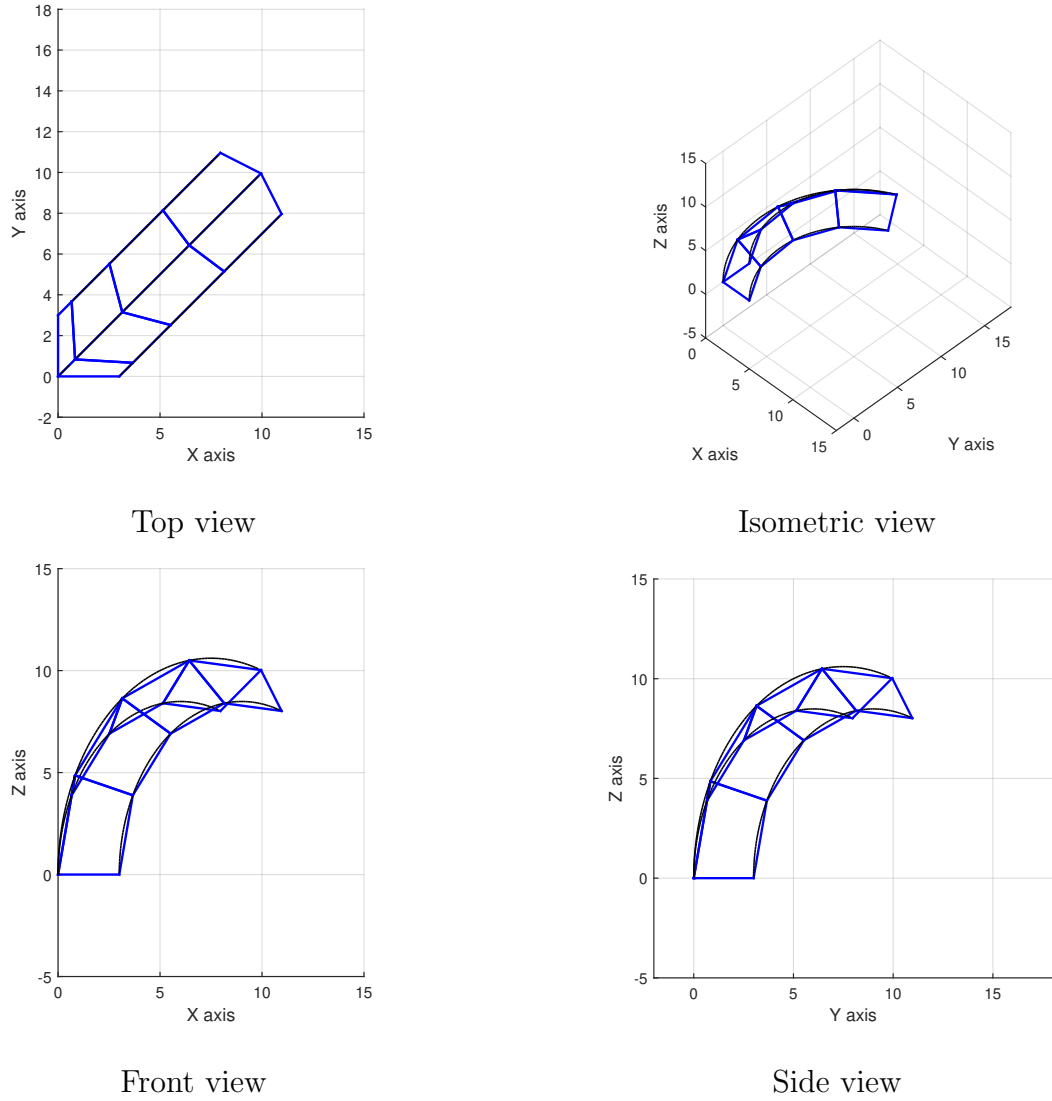
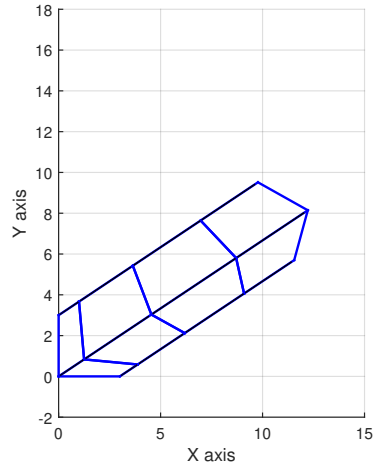
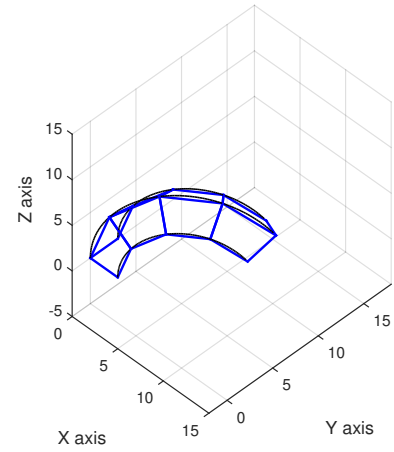


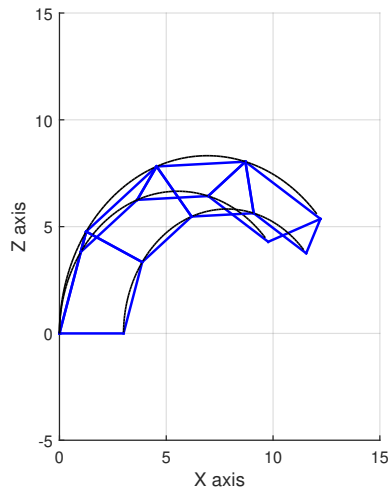
Figure 5.9: Profile of robot with cables actuated by equal displacements. (Black lines for analytical solution and blue lines for optimization based solution)



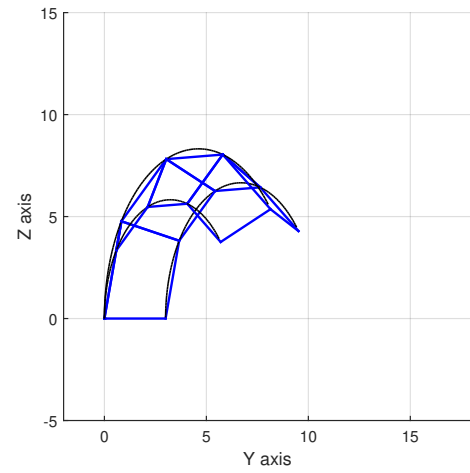
Top view



Isometric view



Front view



Side view

Figure 5.10: Profile of robot with cables actuated by different displacements. (Black lines for analytical solution and blue lines for optimization based solution)

same would translate to adding specific constraints to the problem, such as:

$$\begin{aligned}
 \|\mathbf{x}_0^{i+1} - \mathbf{x}_a^{i+1}\|_j &= a_j \\
 \|\mathbf{x}_0^{i+1} - \mathbf{x}_b^{i+1}\|_j &= a_j \\
 \left\{ \arccos \left(\left(\frac{\mathbf{x}_0^i - \mathbf{x}_a^i}{\|\mathbf{x}_0^i - \mathbf{x}_a^i\|} \right) \cdot \left(\frac{\mathbf{x}_0^i - \mathbf{x}_b^i}{\|\mathbf{x}_0^i - \mathbf{x}_b^i\|} \right) \right) \right\}_j &= \phi_j
 \end{aligned} \tag{5.11}$$

where $(\cdot)_j$ represent the specified values at segment index j . The above optimization problem can again be solved numerically using the function `fmincon` provided by MATLAB.

Inverse kinematics of continuum robot corresponds to finding the configuration of the robot— which is essentially determining the radius of curvature as well as the co-ordinates of the center of the arc formed by the backbone, given the position of the tip of the robot. For general tendon routing, this problem is non-trivial and dependent on the routing of the cables. For continuum robot with equally spaced tendons, this problem has been already addressed by Neppali et al. in reference [156].

5.3 Motion planning of endoscopic robot

This section discusses, the tractrix based motion planning of hyper-redundant endoscopic robot whose travel is confined to a duct. At first, the fundamentals of tractrix based motion planning is discussed. This is followed by three methods to represent 2-dimensional planar ducts along with the motion planning algorithm for each representation. The concept is extended to two methods of 3-D representations and the implementation strategy in the two cases are discussed. Finally, simulation results for an endoscopic robot travelling through GI tract is shown and a few limitations of the procedure is discussed.

5.3.1 Overview of tractrix based motion planning

Consider a rigid link of length L_0 positioned in a 2D plane, initially aligned to the Y-axis as shown in Fig. 5.11. The co-ordinates of the ‘head’ of the link is given as $\mathbf{X}_h = [X_h, Y_h]^T$ and the co-ordinates of the ‘tail’ as $\mathbf{X}_t = [X_t, Y_t]^T$. If the head is displaced to the co-ordinate $\mathbf{x}_h = [x_h, y_h]$ along the positive X – axis by t units, the tail of the link can lie anywhere on the circumference of a circle centered at the co-ordinate $(t, 0)$ with radius L_0 . If we assign a rule that the velocity of the tail of the link is always directed towards the length of the link, we get two diametrically opposite points on the circle. The continuous path traced by the tail point

is the well known tractrix curve as given in equation (5.12):

$$\mathbf{x}_t = [x(t), y(t)] = [t - L_0 \tanh \frac{t}{L_0}, L_0 \operatorname{sech} \frac{t}{L_0}] \quad (5.12)$$

The extension of tractrix equation along motion in arbitrary direction as well as an algorithm to calculate the same in 3-D can be found in [87]. In case of multiple links connected to each other as in the case of a hyper-redundant robot, or a one dimensional object approximated as a series of connected linkages, the algorithm can be applied iteratively from the head to tail as shown in their paper. By moving along the tractrix curve, the tail moves the minimum distance with respect to its initial position. Also, the displacement $\|\mathbf{x}_h - \mathbf{X}_h\| \geq \|\mathbf{x}_t - \mathbf{X}_t\|$ which means that the displacement attenuates from the displaced link to end of the chain in case of serially connected links as shown in Fig. 5.12. Due to the minimal displacement of the tail, the motion can be imagined as the one with high lateral resistance on the link and less resistance in the direction of motion of link.

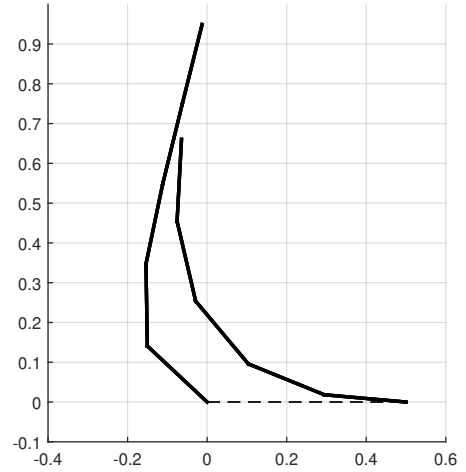
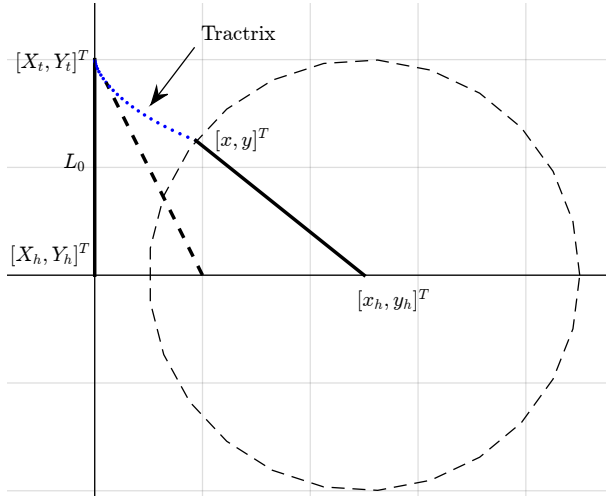


Figure 5.11: Tractrix curve in 2D with one link Figure 5.12: Tractrix with multiple links

It is shown in [88] that for a single rigid link, tractrix curve can also be obtained by minimizing an L^2 metric – the displacement of the tail from its initial position subject to the condition that the length of link is always preserved. So, the co-ordinates of the tail can be obtained from the following minimization problem:

$$\operatorname{argmin}_{\mathbf{x}_t} \|\mathbf{x}_t - \mathbf{X}_t\| \quad (5.13)$$

$$\text{Subject to: } \|\mathbf{x}_h - \mathbf{x}_t\| - L_0 = 0$$

An advantage of expressing tractrix as a minimization problem is that more constraints can be added to the above expression and hence, control the position of the tail point. Though the resulting curve may not necessarily be a tractrix curve, the motion of the tail will appear realistic¹. For the motion of a link which minimizes its tail velocity (displacement of the tail co-ordinates), obstacle avoidance is achieved by formulating the problem as:

$$\begin{aligned} & \underset{\mathbf{x}_t}{\operatorname{argmin}} \|\mathbf{x}_t - \mathbf{X}_t\| & (5.14) \\ \text{Subject to: } & \|\mathbf{x}_h - \mathbf{x}_t\| - L_0 = 0 \\ & f(\mathbf{x}) \succeq 0 \end{aligned}$$

where $\mathbf{f}(\mathbf{x}) = \mathbf{0}$ are the analytical equations of the boundaries of the surfaces which are to be avoided. For example, if the tail is to avoid a single obstacle represented by a circle with center (x_c, y_c) , the expression $f(x) = (x - x_c)^2 + (y - y_c)^2 - r^2 > 0$ ensures that the point x always lies outside the circle of radius r . Complex objects can be modelled as a combination of super-ellipses as shown in [89]. In this case, $\mathbf{f}(x)$ will be a vector of all boundary equations $\mathbf{f}(x) = [f_1(x), f_2(x), \dots, f_m(x)]^T$. It is also worth noting that the value of constraint function in equation (5.14) will increase or decrease as the point is farther from the curve $\mathbf{f}(x)$; the value being zero on the curve. Hence, this approach can also be imagined as a geometric potential field, with zero potential only at the surface of the obstacle.

The problem of planning the motion of the robot through a duct may be specified as:

$$\begin{aligned} & \underset{\mathbf{x}_t}{\operatorname{argmin}} \|\mathbf{x}_t - \mathbf{X}_t\| & (5.15) \\ \text{Subject to: } & \|\mathbf{x}_h - \mathbf{x}_t\| - L_0 = 0 \\ & C_{\text{ineq}} : f(x) < 0 \end{aligned}$$

While this expression is applicable for a duct represented by a single surface with the boundary $f(x)$, unlike the obstacle avoidance problem, the same will not work in the case of complex surfaces represented by combination of simpler analytical shapes. This is because if a point is classified as inside one of the simpler shapes, then it should be classified as outside the other shapes forming the duct. In other words, if one constraint function $f_k(x) < 0$, then the other constraint functions $f_{i \neq k} \geq 0$.

¹The tractrix based algorithm represents a physical system where the link moves in a highly viscous environment. A method to simulate motion in less viscous medium is given in Appendix C

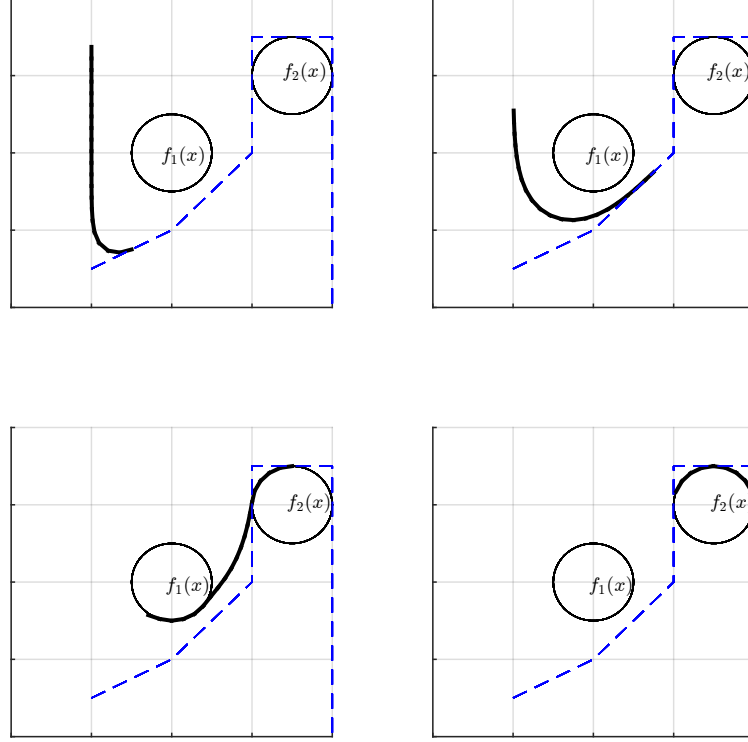


Figure 5.13: Obstacle avoidance in a plane

5.3.2 Motion planning through planar ducts

This section discusses different methods to represent a duct in 2D planar surface and how constraints can be added in different representations of duct so as to ensure that the the tip will always lie inside the duct during motion. Each method is shown to have its own advantages.

5.3.2.1 Representation of duct using super-ellipses

One method to represent a duct is by overlapping a series of super-ellipses as shown in Fig. 5.15. This is the most simple and straightforward means of representation as shown in [89]. In Cartesian co-ordinate system \mathbb{R}^2 , the contour of super-ellipse generates different shapes (see Fig. 5.14) using the following equation:

$$f(\mathbf{x}) = f(x, y) : \left| \frac{x - x_c}{a} \right|^n + \left| \frac{y - y_c}{b} \right|^n - 1 = 0 \quad (5.16)$$

The condition $f(\mathbf{x}_t) < 0$ will ensure that the co-ordinates of the tail of the link (x_t, y_t) always lie inside the bounding curve of a super-ellipse. However, in case of multiple equations

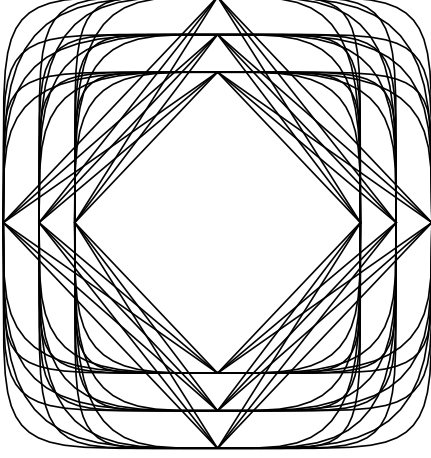
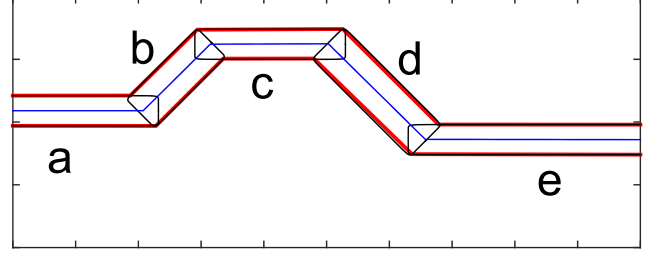


Figure 5.14: Super ellipses


 Figure 5.15: Duct modeled as a combination of super-ellipses **a** through **e** – red: outer boundary, blue: desired path of head

$(f_i(x), i = 1, 2, \dots, m)$, only one of them will be satisfied for the point to be inside the duct. In practical implementation, we can say that this translates to saying that the least value amongst all the values of $f_i(x)$ should be less than zero. For the i^{th} super-ellipse which is rotated by an angle ϕ_i about the z -axis and whose center is translated to the co-ordinates (x_i, y_i) so as to fit a portion of a duct, the co-ordinates of boundary should be multiplied with a transformation matrix

$$T_i = \begin{bmatrix} \cos \phi_i & -\sin \phi_i & 0 & x_i \\ \sin \phi_i & \cos \phi_i & 0 & y_i \\ 0 & 0 & 1 & 0 \\ 0 & 0 & 0 & 1 \end{bmatrix} \quad (5.17)$$

The constraint equation now becomes $g_i(\mathbf{x}_t) : f_i(T_i^T \mathbf{x}_t) < 0, i = 1, 2, \dots, m$. For practical implementation, we can write the inequality constraint as

$$C_{\text{ineq}} : \min(g_i(\mathbf{x}_t)) < 0, i = 1, 2, \dots, m \quad (5.18)$$

An example of single link and multi-segmented chain passing through the duct is shown in Fig. 5.16. Motion of a unit link with and without constraint is shown in Fig. 5.17. The negative gradient of the inequality constraint function is also shown in Fig. 5.17. The method shown here is quite fast and scalable, while the majority of time taken for the scheme is in identifying the super-ellipsoids which fit the duct profile, which is however, a pre-processing task. For the example shown in this section, this identification is done by manually selecting

clusters of points in the duct and fitting ellipses which will reduce the fitting error in a least squared sense.

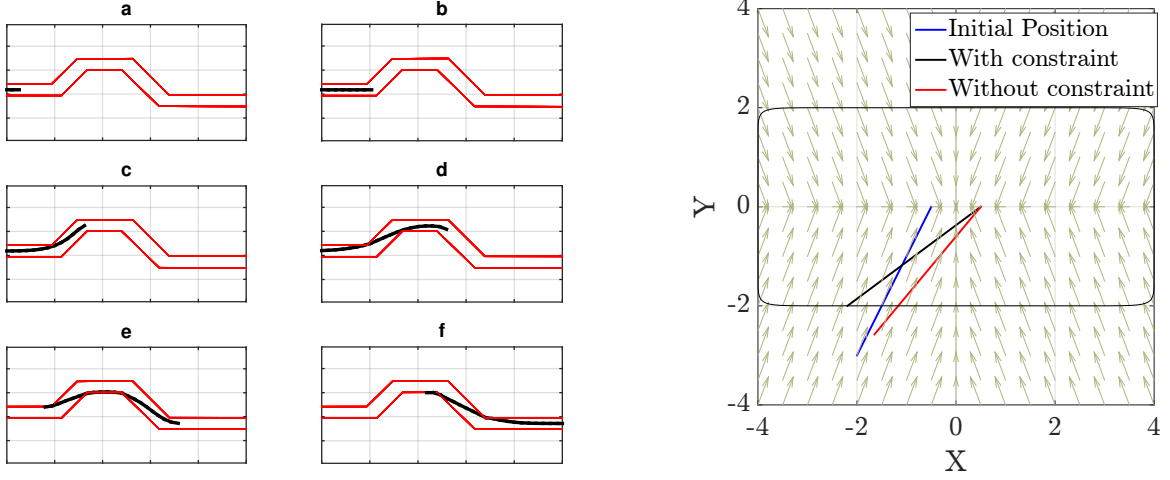


Figure 5.16: Motion through duct modelled as combination of super-ellipses Figure 5.17: Effect of gradient of inequality constraint in pulling the tail into the duct

5.3.2.2 Representation of duct as a set of connected quadrilaterals

Since the profile of a super-ellipse is always symmetric, for complex and non-symmetric ducts, representation using the previous method might require a large number of shapes. For such cases, a complex duct shape can be represented as a closed shape obtained by stitching convex quadrilaterals as shown in Fig. 5.18. The individual quadrilateral patches, denoted as A_1, A_2, \dots, A_n , are each bounded by the line segments defined by the points $(\mathbf{P}_0, \mathbf{P}_1), (\mathbf{P}_1, \mathbf{P}_2), \dots, (\mathbf{P}_{n-1}, \mathbf{P}_n)$ for the curve ζ_1 and $(\mathbf{Q}_0, \mathbf{Q}_1), (\mathbf{Q}_1, \mathbf{Q}_2), \dots, (\mathbf{Q}_{n-1}, \mathbf{Q}_n)$ for the curve ζ_2 . Classification of a point \mathbf{x}_t as inside or outside a quadrilateral represented by points, say, $\mathbf{P}_1, \mathbf{P}_2, \mathbf{Q}_2$ and \mathbf{Q}_1 , is essentially checking the placement of the point in the half spaces represented by the four lines spanned by the point set $(\mathbf{P}_1, \mathbf{P}_2), (\mathbf{P}_2, \mathbf{Q}_2), (\mathbf{Q}_2, \mathbf{Q}_1)$, and $(\mathbf{Q}_1, \mathbf{P}_1)$. This can be written as a set of four inequality constraints:

$$A_i^1 x_t + A_i^2 y_t + B_i < 0 \quad i = 1, 2, 3, 4 \quad (5.19)$$

where $A_i^1 x + A_i^2 y + B_i = 0$ represents a line obtained from one pair of non-diagonal points in the quadrilateral. In matrix form, the inequality will be:

$$C_{\text{ineq}} : [\mathbf{A}] \mathbf{x}_t + \mathbf{B} < 0 \quad (5.20)$$

where $[\mathbf{A}]$ is a 4×4 matrix and \mathbf{B} is a 4×1 vector.

A more convenient method for practical applications is as follows:

The co-ordinates of a point inside the surface patch A_i is given by the parametric expression

$$\mathbf{x}_i(u, v) = [\mathbf{P}_{i-1} + (1 - u) \mathbf{P}_i] (1 - v) + [\mathbf{Q}_{i-1} + (1 - u) \mathbf{Q}_i] (v) \quad (5.21)$$

in parameters u and v . If the vertices of the quadrilateral are given by $\mathbf{P}_i = [xP_i, yP_i]^T$ and $\mathbf{Q}_i = [xQ_i, yQ_i]^T$, then the analytical expressions for the terms u and v , given the value of \mathbf{x}_i , can be obtained by solving equation (5.21) (see Appendix A). The values of u, v can be used to classify the point with respect to the surface patch A_i ¹.

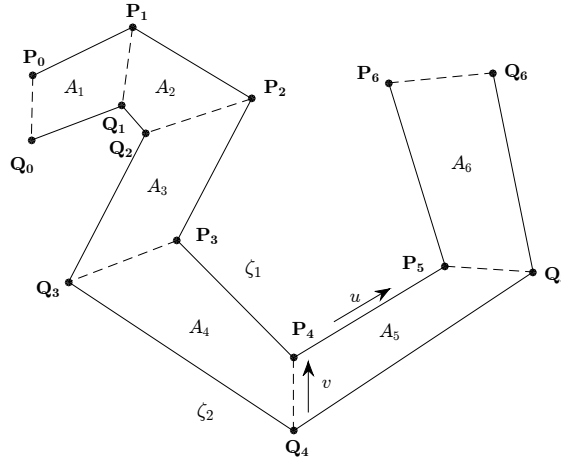


Figure 5.18: Duct represented by stitched quadrilaterals A_1 through A_6

In case of a single quadrilateral patch, the inequality constraints will be simply,

$$C_{\text{ineq}} : 0 \leq u \leq 1, \quad 0 < v < 1 \quad (5.22)$$

for real values of u and v . In case of multiple patches, classifying one point with respect to all the patches return the values $(u_1, v_1), (u_2, v_2), \dots, (u_m, v_m)$ etc. for the m number of patches A_1, A_2, \dots, A_m and consequently, m set of conditions. However, out of the m condition sets, only

¹It may be noted that there will be two sets of solution and they are not always real and unique. For example, the point $\mathbf{P} = (10, -5)$ when classified with respect to the area A given by the points $\mathbf{P}_1 = (0, 15), \mathbf{P}_2 = (10, 10), \mathbf{Q}_1 = (0, 0)$ and $\mathbf{Q}_2 = (4, 1)$, returns the values $u = (1.0 + 0.6i, 1.0 - 0.6i)$ and $v = (2.0 + 1.9i, 2.0 - 1.9i)$. However, it is easy to filter out the imaginary set of solutions, should the algorithm encounter the same.

one set should be satisfied since the point will belong to only one patch at a given instance of motion through the duct.

In order to provide a gradient to the constraint which will direct the point into the duct, an inequality constraint is to be included as in the case of super-ellipses described in the previous subsection. If \hat{u} and \hat{v} represent the parameters obtained for a point \mathbf{x}_t classified with respect to the quadrilateral A_i , $x_{\zeta_1}(t) = \mathbf{P}_{i-1} + (1 - \hat{u}) \mathbf{P}_i$ and $x_{\zeta_2}(t) = \mathbf{Q}_{i-1} + (1 - \hat{u}) \mathbf{Q}_i$ will give the two points on the duct boundary curves corresponding to the parameter \hat{u} . Then we can see that the quantity

$$h = \|\mathbf{x}_{\zeta_1} - \mathbf{x}_t\|^2 + \|\mathbf{x}_{\zeta_2} - \mathbf{x}_t\|^2 - \|\mathbf{x}_{\zeta_1} - \mathbf{x}_{\zeta_2}\|^2 \quad (5.23)$$

will always assign a negative real value for h when point is inside the duct and a positive real value when the point is outside the duct. The value will be zero only at the boundaries. Hence, for an array of quadrilaterals, it is only necessary that the minimum value of the vector $\mathbf{h} = [h_1, h_2, \dots, h_m]$ should be negative for classifying the point with respect to the duct, as in the case of previous section. It may be noted that the inequality only takes into account the parameter variation across the boundaries (along the parameter v) and not in the direction of u . To account for the same, we make use of the function χ which is necessarily a linear combination of two Heaviside step functions $H(0) - H(1)$, defined as:

$$\chi(t) = \begin{cases} 0, & t < 0 \\ 1, & 0 \leq t \leq 1 \\ 0, & t > 1 \end{cases} \quad (5.24)$$

The function χ applied on the quantity \hat{u}_i (which is the value of parameter u classified with respect to quadrilateral A_i), will return 0 only if the point satisfies the constraint $0 \leq \hat{u}_i \leq 1$. Now, multiplying this quantity $\chi(\hat{u})$ with h_i will return a non-zero negative value only if the point is inside the duct. Then the following inequality constraint:

$$C_{\text{ineq}} : [\chi(\hat{\mathbf{u}})]^T \mathbf{h} < 0 \quad (5.25)$$

where $\hat{\mathbf{u}} = [\hat{u}_1, \hat{u}_2, \dots, \hat{u}_m]^T$ becomes a more practical and convenient way to implement the inequality constraint in the optimization problem.

As an example, motion of a unit link passing through the duct and the effect of the added inequality constraint in equation (5.25) to pull the tail end of the link which is initially positioned

outside the duct, is shown in Fig. 5.20. Apart from being more flexible, another advantage of representing a 2D duct as a set of connected quadrilaterals in this parametric form is that by setting the limits of the parameter v to $0 + \delta < v < 1 - \delta$, $\delta < 0.5$, it is easy to manually add a clearance from the walls of the duct without manipulating the duct itself. Also, it is easy to note that $\delta = 0.5 - \epsilon$ (where ϵ is a small number) would follow the backbone curve motion.

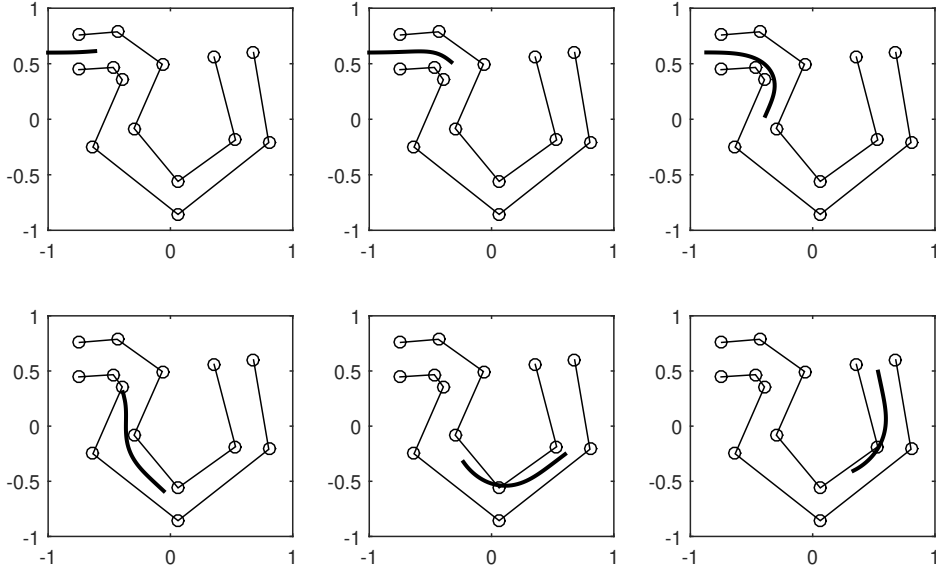


Figure 5.19: Example of constrained motion of a 40 link robot with stitched quadrilaterals

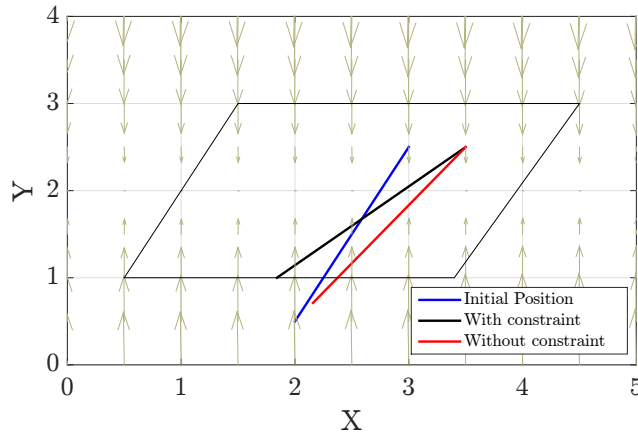


Figure 5.20: Effect of gradient of inequality constraint in pulling the tail into the quadrilateral duct

5.3.2.3 Representation of duct using two non-intersecting continuous curves

If the non-intersecting border curves of the duct can be analytically expressed, then the equation of the surface patch will simply be,

$$\mathbf{x}_i(u, v) = \zeta_1(u) (1 - v) + \zeta_2(u) (v) \quad (5.26)$$

For example, Fig. 5.21 shows a 2D duct defined by two curves $\zeta_1(u) = [u, \sin(u)]^T$ and $\zeta_2(u) = [u, \sin(u + \frac{\pi}{8}) + 1]^T$ and a path chosen midway between the two curves. The equation of the surface generated by these curves will be

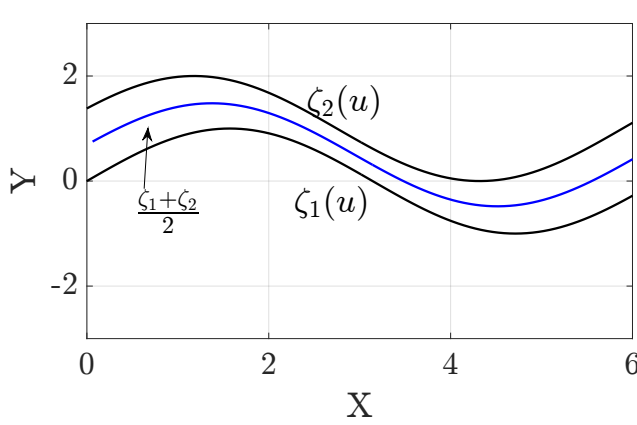


Figure 5.21: Example of analytical duct

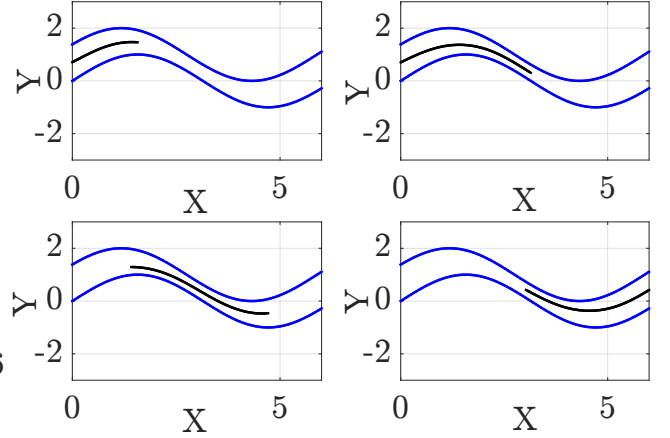


Figure 5.22: Motion through analytical duct

$$\begin{bmatrix} x(u, v) \\ y(u, v) \end{bmatrix} = \begin{bmatrix} u \\ \sin(u) + [\sin(u + \frac{\pi}{8}) - \sin(u) + 1] v \end{bmatrix} \quad (5.27)$$

which has the analytical solution for u and v :

$$u = x$$

$$v = \frac{y - \sin(x)}{\sin(x + \frac{\pi}{8}) - \sin(x) + 1}$$

In this case, we will solve the equations:

$$\begin{aligned} & \min_{\mathbf{x}_t} \|\mathbf{x}_t - \mathbf{X}_t\| \\ \text{sub: } & \|\mathbf{x}_h - \mathbf{x}_t\| - L_0 = 0 \end{aligned} \quad (5.28)$$

$$0 < v|_{\mathbf{x}_t} < 1 \quad (5.29)$$

An example movement of hyper-redundant manipulator through the duct is shown in Fig. 5.22. However, analytical solution is not always viable for complex equations and numerical procedure must be employed to find the values of u and v corresponding to the given tail point to be classified. Also, since multiple solutions may be possible for such cases, the correctness of the solution would heavily depend on the choice of initial guess provided¹.

5.3.3 Motion planning through 3D ducts

In this section, three methods to represent ducts in 3D and how the optimization problem can be framed for each representations is detailed.

5.3.3.1 Representation of duct as a combination of super-ellipsoids

Representation of ducts in 2D can be extended to 3D by using super-ellipsoids. In a Cartesian co-ordinate system, the surface of a super-ellipsoid follows the equation:

$$f(x, y, z) : \left[\left\{ \left(\frac{x}{a} \right)^{\frac{2}{e}} + \left(\frac{y}{b} \right)^{\frac{2}{e}} \right\}^{\frac{e}{n}} + \left(\frac{z}{c} \right)^{\frac{2}{n}} \right]^{\frac{n}{2}} - 1 = 0 \quad (5.30)$$

By changing the parameters a , b , c and n , we get different closed surfaces as shown in Fig. 5.23 and by combining different super-ellipsoid shapes, we can generate a 3D duct profile.

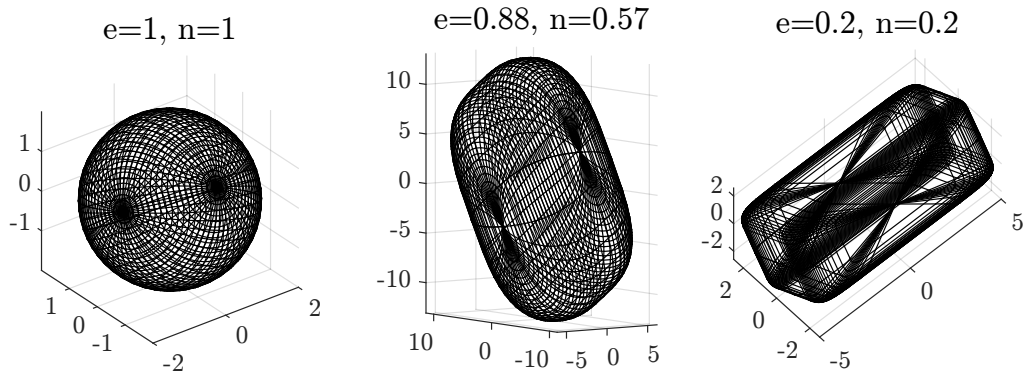


Figure 5.23: Super-ellipsoids

The procedure to calculate the inside-outside condition is same as that of the method described in section 5.3.2.1. The inequality condition will be equation (5.18). As mentioned in the case for super-ellipses, solution to the motion planning problem with ducts represented by

¹The same argument will also hold for analytical surfaces spanned in 3D and hence is not studied further.

super-ellipsoids is fast. Identifying the shapes which fit the duct, is also same as the method mentioned in section 5.3.2.1.

5.3.3.2 Representation of duct as a set of connected cylinders

Similar to the set of connected quadrilaterals in 2D, a duct in 3D can be represented by series of connected cylinders. By linearly interpolating two circles in space, we get the parametric equation of the cylinder as given in equation (5.31) below (see Appendix B for the expanded form of equation (5.31).)

$$x = C_1(u, t, \theta), \quad y = C_2(u, t, \theta), \quad z = C_3(u, t, \theta) \quad (5.31)$$

where the parameters u , t and θ varies along the radial, axial and circumferential direction of the cylinder respectively (see Fig. B.1). Similar to the representation in section 5.3.2.2, $0 \leq u < 1$ and $0 < t < 1$ classifies the point as inside the cylinder. The constrained inequality (5.25) generated will also be valid for cylinders. The quantity h_i is given as $h_i = \hat{u}_i - 1$ which shows the same characteristics as defined by the value of h_i in equation (5.23). The constraint inequality, hence takes the form:

$$C_{\text{ineq}} : [\chi(\hat{\mathbf{t}})]^T \mathbf{h} < 0 \quad (5.32)$$

As is the case of quadrilaterals, it is possible to add a clearance from the walls by changing the radius of cylinder from r to $r - \delta$, which is a very desirable characteristic for robots used in medical applications.

5.3.3.3 Representation of duct using point clouds

The most direct way of representing the duct would be as a point cloud as obtained from measurements or a depth map. Subsequently, it would be possible to process the raw data (by using alpha shapes [157] and standard Delaunay triangulation algorithms [158]) to obtain the geometric representation of the cloud of points as a convex polyhedron. Stereo-lithographic formatted file (STL) is a standard data structure, which has been used in the current work. Using the current framework, it is possible to pose the motion planning problem in the following form:

$$\begin{aligned} & \min_{\mathbf{x}_t} \|\mathbf{x}_t - \mathbf{X}_t\| & (5.33) \\ \text{subject to: } & \|\mathbf{x}_h - \mathbf{x}_t\| - L_0 = 0 \\ & [\mathbf{A}]\mathbf{x}_t + \mathbf{B} \leq 0 \end{aligned}$$

where \mathbf{A} is a $m \times 3$ matrix and \mathbf{B} is a $m \times 1$ vector. The left-hand side of m inequalities represent the equations of m number of planes spanned by three points on each triangular facet of convex polyhedron. The i^{th} equation, $A_i^1 x_t + A_i^2 y_t + A_i^3 z_t + B_i$ takes a value less than zero when the point \mathbf{x}_t is in the half space which contains the origin and is greater than zero otherwise. The value also provides the attractive gradient which will ensure that the point stays inside the duct. However, in actual implementation, this procedure will be tedious and for practical convenience, it is possible to classify the point \mathbf{x}_t as inside or outside the hull using the MATLAB function `inhull.m`, made available by John D'Errico for free usage. The attracting gradient which ensures the point to be inside the duct—as was the case with the previous methods—can be provided using the artificial potential field generated from the centroid of the point cloud in conjunction with the output of the in-out function. The inequality constraint then becomes

$$w(\mathbf{x}_t) \frac{1}{\|(\bar{\mathbf{R}}) - \mathbf{x}_t\|} \leq 0 \quad (5.34)$$

where $w(\mathbf{x}_t)$ represents the output from in-out function which is either 1 for the point being outside and 0 for the point being inside the cloud or on the bounding surface¹. Representations of a pipe using ellipsoids, analytical cylinders and as convex point clouds are shown in Fig. 5.24, Fig. 5.25 and Fig. 5.26.

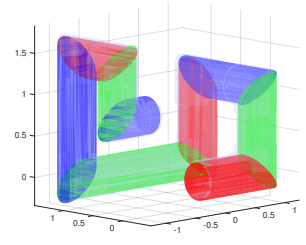
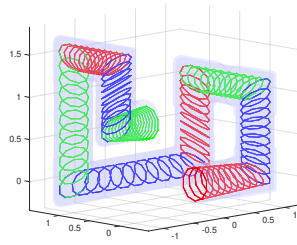
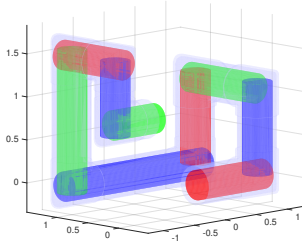


Figure 5.24: Fitted ellipsoids Figure 5.25: Fitted cylinders Figure 5.26: Point clouds

5.3.4 Simulation of motion through GI tract

In this section, the natural motion of a hyper-redundant endoscopic robot through a GI tract is simulated. For simulation, the stereo-lithographic data of GI tract obtained by processing CT scan data obtained from Visible Human Dataset [159] is used. For demonstration, both the methods presented in section 5.3.3.1 and section 5.3.3.2 are used for approximating the GI tract. In the first method, a collection of points are manually selected from the STL file where

¹Unlike the previous classification problems, the bounding surface will also be considered as inside the surface in this case.

super-ellipsoids are fit based on least square error minimization techniques. Representation of GI tract as series of super-ellipsoids is shown in Fig. 5.27.

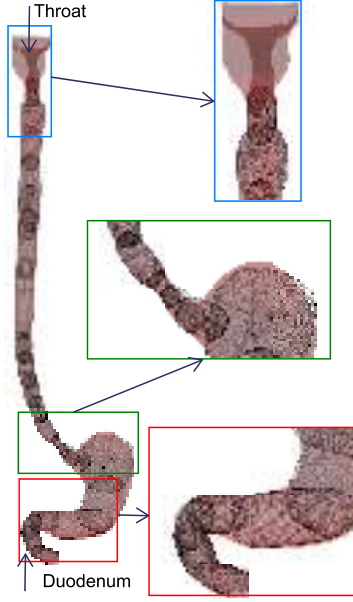


Figure 5.27: GI tract as collection of super-ellipsoids

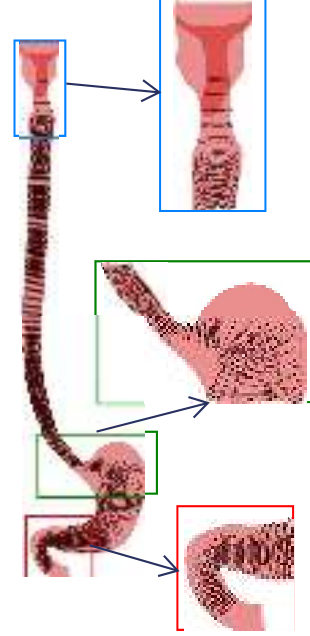


Figure 5.28: GI tract with connected cylinders

For representing GI tract as cylinders, firstly, the medial axis of the duct is found out following Cao et al. [160]. Then at equal intervals of distance along the medial axis, planes are drawn normal to the same. The collection of points which are in the close proximity of the plane are selected and a circle is fitted on the points using least square error minimization. The parameters so obtained are used for the cylinder equations in (5.31). Representation of GI tract as a series of connected cylinders is shown in Fig. 5.28. The algorithms are implemented in MATLAB and the results are rendered using Blender [161]. The realistic motion simulation of an endoscope through GI tract is shown in Fig. 5.29.

5.3.5 Limitations of the tractrix based scheme

In spite of the definite advantages regarding formulation and computational aspects of the tractrix based motion planning approach, there are a few limitations which are of importance. The ducts represented by analytical curves and cylinders involve numerically solving non-linear or transcendental equations to calculate the parameters which could be computationally expensive for bad choice of initial guesses.

It can be seen that a given hyper-redundant robot with a particular link length will not be able to negotiate a path with a “very high” curvature. This is shown in Fig. 5.30. In the figure,



Figure 5.29: Motion of endoscope through GI tract

the points 1,2,...,8 denote the coordinates of \mathbf{x}_h across successive iterations. From iteration 6 onwards, the constraints demarcating the feasible space \mathcal{S} and the one guaranteeing a constant link length cannot be simultaneously satisfied unless the tail \mathbf{x}_t (the result of equation (5.13)), backtracks its own path. Soon after, the optimization problem stops as the link seems to be “locked” at the trough of $\zeta(u)$ ¹. This locking effect can be qualitatively quantified using the concept of “traversability” from literature on wheeled mobile robots (see for example, [162]). A curve $\zeta(u)$ is traversable by a circle C_i , $C_i : \begin{pmatrix} R_i \cos(v) \\ R_i \sin(v) \end{pmatrix}$, $0 \leq v \leq 2\pi$ if C_i can roll over the curve $\zeta(u)$ while maintaining “only one” point of contact at all times. Traversability for planar curves can be described by the relative curvature κ_R of the circle and the curve at the point of contact. For a planar curve and a circle of radius R_i , the relative curvature can be given as

$$\kappa_R = \frac{\zeta_{uu}}{(1 + \zeta_u^2)^{3/2}} - \frac{1}{R_i}$$

A curve is traversable if the relative curvature is greater than 0, just traversable if it is equal to zero and not traversable if it is negative. This can be visualized from Fig. 5.31. This concept would generalize to traversable surfaces when the minimum of the two eigenvalues of the relative curvature matrix² is positive for traversability or vice versa. Based on this result, it can be hypothesized that if curve is traversable by a circle of diameter D_i , then a hyper-redundant

¹The problem appears for backbone curve approach as well, and the solution which address the same comes with the cost of a very large displacement of the tail point.

²The relative curvature matrix of a parametric surface $S(u, v) : \mathbb{S}^2 \rightarrow \mathbb{R}^3$ and a sphere of radius R at the point of contact $P = S(u^*, v^*)$ and on the Gaussian frame attached to the sphere at P is given as: $\kappa_R|_P =$

robot of link length D_i can move below the curve without intersecting the curve as shown in Fig. 5.32. This would also give an idea about the largest link length that can be used in a hyper-redundant robot traversing a given duct.

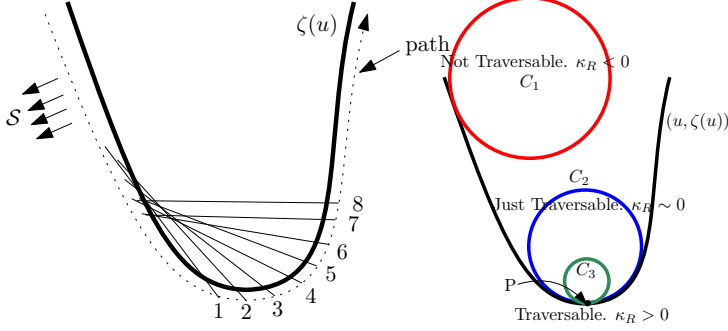


Figure 5.30: Infeasible link length

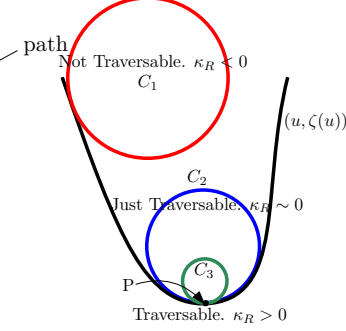


Figure 5.31: Traversability of a curve

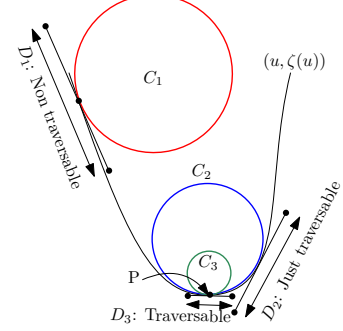


Figure 5.32: Feasible link lengths

5.4 Conclusions

The forward kinematics of cable driven continuum robots such as the well-known Rice/Clemson elephant trunk has been analytically solved by Gravagne and Walker based on differential geometry. It is shown in that the same can also be achieved using optimization methods. The continuum robot is discretized into segments with each segment represented as a 4-bar parallelogram linkage for planar manipulation. From the initial horizontal position of the coupler, a unique pose of the 4-bar linkage is obtained by minimizing the angle made by coupler with the fixed link, while maintaining the constraints of link lengths. When the iterative process is continued for the entire robot, the resulting pose is shown to be the same as the one derived using the traditional differential geometric methods. A minimum number of segments required for the procedure is also suggested based on the derivation and the method shows consistency with varying number of segments. The concept is directly extended to 3D using a 7-bar linkage or two adjoined 4-bar linkages and with an extra constraint to maintain the constant angle between the cables. The numerical procedure and analytical solution are shown to match each other as in the 2D case. The method suggested in this chapter suggests a new perspective in modelling the forward kinematics of cable driven continuum robots. The proposed method is easy to apply to robots having uneven separation between the cables and also for robots with generalized cable routing— for which analytical methods could be a daunting task.

$$\begin{bmatrix} S_{uu} \cdot \mathbf{N} - 1/R & S_{uv} \cdot \mathbf{N} \\ S_{uv} \cdot \mathbf{N} & S_{vv} \cdot \mathbf{N} - 1/R \end{bmatrix}_{(u=u^*, v=v^*)} \quad \text{where } \mathbf{N} \text{ is the normal vector.}$$

Motion planning for hyper-redundant robots in narrow ducts using tractrix based redundancy resolution scheme is addressed. To this end, three methods to represent ducts in 2D plane as a combination of ellipses, as a series of connected quadrilaterals as well as a bound planar surface formed from two non-intersecting analytical curves are discussed. Methods to formulate inequality constraints which will impose the tail point of a link to always lie inside the duct are investigated for all the cases. In 3D, representations of ducts as series of ellipsoids and as a series of connected cylinders are discussed. The basic formulation as well as formulation for efficient practical implementation are discussed. The motion planning strategy is validated by simulating the motion of endoscopic hyper-redundant robot traversing a GI tract and is shown that the methods discussed can be effectively used in motion planning of a hyper-redundant robot while emulating realism.

Chapter 6

Conclusions and Future work

6.1 Summary

Due to the innovative concepts in catheter design and minimal invasive nature of procedures conducted using endoscopes, endoscopy has become an indispensable solution for many medical treatments and diagnosis. The two problems faced during endoscopy which are the independent motion of catheter with respect to the camera as well as maneuvering the scope through the tract while maintaining the safety of patients are still largely unaddressed by modern day endoscopes. An endoscope design which takes care of these issues can reduce the overall time required for the procedure and thereby reducing the patient's discomfort. The thesis prescribes solutions to addressing these problems using a flexible end-effector for actuating the catheter tip independent of the camera and using a hyper-redundant endoscopic robot which can be controlled to travel through the GI tract without colliding the walls of the duct.

Pneumatic artificial muscles are found to be a very good choice for actuating the end-effector due to its inherent compliance, lightness and high power-to-weight ratio. In order to apply the muscles in end-effector and to analyse the kinematics of end-effector, the pressure-deformation characteristics of MPAMs should be well understood. A literature survey on the static pressure-deformation characteristics of PAMs is studied. Due to the non-trivial nature of the physical interaction between the tube and the braiding of a PAM, many attempts were made in the literature to quantify the same as accurately as possible. From an implementation point of view, many empirical models have also been researched. In chapter 2 of this thesis, various attempts made by the researchers in this field have been consolidated. It is possible to selectively choose one of these models, or combine relevant aspects of different models based on the application in hand, and to this end, the chapter would serve as a guide for upcoming and continuing researchers and engineers.

In chapter 3, fabrication and characterization of a miniaturized PAM is discussed in detail. Miniaturized versions of pneumatic artificial muscles (MPAMs) with diameters 1.2 mm and 1.6 mm with lengths ranging from 40 to 70 mm are successfully fabricated and tested. From the literature survey, it has been observed that not many research emphasis has been made to describe the physics of miniaturized versions of PAMs due to the added complexity of the same and also due to the difficulty in experimentation. It is also seen from preliminary characterization experiments that the models available for PAMs do not conform experimentally with the results obtained for the fabricated MPAMs. To address this gap in the literature, and also to develop a consistent model which can be employed in the end-effector, a new mathematical model for miniaturized PAMs have been developed. The modelling strategy is different from the conventional methods and is shown to be consistent with the changes in the initial parameters of MPAM such as length, thickness as well as the initial braiding angle with error less than 7%. While the model under-predicts the stiffness of pressurized MPAM, this is identified as due to the limitation in the model in addressing the stretching of conical end-section due to the applied force. A correction applied to the end-section length proportional to the applied force showed better conformation with the experimental results. The model also predicts the theoretical limiting angle of 54.7° .

Chapter 4 shows the design, fabrication and testing of a flexible end-effector which make use of miniaturized PAMs. The fabricated end-effector prototype, is 55 mm long and has a diameter of 9 mm. The prototype was able to deflect a catheter tip by about 20 mm at the highest set pressure, which is more than the value required for practical purposes. The design stands out from similar designs for continuum actuators due to its absence of guiding discs to route the MPAMs. Due to the absence of guiding discs, the kinematic analysis for similar continuum designs—which are already available in the literature—could not be directly applied. Hence, a new forward kinematics model for the end-effector is proposed and validated experimentally. The new model takes input from the pressure-deformation model and uses an iterative method to solve the forward kinematics. The method predicts the actual pose of the end-effector with ± 2 mm error at the tip. An inverse kinematics formulation is proposed which takes input from the projected workspace of the end-effector. The theoretical prediction varies from experimental results by ~ 9 mm in deflection angle. Finally, a method to control the end-effector in real-time by integrating the workspace with the workspace of a thumbstick is proposed and demonstrated which demonstrates the feasibility of the designed end-effector in successful application on a clinical setting.

The second problem of maneuverability of the endoscope is addressed in chapter 5 of this thesis, by proposing the endoscope as a hyper-redundant continuum manipulator. Multi-segmented

cable driven continuum robot is identified to be the best suitor for this application due to its flexibility and potential for compact design. A different approach in modelling the forward kinematics of continuum robot has been developed and simulated. For 2D and 3D continuum manipulators with four cables routed at 90° apart, the derived numerical approach is shown to exactly match the theoretical results obtained from a differential geometric approach barring the errors from the numerical computation scheme. Since it is shown in the literature that unorthodox tendon routing for cables in continuum robots have definite advantages over the conventional routing, the derived formulation becomes more convenient and hence, quite promising method in solving the forward kinematics of cable driven robots. Once the kinematics of a single segment is fully understood, the endoscopic robot could be successfully used to maneuver through the GI tract while avoiding collision from the walls of the duct. To this end, chapter 5 of this thesis also propose tractrix based optimization strategy to resolve the redundancy and hence, to plan the motion of the robot to travel in confined spaces. Three different ways to represent a duct in 2D as well as 3D are shown. Formulations to implement confined-space motion in each of these cases are discussed in detail. Finally, the motion of an endoscope robot passing through a GI tract profile obtained from a human CT scan data is simulated to demonstrate and validate the concepts.

6.2 Scope for future work

The designs and methodologies discussed in this thesis have the following scopes for improvement:

1. As mentioned in chapter 3, the derived mathematical formulation does not quantify the end-tapering and the value is at present, experimentally determined. By considering the non-linear elastic nature of the silicone tube, and from the clamped end-conditions, the end-point curvature of the silicone tube at the inflated state could be calculated. This value of curvature could prove to be a crucial identifier in quantifying the end-tapering of the MPAM.
2. The end-effector is in preliminary stages of development and has scope of improvement in terms of developing faster implementation schemes and model based control systems. More work is required before the independently actuated end-effector can be employed in a clinical setting. The endoscopic tip with the preformed camera assembly and the spring loaded cap has to be fabricated and analysed. Integration of the catheter to reduce the overall dimensions of the end-effector is yet to be carried out.

3. Since it is possible to generate different spatial configurations for a continuum robot through general tendon routing, it may be possible to construct endoscopic robot which adheres to the profile of the GI tract, in which case, the actuation will be minimal. More work has to be done in this regard which may be accompanied with experimental demonstrations.
4. By including an artificial potential in the direction of motion which considers the curvature of the traversed path, it may be possible to negotiate sharp corners and avoid the locking effect of hyper-redundant manipulators.

Appendix

A Analytical expressions for u, v for quadrilateral patch

$$v = \frac{k_1 - k_2 \pm \sqrt{(k_2 - k_1)^2 - 4k_3k_4}}{2k_3}, \quad u = \frac{(x - {}^xP_{i-1} + v)}{(a_2 + va_3)} \quad (6.1)$$

where, $k_1 = (b_1b_2 + b_0b_3)$, $k_2 = (a_1a_2 + a_0a_3)$, $k_3 = (a_1a_3 - b_1b_3)$, $k_4 = (a_0a_2 - b_0b_2)$

$$a_0 = y - {}^yP_{i-1}, \quad a_1 = {}^yP_{i-1} - {}^yP_i, \quad a_2 = {}^xQ_{i-1} - {}^xP_{i-1}, \quad a_3 = ({}^xQ_i - {}^xP_i) - ({}^xQ_{i-1} - {}^xP_{i-1})$$

$$b_0 = x - {}^xP_{i-1}, \quad b_1 = {}^xP_{i-1} - {}^xP_i, \quad b_2 = {}^yQ_{i-1} - {}^yP_{i-1}, \quad b_3 = ({}^yQ_i - {}^yP_i) - ({}^yQ_{i-1} - {}^yP_{i-1})$$

If ${}^xP_{i-1} = {}^xP_i$ and ${}^xQ_{i-1} = {}^xQ_i$,

$$u = \frac{b_0}{a_2}, \quad v = \frac{a_0a_2 - (a_3 + a_2)}{a_1(b_0 - a_2) + b_0(b_3 - b_2)} \quad (6.2)$$

B Parametric equation of solid cylinder

The parametric cylinder, as shown in figure B.1, with the parameters u , θ and t is given as:

$$x = C_1(u, t, \theta) = (r_1m_1u \cos \theta + m_2)(1 - t) + (r_2n_1u \cos \theta + n_2)t \quad (6.3)$$

$$y = C_2(u, t, \theta) = (r_1m_3u \cos \theta + r_1m_4u \sin \theta + m_5)(1 - t) + (r_2n_3u \cos \theta + r_2n_4u \sin \theta + n_5)t \quad (6.4)$$

$$z = C_3(u, t, \theta) = (r_1m_6u \cos \theta + r_1m_7u \sin \theta + m_8)(1 - t) + (r_2n_6u \cos \theta + r_2n_7u \sin \theta + n_8)t \quad (6.5)$$

where

$$\begin{aligned} m_1 &= \cos^1\phi_2, \quad m_2 = {}^1x_c, & m_3 &= \sin^1\phi_1 \sin^1\phi_2, \quad m_4 = \cos^1\phi_1, \\ m_5 &= {}^1y_c, \quad m_6 = -\cos^1\phi_1 \sin^1\phi_2, & m_7 &= \sin^1\phi_1, \quad m_8 = {}^1z_c \end{aligned}$$

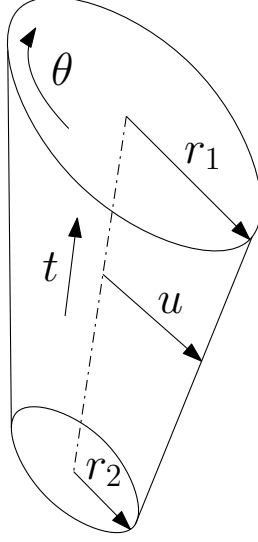


Figure B.1: Parameters of a general cylinder

$$\begin{aligned}
 n_1 &= \cos^2 \phi_2, \quad n_2 = {}^2x_c, & n_3 &= \sin^2 \phi_1 \sin^2 \phi_2, \quad n_4 = \cos^2 \phi_1, \\
 n_5 &= {}^2y_c, \quad n_6 = -\cos^2 \phi_1 \sin^2 \phi_2, & n_7 &= \sin^2 \phi_1, \quad n_8 = {}^2z_c
 \end{aligned}$$

The quantity ${}^1(\cdot)$ and ${}^2(\cdot)$ represent the corresponding parameters of the circles at the ends of the cylinder. ϕ_1 and ϕ_2 are the angles about the Y and X-axes which the plane of the circle is rotated, (x_c, y_c, z_c) is the co-ordinate of the center of the circle.

C Tractrix emulates natural motion

Motion simulated using the approach discussed in this paper imparts realism due to the minimal movement of tail with respect to the head. In nature this effect is created due to the friction or other resistive forces acting in the lateral direction of the link. In the absence of friction, displacement given in the head will result in a simple translation of link. In other words, \mathbf{x}_t in this case, will be same as \mathbf{x}_h . In actual practice, there will be a discrepancy between natural movement and the simulation based on the tractrix approach because tractrix represents the ideal scenario with motion of tail limited only in the direction of motion of the link due to very high friction while in natural motion, there is always some degree of translation possible. This slippage could be included in the formulation, however, by adding a slip vector to the tail displacement. Since the slippage amounts to the translation of link in the direction of link, slip vector will be in the direction of head displacement and can be written as $\mathbf{s} = \nu \mathbf{X}_h$, where $\nu < 1$ is a constant. Ideal tractrix case with friction is obtained by setting $\nu = 0$ and $\nu = 1$ represents pure translation of the link. Including this vector, the minimization function may

be written as:

$$\min_{\mathbf{x}_t} \|\mathbf{x}_t - (\mathbf{X}_t + \nu \mathbf{X}_h)\| \quad (6.6)$$

Fig. C.2 and Fig. C.3 show the final pose of a bicycle chain pulled from an initial horizontal position along the negative Y-axis on two surfaces: a smooth paper and a rough surface paved with gravel. Using a constant value of $\nu = 0.95$ for paper and $\nu = 0.86$ for gravel, we can see from the figures that the results from the formulation closely resemble the actual pose.

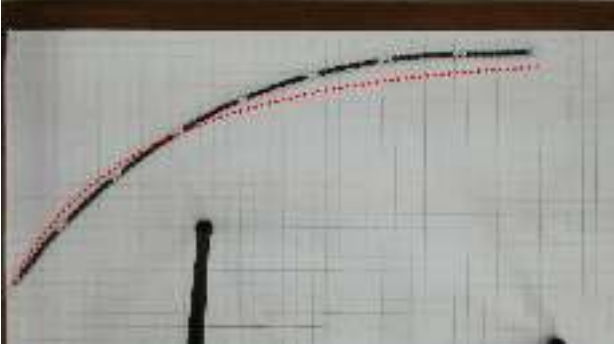


Figure C.2: Tractrix emulating the motion of a bicycle chain on photo paper, $\nu = 0.95$

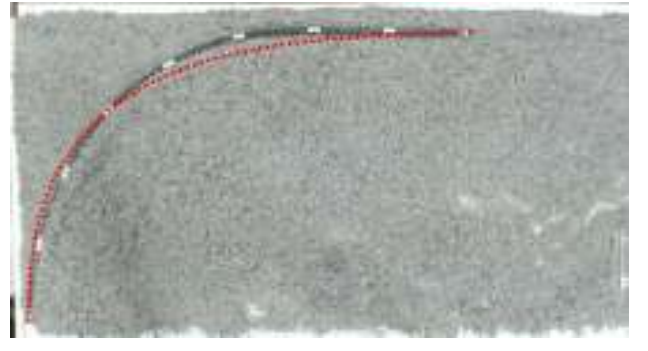


Figure C.3: Tractrix emulating the motion of a bicycle chain on gravel, $\nu = 0.86$

Bibliography

- [1] S. J. Spaner and G. L. Warnock, “A brief history of endoscopy, laparoscopy, and laparoscopic surgery”, *Journal of Laparoendoscopic & Advanced Surgical Techniques*, vol. 7, no. 6, pp. 369–373, 1997 (cit. on p. 1).
- [2] R. H. Hunt, “A brief history of endoscopy”, *Gastroenterology*, vol. 121, no. 3, pp. 738–739, 2001 (cit. on p. 1).
- [3] R. B. Bush, H. Leonhardt, I. M. Bush, and R. R. Landes, “Dr. Bozzini’s Lichtleiter: A translation of his original article (1806)”, *Urology*, vol. 3, no. 1, pp. 119–123, 1974 (cit. on p. 2).
- [4] S. K. Lo, L. L. Fujii-Lau, B. K. Enestvedt, J. H. Hwang, V. Konda, M. A. Manfredi, J. T. Maple, F. M. Murad, R. Pannala, K. L. Woods, *et al.*, “The use of carbon dioxide in gastrointestinal endoscopy”, *Gastrointestinal Endoscopy*, vol. 83, no. 5, pp. 857–865, 2016 (cit. on p. 2).
- [5] Olympus, *Olympus America*, medical.olympusamerica.com, Accessed: 2018-07-08 (cit. on p. 3).
- [6] Ethicon US, LLC, *Ethicon US, LLC*, www.ethicon.com, Accessed: 2018-07-08 (cit. on p. 4).
- [7] Barxx, *Barxx, St. Petersburg, FL. 33743-0271*, www.barxx.com, Accessed: 2018-07-08 (cit. on p. 4).
- [8] Pentax Medical, *Akishima-shi, Tokyo, 196-0012, Japan*, www.pentaxmedical.com, Accessed: 2018-07-08 (cit. on p. 4).
- [9] S. P. Gibb, J. S. Laney, and A. M. Tarshis, “Use of fiberoptic endoscopy in diagnosis and therapy of upper gastrointestinal disorders.”, *The Medical Clinics of North America*, vol. 70, no. 6, pp. 1307–1324, 1986 (cit. on pp. 3, 4).
- [10] V. Kumbhari and M. A. Khashab, “Perforation due to ERCP”, *Techniques in Gastrointestinal Endoscopy*, vol. 16, no. 4, pp. 187–194, 2014 (cit. on p. 4).

- [11] Y. Torii, *Bending part of endoscope*, US Patent 6,641,528, 2003 (cit. on p. 5).
- [12] E. A. Arkenbout, P. W. Henselmans, F. Jelínek, and P. Breedveld, “A state of the art review and categorization of multi-branched instruments for NOTES and SILS”, *Surgical Endoscopy*, vol. 29, no. 6, pp. 1281–1296, 2015 (cit. on p. 5).
- [13] A. Bajo and N. Simaan, “Hybrid motion/force control of multi-backbone continuum robots”, *The International Journal of Robotics Research*, vol. 35, no. 4, pp. 422–434, 2016 (cit. on p. 5).
- [14] K. Ikuta, M. Nokata, and S. Aritomi, “Biomedical micro robots driven by miniature cybernetic actuator”, in *Proceedings of the IEEE Workshop on Micro Electro Mechanical Systems, 1994, MEMS’94*, IEEE, 1994, pp. 263–268 (cit. on p. 5).
- [15] K. Xu, R. E. Goldman, J. Ding, P. K. Allen, D. L. Fowler, and N. Simaan, “System design of an insertable robotic effector platform for single port access (SPA) surgery”, in *IEEE/RSJ International Conference on Intelligent Robots and Systems, IROS 2009.*, IEEE, 2009, pp. 5546–5552 (cit. on p. 5).
- [16] J. Szewczyk, V De Sars, P. Bidaud, and G Dumont, “An active tubular polyarticulated micro-system for flexible endoscope”, *Experimental Robotics VII*, pp. 179–188, 2001 (cit. on p. 5).
- [17] S. Kim, C. Laschi, and B. Trimmer, “Soft robotics: A bioinspired evolution in robotics”, *Trends in Biotechnology*, vol. 31, no. 5, pp. 287–294, 2013 (cit. on p. 5).
- [18] C. Laschi, B. Mazzolai, and M. Cianchetti, “Soft robotics: Technologies and systems pushing the boundaries of robot abilities”, *Science Robotics*, vol. 1, no. 1, eaah3690, 2016 (cit. on p. 5).
- [19] D. Trivedi, C. D. Rahn, W. M. Kier, and I. D. Walker, “Soft robotics: Biological inspiration, state of the art, and future research”, *Applied Bionics and Biomechanics*, vol. 5, no. 3, pp. 99–117, 2008 (cit. on p. 5).
- [20] L. Wang, S. G. Nurzaman, F. Iida, *et al.*, “Soft-material robotics”, *Foundations and Trends in Robotics*, vol. 5, no. 3, pp. 191–259, 2017 (cit. on p. 5).
- [21] A. D. Marchese, R. K. Katzschmann, and D. Rus, “A recipe for soft fluidic elastomer robots”, *Soft Robotics*, vol. 2, no. 1, pp. 7–25, 2015 (cit. on p. 5).
- [22] R. H. Gaylord, *Fluid actuated motor system and stroking device*, US Patent 2,844,126, 1958 (cit. on pp. 5, 16, 33).
- [23] L. Joseph, “Artificial muscle”, *Life*, vol. 14, pp. 87–88, 1960 (cit. on p. 5).

- [24] J. E. Takosoglu, P. A. Laski, S. Blasiak, G. Bracha, and D. Pietrala, “Determining the static characteristics of pneumatic muscles”, *Measurement and Control*, vol. 49, no. 2, pp. 62–71, 2016 (cit. on pp. 6, 27).
- [25] T. E. Pillsbury, C. S. Kothera, and N. M. Wereley, “Effect of bladder wall thickness on miniature pneumatic artificial muscle performance”, *Bioinspiration & Biomimetics*, vol. 10, no. 5, p. 055 006, 2015 (cit. on pp. 6, 27, 33).
- [26] Festo Fluidic Muscle, *Festo Didactic Inc., 607 Industrial Way West, Eatontown NJ 07724*, www.festo.com, Accessed: 2018-04-12 (cit. on pp. 6, 8, 54).
- [27] A. De Greef, P. Lambert, and A. Delchambre, “Towards flexible medical instruments: Review of flexible fluidic actuators”, *Precision Engineering*, vol. 33, no. 4, pp. 311–321, 2009 (cit. on p. 6).
- [28] S. D. Prior, P. R. Warner, A. S. White, J. Parsons, and R. Gill, “Actuators for rehabilitation robots”, *Mechatronics*, vol. 3, no. 3, pp. 285–294, 1993 (cit. on p. 6).
- [29] Y. S. K. Takeo Takagi Yokohama, *Pneumatic actuator for manipulator*, US Patent 4,615,260, 1986 (cit. on p. 6).
- [30] A. Moers, M. De Volder, and D. Reynaerts, “Integrated high pressure microhydraulic actuation and control for surgical instruments”, *Biomedical Microdevices*, vol. 14, no. 4, pp. 699–708, 2012 (cit. on p. 6).
- [31] K. Ashwin, D. P. Jose, and A. Ghosal, “Modeling and analysis of a flexible end-effector for actuating endoscopic catheters”, in *Proceedings of the 14th IFToMM World Congress*, IFToMM, 2015, pp. 113–120 (cit. on pp. 6, 7).
- [32] H. M. Le, T. N. Do, and S. J. Phee, “A survey on actuators-driven surgical robots”, *Sensors and Actuators A: Physical*, vol. 247, pp. 323–354, 2016 (cit. on p. 6).
- [33] T. Noritsugu and T. Tanaka, “Application of rubber artificial muscle manipulator as a rehabilitation robot”, *IEEE/ASME Transactions on Mechatronics*, vol. 2, no. 4, pp. 259–267, 1997 (cit. on p. 6).
- [34] P. K. Jamwal, S. Q. Xie, S. Hussain, and J. G. Parsons, “An adaptive wearable parallel robot for the treatment of ankle injuries”, *IEEE/ASME Transactions on Mechatronics*, vol. 19, no. 1, pp. 64–75, 2014 (cit. on p. 6).
- [35] G. Andrikopoulos, G. Nikolakopoulos, and S. Manesis, “A survey on applications of pneumatic artificial muscles”, in *19th Mediterranean Conference on Control & Automation, MED 2011*, IEEE, 2011, pp. 1439–1446 (cit. on p. 7).

- [36] A. P. Tjahyono, K. C. Aw, H. Devaraj, W. Surendra, E. Haemmerle, and J. Travas-Sejdic, “A five-fingered hand exoskeleton driven by pneumatic artificial muscles with novel polypyrrole sensors”, *Industrial Robot: An International Journal*, vol. 40, no. 3, pp. 251–260, 2013 (cit. on p. 7).
- [37] S. C. Obiajulu, E. T. Roche, F. A. Pigula, and C. J. Walsh, “Soft pneumatic artificial muscles with low threshold pressures for a cardiac compression device”, in *International Design Engineering Technical Conferences and Computers and Information in Engineering Conference*, ASME, 2013, V06AT07A009–V06AT07A009 (cit. on p. 7).
- [38] M. De Volder, A. Moers, and D. Reynaerts, “Fabrication and control of miniature McKibben actuators”, *Sensors and Actuators A: Physical*, vol. 166, no. 1, pp. 111–116, 2011 (cit. on pp. 7, 26, 33, 54).
- [39] S. Chakravarthy, K. Aditya, and A. Ghosal, “Experimental characterization and control of miniaturized pneumatic artificial muscle”, *Journal of Medical Devices*, vol. 8, no. 4, p. 041011, 2014 (cit. on p. 7).
- [40] M. Bryant, M. A. Meller, and E. Garcia, “Toward variable recruitment fluidic artificial muscles”, in *ASME 2013 Conference on Smart Materials, Adaptive Structures and Intelligent Systems*, ASME, 2013, V002T06A014–V002T06A014 (cit. on p. 7).
- [41] —, “Variable recruitment fluidic artificial muscles: Modeling and experiments”, *Smart Materials and Structures*, vol. 23, no. 7, p. 074009, 2014 (cit. on pp. 7, 18, 32).
- [42] M. A. Meller, J. B. Chipka, M. J. Bryant, and E. Garcia, “Modeling of the energy savings of variable recruitment McKibben muscle bundles”, in *Bioinspiration, Biomimetics, and Bioreplication 2015*, International Society for Optics and Photonics, vol. 9429, 2015, 94290S (cit. on pp. 7, 18).
- [43] R. M. Robinson, C. S. Kothera, and N. M. Wereley, “Variable recruitment testing of pneumatic artificial muscles for robotic manipulators”, *IEEE/ASME Transactions on Mechatronics*, vol. 20, no. 4, pp. 1642–1652, 2015 (cit. on p. 7).
- [44] M. Meller, J. Chipka, A. Volkov, M. Bryant, and E. Garcia, “Improving actuation efficiency through variable recruitment hydraulic McKibben muscles: Modeling, orderly recruitment control, and experiments”, *Bioinspiration & Biomimetics*, vol. 11, no. 6, p. 065004, 2016 (cit. on pp. 7, 18).
- [45] S. Kurumaya, H. Nabae, G. Endo, and K. Suzumori, “Design of thin McKibben muscle and multifilament structure”, *Sensors and Actuators A: Physical*, vol. 261, pp. 66–74, 2017 (cit. on pp. 7, 27).

- [46] B. Wang, K. C. Aw, M. Biglari-Abhari, and A. McDaid, “Design and fabrication of a fiber-reinforced pneumatic bending actuator”, in *2016 IEEE International Conference on Advanced Intelligent Mechatronics, AIM*, IEEE, 2016, pp. 83–88 (cit. on pp. 7, 25).
- [47] W. McMahan, V Chitrakaran, M Csencsits, D Dawson, I. D. Walker, B. A. Jones, M Pritts, D Dienno, M Grissom, and C. D. Rahn, “Field trials and testing of the octarm continuum manipulator”, in *Proceedings of the 2006 IEEE International Conference on Robotics and Automation (ICRA)*, IEEE, 2006, pp. 2336–2341 (cit. on p. 7).
- [48] J. Bishop-Moser, G. Krishnan, and S. Kota, “Force and moment generation of fiber-reinforced pneumatic soft actuators”, in *Proceedings of 2013 IEEE/RSJ International Conference on Intelligent Robots and Systems (IROS)*, IEEE, 2013, pp. 4460–4465 (cit. on p. 7).
- [49] M. Yip and N. Das, “Robot autonomy for surgery”, *arXiv preprint arXiv:1707.03080*, 2017 (cit. on p. 7).
- [50] E. E. Barakat, M. A. Bedaiwy, S. Zimberg, B. Nutter, M. Nosseir, and T. Falcone, “Robotic-assisted, laparoscopic, and abdominal myomectomy: A comparison of surgical outcomes”, *Obstetrics & Gynecology*, vol. 117, no. 2, pp. 256–266, 2011 (cit. on p. 7).
- [51] A. Wolf, H. B. Brown, R. Casciola, A. Costa, M. Schwerin, E Shamas, and H. Choset, “A mobile hyper redundant mechanism for search and rescue tasks”, in *Proceedings of the 2003 IEEE/RSJ International Conference on Intelligent Robots and Systems (IROS)*, IEEE, vol. 3, 2003, pp. 2889–2895 (cit. on p. 7).
- [52] R. R. Murphy, S. Tadokoro, D. Nardi, A. Jacoff, P. Fiorini, H. Choset, and A. M. Erkmen, “Search and rescue robotics”, in *Springer Handbook of Robotics*, Springer, 2008, pp. 1151–1173 (cit. on p. 7).
- [53] G. S. Chirikjian and J. W. Burdick, “Hyper-redundant robot mechanisms and their applications”, in *Proceedings of the IEEE/RSJ International Workshop on Intelligent Robots and Systems, 'Intelligence for Mechanical Systems', (IROS)*, IEEE, 1991, pp. 185–190 (cit. on pp. 7, 9, 77).
- [54] E. Paljug, T. Ohm, and S. Hayati, “The JPL serpentine robot: A 12-dof system for inspection”, in *Proceedings of the 1995 IEEE International Conference on Robotics and Automation (ICRA)*, IEEE, vol. 3, 1995, pp. 3143–3148 (cit. on p. 7).
- [55] R. L. William II and J. B. Mayhew IV, “Obstacle-free control of the hyper-redundant NASA inspection manipulator”, in *Proceedings of the Fifth National Conference on Applied Mechanics and Robotics*, 1997, pp. 12–15 (cit. on p. 7).

- [56] L. Gargiulo, P. Bayetti, V. Bruno, J.-C. Hatchressian, C. Hernandez, M. Houry, D. Keller, J.-P. Martins, Y. Measson, Y. Perrot, *et al.*, “Operation of an ITER relevant inspection robot on Tore Supra Tokamak”, *Fusion Engineering and Design*, vol. 84, no. 2-6, pp. 220–223, 2009 (cit. on p. 7).
- [57] S. Hirose and M. Mori, “Biologically inspired snake-like robots”, in *IEEE International Conference on Robotics and Biomimetics, (ROBIO)*, IEEE, 2004, pp. 1–7 (cit. on p. 7).
- [58] M. W. Hannan and I. D. Walker, “Analysis and initial experiments for a novel elephant’s trunk robot”, in *Proceedings of the 2000 IEEE/RSJ International Conference on Intelligent Robots and Systems (IROS)*, IEEE, vol. 1, 2000, pp. 330–337 (cit. on p. 7).
- [59] A. A. Transeth, K. Y. Pettersen, and P. Liljebäck, “A survey on snake robot modeling and locomotion”, *Robotica*, vol. 27, no. 7, pp. 999–1015, 2009 (cit. on p. 7).
- [60] I. A. Gravagne and I. D. Walker, “On the kinematics of remotely-actuated continuum robots”, in *Proceedings of the 2000 IEEE International Conference on Robotics and Automation, (ICRA)*, IEEE, vol. 3, 2000, pp. 2544–2550 (cit. on pp. 7, 58, 76, 79, 80, 83).
- [61] Z. Li, P. W. Chiu, and R. Du, “Design and kinematic modeling of a concentric wire-driven mechanism targeted for minimally invasive surgery”, in *2016 IEEE/RSJ International Conference on Intelligent Robots and Systems (IROS)*, IEEE, 2016, pp. 310–316 (cit. on p. 7).
- [62] P. Sears and P. E. Dupont, “Inverse kinematics of concentric tube steerable needles”, in *2007 IEEE International Conference on Robotics and Automation, (ICRA)*, IEEE, 2007, pp. 1887–1892 (cit. on p. 7).
- [63] I. D. Walker, “Continuous backbone “continuum” robot manipulators”, *ISRN robotics*, vol. 2013, 2013 (cit. on p. 8).
- [64] G. Robinson and J. B. C. Davies, “Continuum robots-a state of the art”, in *Proceedings of the 1999 IEEE International Conference on Robotics and Automation (ICRA)*, IEEE, vol. 4, 1999, pp. 2849–2854 (cit. on p. 8).
- [65] I. D. Walker and M. W. Hannan, “A novel ‘elephant’s trunk’ robot”, in *Proceedings of the 1999 IEEE/ASME International Conference on Advanced Intelligent Mechatronics*, IEEE, 1999, pp. 410–415 (cit. on p. 8).
- [66] K. Cao, R. Kang, J. Wang, Z. Song, and J. Dai, “Kinematic model and workspace analysis of tendon-driven continuum robots”, in *Proceedings of the 14th IFToMM World Congress*, 2015, pp. 640–644 (cit. on p. 8).

- [67] D. C. Rucker and R. J. Webster III, “Statics and dynamics of continuum robots with general tendon routing and external loading”, *IEEE Transactions on Robotics*, vol. 27, no. 6, pp. 1033–1044, 2011 (cit. on pp. 8, 76, 83).
- [68] K. Xu and N. Simaan, “An investigation of the intrinsic force sensing capabilities of continuum robots”, *IEEE Transactions on Robotics*, vol. 24, no. 3, pp. 576–587, 2008 (cit. on p. 8).
- [69] R. Behrens, C. Kuchler, T. Förster, and N. Elkmann, “Kinematics analysis of a 3-dof joint for a novel hyper-redundant robot arm”, in *Proceedings of the 2011 IEEE International Conference on Robotics and Automation (ICRA)*, IEEE, 2011, pp. 3224–3229 (cit. on p. 8).
- [70] N. Simaan, R. Taylor, and P. Flint, “A dexterous system for laryngeal surgery”, in *Proceedings of the 2004 IEEE International Conference on Robotics and Automation, (ICRA)*, IEEE, vol. 1, 2004, pp. 351–357 (cit. on pp. 8, 58).
- [71] X. Dong, M. Raffles, S. C. Guzman, D. Axinte, and J. Kell, “Design and analysis of a family of snake arm robots connected by compliant joints”, *Mechanism and Machine Theory*, vol. 77, pp. 73–91, 2014 (cit. on p. 8).
- [72] M. Blessing and I. D. Walker, “Novel continuum robots with variable-length sections”, in *Proceedings of the 3rd IFAC Symposium on Mechatronic Systems*, 2004, pp. 55–60 (cit. on p. 8).
- [73] D. E. Whitney, “Resolved motion rate control of manipulators and human prostheses”, *IEEE Transactions on Man-Machine Systems*, vol. 10, no. 2, pp. 47–53, 1969 (cit. on p. 9).
- [74] A. Liegeois, “Automatic supervisory control of the configuration and behaviour of multi-body mechanisms”, *IEEE Transactions on Systems, Man and Cybernetics*, vol. 7, no. 12, pp. 868–871, 1977 (cit. on p. 9).
- [75] J. Baillieul, J. Hollerbach, and R. Brockett, “Programming and control of kinematically redundant manipulators”, in *The 23rd IEEE Conference on Decision and Control*, IEEE, vol. 23, 1984, pp. 768–774 (cit. on p. 9).
- [76] A. A. Maciejewski and C. A. Klein, “Obstacle avoidance for kinematically redundant manipulators in dynamically varying environments”, *The International Journal of Robotics Research*, vol. 4, no. 3, pp. 109–117, 1985 (cit. on p. 9).
- [77] Y. K. Hwang and N. Ahuja, “Gross motion planning—a survey”, *ACM Computing Surveys (CSUR)*, vol. 24, no. 3, pp. 219–291, 1992 (cit. on p. 9).

- [78] S. Chiaverini, “Singularity-robust task-priority redundancy resolution for real-time kinematic control of robot manipulators”, *IEEE Transactions on Robotics and Automation*, vol. 13, no. 3, pp. 398–410, 1997 (cit. on p. 9).
- [79] L. Sciavicco and B. Siciliano, “A solution algorithm to the inverse kinematic problem for redundant manipulators”, *IEEE Journal on Robotics and Automation*, vol. 4, no. 4, pp. 403–410, 1988 (cit. on p. 9).
- [80] Z. Mao and T. C. Hsia, “Obstacle avoidance inverse kinematics solution of redundant robots by neural networks”, *Robotica*, vol. 15, no. 1, pp. 3–10, 1997 (cit. on p. 9).
- [81] G. Antonelli and S. Chiaverini, “Fuzzy redundancy resolution and motion coordination for underwater vehicle-manipulator systems”, *IEEE Transactions on Fuzzy Systems*, vol. 11, no. 1, pp. 109–120, 2003 (cit. on p. 9).
- [82] B. Dasgupta, A. Gupta, and E. Singla, “A variational approach to path planning for hyper-redundant manipulators”, *Robotics and Autonomous Systems*, vol. 57, no. 2, pp. 194–201, 2009 (cit. on p. 9).
- [83] O. Khatib, “Real-time obstacle avoidance for manipulators and mobile robots”, in *Autonomous Robot Vehicles*, Springer, 1986, pp. 396–404 (cit. on p. 9).
- [84] V. J. Lumelsky and A. A. Stepanov, “Path-planning strategies for a point mobile automaton moving amidst unknown obstacles of arbitrary shape”, *Algorithmica*, vol. 2, no. 1-4, pp. 403–430, 1987 (cit. on p. 9).
- [85] H. Choset, “Coverage for robotics—a survey of recent results”, *Annals of Mathematics and Artificial Intelligence*, vol. 31, no. 1-4, pp. 113–126, 2001 (cit. on p. 9).
- [86] J.-C. Latombe, *Robot motion planning*. Springer Science & Business Media, 2012, vol. 124 (cit. on p. 9).
- [87] S Sreenivasan, P. Goel, and A. Ghosal, “A real-time algorithm for simulation of flexible objects and hyper-redundant manipulators”, *Mechanism and Machine Theory*, vol. 45, no. 3, pp. 454–466, 2010 (cit. on pp. 9, 87).
- [88] M. S. Menon, G. Ananthasuresh, and A. Ghosal, “Natural motion of one-dimensional flexible objects using minimization approaches”, *Mechanism and Machine Theory*, vol. 67, pp. 64–76, 2013 (cit. on pp. 9, 77, 87).
- [89] M. S. Menon, V. Ravi, and A. Ghosal, “Trajectory planning and obstacle avoidance for hyper-redundant serial robots”, *Journal of Mechanisms and Robotics*, vol. 9, no. 4, p. 041 010, 2017 (cit. on pp. 10, 88, 89).

- [90] R. M. Robinson, C. S. Kothera, and N. M. Wereley, “Quasi-static nonlinear response of pneumatic artificial muscles for both agonistic and antagonistic actuation modes”, *Journal of Intelligent Material Systems and Structures*, vol. 26, no. 7, pp. 796–809, 2015 (cit. on pp. 13, 14, 23, 29, 33).
- [91] R. M. Robinson, C. S. Kothera, R. M. Sanner, and N. M. Wereley, “Nonlinear control of robotic manipulators driven by pneumatic artificial muscles”, *IEEE/ASME Transactions on Mechatronics*, vol. 21, no. 1, pp. 55–68, 2016 (cit. on p. 13).
- [92] H. Li, K. Kawashima, K. Tadano, S. Ganguly, and S. Nakano, “Achieving haptic perception in forceps’ manipulator using pneumatic artificial muscle”, *IEEE/ASME Transactions on Mechatronics*, vol. 18, no. 1, pp. 74–85, 2013 (cit. on pp. 13, 28).
- [93] B. Tondu, “Modelling of the McKibben artificial muscle: A review”, *Journal of Intelligent Material Systems and Structures*, vol. 23, no. 3, pp. 225–253, 2012 (cit. on pp. 13, 23, 31, 45).
- [94] H. Schulte, “The application of external power in prosthetics and orthotics”, *The Characteristics of the McKibben Artificial Muscle, National Research Council*, vol. 874, 1961 (cit. on pp. 14, 19, 33).
- [95] G. K.H.S. L. Das, B. Tondu, F. Forget, J. Manhes, O. Stasse, and P. Souères, “Controlling a multi-joint arm actuated by pneumatic muscles with quasi-DDP optimal control”, in *2016 IEEE/RSJ International Conference on Intelligent Robots and Systems (IROS)*, IEEE, 2016, pp. 521–528 (cit. on pp. 14, 17).
- [96] I. Doric, A. Reitberger, S. Wittmann, R. Harrison, and T. Brandmeier, “A novel approach for the test of active pedestrian safety systems”, *IEEE Transactions on Intelligent Transportation Systems*, vol. 18, no. 5, pp. 1299–1312, 2017 (cit. on pp. 14, 28).
- [97] T. E. Pillsbury, N. M. Wereley, and Q. Guan, “Comparison of contractile and extensile pneumatic artificial muscles”, *Smart Materials and Structures*, vol. 26, no. 9, p. 095034, 2017 (cit. on p. 14).
- [98] C.-P. Chou and B. Hannaford, “Measurement and modeling of McKibben pneumatic artificial muscles”, *IEEE Transactions on Robotics and Automation*, vol. 12, no. 1, pp. 90–102, 1996 (cit. on pp. 15, 16, 27, 33, 35, 48).
- [99] B. Tondu and P. Lopez, “Modeling and control of McKibben artificial muscle robot actuators”, *IEEE Control Systems*, vol. 20, no. 2, pp. 15–38, 2000 (cit. on pp. 17, 18, 32, 33).

- [100] T. Itto and K. Kogiso, “Hybrid modeling of McKibben pneumatic artificial muscle systems”, in *2011 IEEE International Conference on Industrial Technology (ICIT)*, IEEE, 2011, pp. 65–70 (cit. on pp. 17, 28).
- [101] S. Davis and D. G. Caldwell, “Braid effects on contractile range and friction modeling in pneumatic muscle actuators”, *The International Journal of Robotics Research*, vol. 25, no. 4, pp. 359–369, 2006 (cit. on pp. 18, 33).
- [102] E. Chapman, M. Macleod, and M. Bryant, “Electrohydraulic modeling of a fluidic artificial muscle actuation system for robot locomotion”, in *ASME 2015 Conference on Smart Materials, Adaptive Structures and Intelligent Systems*, ASME, 2015, V001T03A005–V001T03A005 (cit. on p. 19).
- [103] G. Andrikopoulos, G. Nikolakopoulos, and S. Manesis, “Novel considerations on static force modeling of pneumatic muscle actuators”, *IEEE/ASME Transactions on Mechatronics*, vol. 21, no. 6, pp. 2647–2659, 2016 (cit. on pp. 19, 25, 33, 48).
- [104] W. F. Carlo Ferraresi, W. Walter Franco, and A. Bertetto, “Flexible pneumatic actuators: A comparison between the McKibben and the straight fibres muscles”, *Journal of Robotics and Mechatronics*, vol. 13, pp. 56–63, 2001 (cit. on pp. 20, 26, 33).
- [105] C. S. Kothera, M. Jangid, J. Sirohi, and N. M. Wereley, “Experimental characterization and static modeling of McKibben actuators”, *Journal of Mechanical Design*, vol. 131, no. 9, p. 091 010, 2009 (cit. on pp. 20, 21, 23, 39, 48).
- [106] N. Delson, T. Hanak, K. Loewke, and D. N. Miller, “Modeling and implementation of McKibben actuators for a hopping robot”, in *Proceedings of the 12th International Conference on Advanced Robotics, (ICAR)*, IEEE, 2005, pp. 833–840 (cit. on pp. 20, 33).
- [107] M. Mooney, “A theory of large elastic deformation”, *Journal of Applied Physics*, vol. 11, no. 9, pp. 582–592, 1940 (cit. on p. 20).
- [108] R. Rivlin, “Large elastic deformations of isotropic materials IV. Further developments of the general theory”, *Philosophical Transactions of the Royal Society of London A*, vol. 241, no. 835, pp. 379–397, 1948 (cit. on p. 20).
- [109] G. K. Klute and B. Hannaford, “Accounting for elastic energy storage in McKibben artificial muscle actuators”, *Journal of Dynamic Systems, Measurement, and Control*, vol. 122, no. 2, pp. 386–388, 2000 (cit. on p. 21).
- [110] B. K. Woods, C. S. Kothera, and N. M. Wereley, “Wind tunnel testing of a helicopter rotor trailing edge flap actuated via pneumatic artificial muscles”, *Journal of Intelligent Material Systems and Structures*, vol. 22, no. 13, pp. 1513–1528, 2011 (cit. on p. 21).

- [111] D. Trivedi, A. Lotfi, and C. D. Rahn, “Geometrically exact models for soft robotic manipulators”, *IEEE Transactions on Robotics*, vol. 24, no. 4, pp. 773–780, 2008 (cit. on pp. 22, 33, 48).
- [112] B. Kim, S. B. Lee, J. Lee, S. Cho, H. Park, S. Yeom, and S. H. Park, “A comparison among Neo-Hookean model, Mooney-Rivlin model, and Ogden model for chloroprene rubber”, *International Journal of Precision Engineering and Manufacturing*, vol. 13, no. 5, pp. 759–764, 2012 (cit. on p. 22).
- [113] G. Wang, N. M. Wereley, and T. Pillsbury, “Non-linear quasi-static model of pneumatic artificial muscle actuators”, *Journal of Intelligent Material Systems and Structures*, vol. 26, no. 5, pp. 541–553, 2015 (cit. on pp. 22, 33).
- [114] M. D. Doumit, “Characterization, modeling and design of the braided pneumatic muscle”, PhD thesis, University of Ottawa (Canada), 2009 (cit. on pp. 22, 33).
- [115] E. G. Hocking and N. M. Wereley, “Analysis of nonlinear elastic behavior in miniature pneumatic artificial muscles”, *Smart Materials and Structures*, vol. 22, no. 1, p. 014016, 2012 (cit. on pp. 23, 26, 27, 33, 39, 47, 48).
- [116] W. Liu and C. Rahn, “Fiber-reinforced membrane models of McKibben actuators”, *Transactions of the ASME-E-Journal of Applied Mechanics*, vol. 70, no. 6, pp. 853–859, 2003 (cit. on pp. 23, 24, 33, 48).
- [117] A. Kydonieffs and E. P. Salathe, “Finite cylindrical deformations of a reinforced elastic tube”, *International Journal of Engineering Science*, vol. 12, no. 6, pp. 519–535, 1974 (cit. on p. 23).
- [118] J. E. A. Albert Edward Green, *Large Elastic Deformations*. Clarendon Press, 1970, vol. 1 (cit. on p. 23).
- [119] E. Ball and E. Garcia, “Effects of bladder geometry in pneumatic artificial muscles”, *Journal of Medical Devices*, vol. 10, no. 4, p. 041001, 2016 (cit. on pp. 24, 33, 34).
- [120] N. Goulbourne, “A mathematical model for cylindrical, fiber reinforced electro-pneumatic actuators”, *International Journal of Solids and Structures*, vol. 46, no. 5, pp. 1043–1052, 2009 (cit. on p. 24).
- [121] D. Chen and K. Ushijima, “Prediction of the mechanical performance of McKibben artificial muscle actuator”, *International Journal of Mechanical Sciences*, vol. 78, pp. 183–192, 2014 (cit. on pp. 24, 33).

- [122] W. Zhang, M. L. Accorsi, and J. W. Leonard, “Analysis of geometrically nonlinear anisotropic membranes: Application to pneumatic muscle actuators”, *Finite Elements in Analysis and Design*, vol. 41, no. 9-10, pp. 944–962, 2005 (cit. on p. 25).
- [123] M. G. Antonelli, P. Beomonte Zobel, F. Durante, and T. Raparelli, “Numerical modelling and experimental validation of a McKibben pneumatic muscle actuator”, *Journal of Intelligent Material Systems and Structures*, vol. 28, no. 19, pp. 2737–2748, 2017 (cit. on p. 25).
- [124] D. Sangian, S. Naficy, G. M. Spinks, and B. Tondu, “The effect of geometry and material properties on the performance of a small hydraulic McKibben muscle system”, *Sensors and Actuators A: Physical*, vol. 234, pp. 150–157, 2015 (cit. on pp. 27, 33, 34, 48).
- [125] A. Pujana-Arrese, A. Mendizabal, J. Arenas, R. Prestamero, and J. Landaluze, “Modelling in modelica and position control of a 1-dof set-up powered by pneumatic muscles”, *Mechatronics*, vol. 20, no. 5, pp. 535–552, 2010 (cit. on p. 28).
- [126] S. Ganguly, A. Garg, A. Pasricha, and S. Dwivedy, “Control of pneumatic artificial muscle system through experimental modelling”, *Mechatronics*, vol. 22, no. 8, pp. 1135–1147, 2012 (cit. on p. 28).
- [127] L. Sui and S. Xie, “Modelling of pneumatic muscle actuator and antagonistic joint using linearised parameters”, *International Journal of Biomechatronics and Biomedical Robotics* 19, vol. 2, no. 2-4, pp. 67–74, 2013 (cit. on p. 28).
- [128] B. Tondu, “Closed-loop position control of artificial muscles with a single integral action: Application to robust positioning of McKibben artificial muscle”, in *2013 IEEE International Conference on Mechatronics (ICM)*, IEEE, 2013, pp. 718–723 (cit. on p. 28).
- [129] —, “Single linear integral action control for closed-loop positioning of a biomimetic actuator with artificial muscles”, in *2015 European Control Conference (ECC)*, IEEE, 2015, pp. 3585–3590 (cit. on p. 28).
- [130] M. Van Damme, P. Beyl, B. Vanderborght, R. Van Ham, I. Vanderniepen, R. Versluys, F. Daerden, and D. Lefeber, “Modeling hysteresis in pleated pneumatic artificial muscles”, in *2008 IEEE Conference on Robotics, Automation and Mechatronics*, IEEE, 2008, pp. 471–476 (cit. on p. 29).
- [131] J. A. Stakvik and J. T. G. Michael R.P. Ragazzon Arnfinn A. Eielsen, “On implementation of Preisach model for hysteresis identification and inversion for hysteresis compensation”, *Modeling, Identification and Control*, 2015 (cit. on p. 29).

- [132] W. D. Iwan, “A distributed-element model for hysteresis and its steady-state dynamic response”, *Journal of Applied Mechanics*, vol. 33, no. 4, pp. 893–900, 1966 (cit. on p. 29).
- [133] T. V. Minh, T. Tjahjowidodo, H. Ramon, and H. Van Brussel, “Control of a pneumatic artificial muscle (pam) with model-based hysteresis compensation”, in *IEEE/ASME International Conference on Advanced Intelligent Mechatronics, (AIM)*, IEEE, 2009, pp. 1082–1087 (cit. on p. 29).
- [134] T. Vo Minh, T. Tjahjowidodo, H. Ramon, and H. Van Brussel, “A new approach to modeling hysteresis in a pneumatic artificial muscle using the Maxwell-slip model”, *IEEE/ASME Transactions on Mechatronics*, vol. 16, no. 1, pp. 177–186, 2011 (cit. on p. 29).
- [135] C.-J. Lin, C.-R. Lin, S.-K. Yu, and C.-T. Chen, “Hysteresis modeling and tracking control for a dual pneumatic artificial muscle system using Prandtl–Ishlinskii model”, *Mechatronics*, vol. 28, pp. 35–45, 2015 (cit. on pp. 30, 31).
- [136] M. Ismail, F. Ikhoulane, and J. Rodellar, “The hysteresis Bouc-Wen model, a survey”, *Archives of Computational Methods in Engineering*, vol. 16, no. 2, pp. 161–188, 2009 (cit. on p. 30).
- [137] A. Visintin, *Differential Models of Hysteresis*. Springer Science & Business Media, 2013, vol. 111 (cit. on p. 30).
- [138] S. Xie, J. Mei, H. Liu, and Y. Wang, “Hysteresis modeling and trajectory tracking control of the pneumatic muscle actuator using modified Prandtl–Ishlinskii model”, *Mechanism and Machine Theory*, vol. 120, pp. 213–224, 2018 (cit. on p. 31).
- [139] H. Aschemann and D. Schindele, “Comparison of model-based approaches to the compensation of hysteresis in the force characteristic of pneumatic muscles”, *IEEE Transactions on Industrial Electronics*, vol. 61, no. 7, pp. 3620–3629, 2014 (cit. on p. 31).
- [140] Y. Liu, X. Zang, Z. Lin, X. Liu, and J. Zhao, “Modelling length/pressure hysteresis of a pneumatic artificial muscle using a modified Prandtl–Ishlinskii model”, *Strojniški vestnik-Journal of Mechanical Engineering*, vol. 63, no. 1, pp. 56–64, 2017 (cit. on p. 31).
- [141] L. Hao, H. Yang, Z. Sun, C. Xiang, and B. Xue, “Modeling and compensation control of asymmetric hysteresis in a pneumatic artificial muscle”, *Journal of Intelligent Material Systems and Structures*, vol. 28, no. 19, pp. 2769–2780, 2017 (cit. on p. 31).

- [142] E. Chapman, T. Jenkins, and M. Bryant, “Parametric study of a fluidic artificial muscle actuated electrohydraulic system”, in *ASME 2016 Conference on Smart Materials, Adaptive Structures and Intelligent Systems*, ASME, 2016, V002T06A003–V002T06A003 (cit. on p. 32).
- [143] MATLAB, *version 9.1 (R2016b)*. Natick, Massachusetts: The MathWorks Inc., 2016 (cit. on p. 36).
- [144] J. Diani, B. Fayolle, and P. Gilormini, “A review on the Mullins effect”, *European Polymer Journal*, vol. 45, no. 3, pp. 601–612, 2009 (cit. on p. 39).
- [145] C. S. Jog, *Continuum Mechanics*. Cambridge University Press, 2015, vol. 1 (cit. on p. 39).
- [146] S. Neppalli, B Jones, W. McMahan, V Chitrakaran, I Walker, M Pritts, M Csencsits, C Rahn, and M Grissom, “Octarm-a soft robotic manipulator”, in *2007 IEEE/RSJ International Conference on Intelligent Robots and Systems (IROS)*, IEEE, 2007, pp. 2569–2569 (cit. on p. 54).
- [147] M. B. Pritts and C. D. Rahn, “Design of an artificial muscle continuum robot”, in *2004 IEEE International Conference on Robotics and Automation (ICRA)*, IEEE, vol. 5, 2004, pp. 4742–4746 (cit. on p. 54).
- [148] R. Hartley and A. Zisserman, *Multiple View Geometry in Computer Vision*. Cambridge University Press, 2003 (cit. on p. 62).
- [149] R. J. Roesthuis, M. Kemp, J. J. van den Dobbelsteen, and S. Misra, “Three-dimensional needle shape reconstruction using an array of fiber bragg grating sensors”, *IEEE/ASME Transactions on Mechatronics*, vol. 19, no. 4, pp. 1115–1126, 2014 (cit. on p. 62).
- [150] A. Ghosal, *Robotics: Fundamental Concepts and Analysis*. Oxford University Press, 2006 (cit. on p. 67).
- [151] J. Starke, E. Amanov, M. T. Chikhaoui, and J. Burgner-Kahrs, “On the merits of helical tendon routing in continuum robots”, in *2017 IEEE/RSJ International Conference on Intelligent Robots and Systems (IROS)*, IEEE, 2017, pp. 6470–6476 (cit. on p. 76).
- [152] H. M. Choset and J. Burdick, “Sensor based motion planning: The hierarchical generalized voronoi graph”, PhD thesis, California Institute of Technology (USA), 1996 (cit. on p. 77).
- [153] C. J. Taylor and D. J. Kriegman, “Vision-based motion planning and exploration algorithms for mobile robots”, *IEEE Transactions on Robotics and Automation*, vol. 14, no. 3, pp. 417–426, 1998 (cit. on p. 77).

- [154] M. Li, D. Mazilu, and K. A. Horvath, “Robotic system for transapical aortic valve replacement with MRI guidance”, in *International Conference on Medical Image Computing and Computer-Assisted Intervention*, Springer, 2008, pp. 476–484 (cit. on p. 77).
- [155] S.-E. Song, N. B. Cho, G. Fischer, N. Hata, C. Tempany, G. Fichtinger, and I. Iordachita, “Development of a pneumatic robot for MRI-guided transperineal prostate biopsy and brachytherapy: New approaches”, in *2010 IEEE International Conference on Robotics and Automation (ICRA)*, IEEE, 2010, pp. 2580–2585 (cit. on p. 77).
- [156] S. Neppalli, M. A. Csencsits, B. A. Jones, and I. D. Walker, “Closed-form inverse kinematics for continuum manipulators”, *Advanced Robotics*, vol. 23, no. 15, pp. 2077–2091, 2009 (cit. on p. 86).
- [157] H. Edelsbrunner and E. P. Mücke, “Three-dimensional alpha shapes”, *ACM Transactions on Graphics (TOG)*, vol. 13, no. 1, pp. 43–72, 1994 (cit. on p. 97).
- [158] D.-T. Lee and B. J. Schachter, “Two algorithms for constructing a delaunay triangulation”, *International Journal of Computer & Information Sciences*, vol. 9, no. 3, pp. 219–242, 1980 (cit. on p. 97).
- [159] V. M. Spitzer and D. G. Whitlock, “The visible human dataset: The anatomical platform for human simulation”, *The Anatomical Record: An Official Publication of the American Association of Anatomists*, vol. 253, no. 2, pp. 49–57, 1998 (cit. on p. 98).
- [160] J. Cao, A. Tagliasacchi, M. Olson, H. Zhang, and Z. Su, “Point cloud skeletons via Laplacian based contraction”, in *Shape Modeling International (SMI 2010)*, IEEE, 2010, pp. 187–197 (cit. on p. 99).
- [161] Blender Online Community, *Blender—A 3D modelling and rendering package*, Blender Foundation, Blender Institute, Amsterdam, 2018. [Online]. Available: <http://www.blender.org> (cit. on p. 99).
- [162] C. N, “Modeling of wheeled mobile robots on uneven terrain”, Master’s thesis, Indian Institute of Science, Bangalore (India), 2003 (cit. on p. 100).